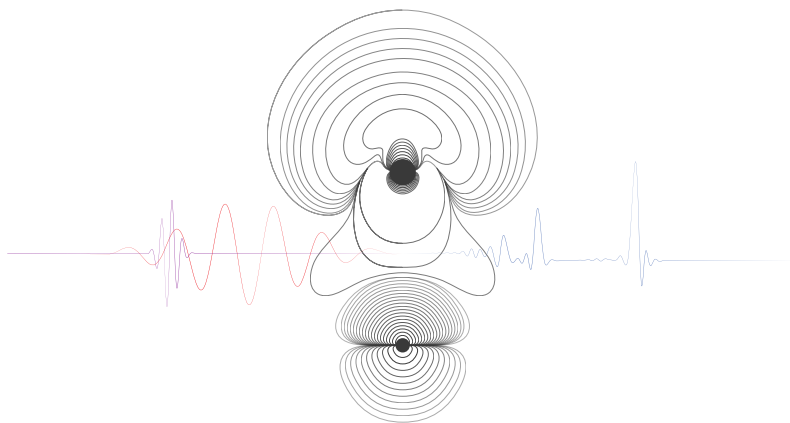


ATTOSECOND TRANSIENT ABSORPTION
SPECTROSCOPY
IN DIATOMIC MOLECULES



NIKOLAJ SCHRØDER WITTIG RAVN

PHD THESIS
JULY 2020

SUPERVISOR: LARS BOJER MADSEN
CO-SUPERVISOR: FRANK JENSEN

DEPARTMENT OF PHYSICS AND ASTRONOMY
AARHUS UNIVERSITY

English summary

The ultrafast dynamics of electrons inside atoms, molecules, and solids demand extraordinarily fast measurement methods to keep up with the electrons and achieve a sufficient temporal resolution. This is due to the fact that the natural timescale of the electron dynamics is measured in attoseconds, a timescale so unfathomably short compared to the timescale of seconds that humans inhabit. A second is to electrons and their attosecond existence what the age of the universe is to us.

Methods to probing electron dynamics have had to match these timescales, and the only currently known way to achieve the temporal resolution is to use extremely short pulses of laser light. The invention of such pulses has opened the field of attosecond science, dedicated to the advancement of the understanding and control of ultrafast phenomena.

In this thesis we apply the method of attosecond transient absorption spectroscopy (ATAS) in the study of the dynamics of diatomic molecules. ATAS is a pump-probe scheme, where the system dynamics are first instigated and later recorded by very accurately timed pairs of light pulses. The precise control of the delay between the two pulses enables the creation of detailed spectrograms, with features containing information about the underlying processes. The main focus of this thesis is the description and implementation of numerical simulations of molecular systems, with subsequent theoretical analysis of the appearing features. In particular, the analysis of the spectrum of the molecule Lithium Fluoride, and the analysis of a propose model exhibiting non-adiabatic effects due to the presence of an avoided crossing.

Dansk resumé

I atomer, molekyler, og faststoffer farer elektronerne ultrahurtigt rundt, og for at kunne følge med elektronerne påkræves exceptionelt hurtige målemetoder, som kan opnå en tilstrækkelig tidslig opløsning af elektrondynamikken. Dette skyldes, at et attosekund – den naturlige tidsskala for elektrondynamik – er så ubegribeligt kort sammenlignet med den sekundbaserede tidsskala, som mennesker lever på. For elektronerne er et sekund hvad universets alder er for os.

Metoder, der kan undersøge elektrondynamikken, er nødt til at kunne matche disse tidsskalaer. På nuværende tidspunkt er den eneste metode, som kan opløse dynamik på attosekundskala, brugen af ekstremt korte pulser af laserlys. Opfindelsen af disse pulser har lagt grundstenen for attosekundsvideenskaben, et forskningsfelt dedikeret til at fremme vores forståelse og kontrol af ultrahurtige fænomener.

I denne afhandling anvender vi den såkaldte “attosecond transient absorption spectroscopy” (ATAS) metode til at studere diatomare molekylers dynamik. ATAS er en pumpe-probe-protokol, hvor systemets dynamik først igangsættes og derefter måles af parvise laserpulser. Tidsforskydningen af disse pulser, som kan kontrolleres med høj præcision, gør det muligt at måle højt detaljerede spektrogrammer, som indeholder tegn fra de bagvedliggende processer.

Denne afhandlings hovedfokus har været numeriske simulering og teoretisk analyse af molekylære systemer. Specielt har vi analyseret spektret af molekylært Lithiumfluorid, og undersøgt effekterne af ikke-adiabatiske kobling i et modelsystem.

Preface

This dissertation presents the main work I have done during my PhD studies at the Department of Physics and Astronomy at Aarhus University, Denmark. The research was carried out in the period from August 2017 to July 2020 under the supervision of Professor Lars Bojer Madsen, with co-supervision of Associate Professor Frank Jensen. In addition, I was at a research stay in the spring of 2019 at the Arctic University of Norway (UiT) in Tromsø, Norway, under the supervision of Professor Kenneth Ruud and Researcher Bin Gao.

Notation

Hartree atomic units ($m_e = e = \hbar = a_0 = 1$) are used through the thesis, unless explicitly stated otherwise.

In accordance with GSNS rules, part of this thesis contain material that was also used in the progress report for the qualifying examination.

Acknowledgments

First I would like to thank my main supervisor Lars Bojer Madsen, who has guide me the last three years through countless hours of discussions. His door was always open, ready to talk and offer advice in both work and life. I would also like to thank my co-supervisor Frank Jensen, for his patience in teaching quantum chemistry to a physicist.

A great thanks is extended to all my colleagues and friends from the department, including Philip Daniel Blocher, Alexander Holm Kiilerich, Jinglei Zhang, Felix Motzoi, Kenneth Klochmann Hansen, Kamanasish Debnath, Izhak Cohen, Simon Vendelbo Bylling Jensen, Ben Lemberger, Albert Benseny Cases, Jørgen Johansen Rørstad and the rest of the Bojer

group. In addition I thank Grete Flarup and Ann-Berit Porse Stærkær for their immense help and good spirit when bureaucracy caused troubles.

I thank Professor Kenneth Ruud and his whole group for hosting me at the Arctic University in Tromsø, and Bin Gao for his work as my daily supervisor during my stay.

Outside of the departments wall I thank my friends and family for their invaluable company and support. In particular my thanks go out to Simon Skjødt for our countless runs and discussions, Julie Astono for the many adventures we went on together, my loving mother and father who brought me up with kindness and my two younger sisters who are still among my closest friends. A special thanks is also given to Kevin Kuriakose for the creation of a wonderful cover image.

Nikolaj Schrøder Wittig Ravn
Aarhus, July 2020

List of Publications

- [1] J. J. Rørstad, N. S. W. Ravn, L. Yue, and L. B. Madsen, Attosecond transient-absorption spectroscopy of polar molecules, *Phys. Rev. A* **98**, 053401 (2018).

Contents

Preface	iii
1 Introduction and outline	1
2 Main Theory	5
2.1 Attosecond Transient Absorption Spectroscopy and the Response function	5
2.2 The Molecular System	7
2.2.1 Field interaction	9
2.2.2 The Molecular Dipole Operator	9
2.2.3 Nuclear wave functions and the Born-Oppenheimer expansion	10
2.2.4 Use of Symmetry and Selection Rules	13
2.3 Obtaining Molecular Properties - Electronic Structure Theory	15
2.3.1 Calculating the Ground State	15
2.3.2 Response Theory	18
2.3.3 Stitching Curves Together and the Problem of Sign .	19
2.4 The Adiabatic and Diabatic Representations	21
2.4.1 Avoided crossings and the noncrossing rule	22
2.4.2 Transforming to the diabatic representation	24
2.4.3 An illustrative example of two adiabatic and diabatic curves	26
2.5 Fundamental Features of the ATA spectra	30
2.5.1 Adiabatic Three-level Model	31
2.5.2 Expanding the Three-level Model to multiple levels .	42
2.6 Two-level Model for a system with a permanent dipole . . .	45
2.6.1 Light-induced structures	49
2.6.2 Ladder structures	50
3 Numerical Methods	55

3.1	Grid Representation	55
3.1.1	Grid Hamiltonian for vibrational levels and eigenstates	56
3.2	Time Evolution	57
3.2.1	Split Operator Method	58
3.2.2	The Fast-Fourier Transform	59
3.2.3	Imaginary Time Propagation	61
3.3	Complex Absorbing Potential	62
3.4	The Window Function	63
4	The LiF molecule, a polar diatomic molecule	65
4.1	The LiF system and field parameters	65
4.2	Full numerical simulation	68
4.3	Light-induced structures	70
4.4	Ladder feature	73
4.5	Polar versus nonpolar molecules	76
4.6	Orientation and alignment	76
5	Model System	79
5.1	Parameters of the system and the fields	79
5.2	XUV-only spectroscopy	83
5.2.1	Dynamics of the nuclear wave-packets	86
5.3	ATA spectra of the Model System	89
5.3.1	Using the Multi-level model	92
6	Summary and Outlook	99
A	Fourier Transforms of the fields	101
B	Adiabatic Multi-Level model	107
	Bibliography	112

Introduction and outline

Since the invention of the laser in the 1960's, the strive to study increasingly fast processes has been pushing the duration of the pulses to ever shorter timescales. With the use of high harmonic generation (HHG), a non-linear effect where a target sample is made to emit high harmonics of the generation beam, production of sub-femtosecond pulses have been achieved. With the advent of these attosecond pulses, it has become possible to study the dynamics of electrons in atoms, molecules and solids on their natural time scale. This is of interest both on a fundamental level, since it broadens our knowledge to new phenomena, but also of practical use. A better understanding and possible control of electronic dynamics could help us in: understanding and possibly steering of biochemical processes, understanding the size and speed limits of electronic information processing and magnetic information storage, raising the efficiency of solar cells, and more [2].

Observation of the motion of the electrons requires first the ability to trigger and subsequently to probe the process as well as controlling the timing of these two pump and probe steps accurately. The dynamics are mapped out by variation of the time delay between the trigger and probe in a pump-probe setup, such that repeated experiments at different delays give rise to a time-resolved spectrogram. The usual setup consists of an initial femtosecond laser pulse, either infrared (IR) or near infrared (NIR), which is split in two. One part is used to generate the attosecond pump field, which is usually in the ultraviolet (UV) to extreme ultraviolet (XUV) domain, through HHG, while the other can be used as the probe. An important property of HHG, is that the generated attosecond pulse is coherent with itself as well as coherent with the original generating pulse.

Because the generated field in HHG is synchronized with the original generating field, it is possible to control the delay between the pump and probe with high sub-femtosecond precision [3]. The observables of such an experiment can be either outgoing electrons and other charged particles or outgoing light. The charged particles provide a more direct measurement since they carry directly the information from the system, while the photon detection is a more indirect measurement. The latter can be an advantage since it is less invasive and can be done using lower intensities. The lower intensities mean that optical detection methods are closer to the perturbative regime, meaning that the extracted dynamics more closely resembles the field-free dynamics of interest. The lower intensities also mean that the computationally demanding continuum states of the electrons are not needed in the description. Detection of photons can also be done more efficiently than that of outgoing electrons from strong-field photoionization, making the optical methods more experimentally favorable.

Attosecond transient absorption spectroscopy (ATAS) is a pump-probe type experiment as described above, where one measures the frequency-resolved, time-integrated absorption of the system. For dilute gases macroscopic effects can be neglected and the absorption spectrum can be described accurately under a single-system-response approximation [3, 4], though experiments have been carried out outside of this regime [5, 6]. When the system interacts with the external femtosecond and attosecond pulses a time-dependent dipole moment is induced, and the interference between the generated field from the oscillating dipole and the original attosecond field is recorded. It is therefore the calculation of the time-dependent dipole moment that is of interest in theoretical modeling of ATAS.

ATAS has been used to study atomic systems since 2010, and experiments [7–9] as well as theory [10, 11] have led to the discovery and analysis of new phenomena. Work has also been extended to solid state systems [12–14], and, of more interest to this project, experiments have been carried out on diatomic molecules [15–18].

For dynamics of molecules the theory used is that of electronic structure and nuclear wave packets. By expanding the total wave function in the adiabatic electronic basis one arrives at the picture of the nuclear wave packets moving on electronic potential energy surfaces. This introduces a new level of complexity compared with the atoms, since nuclear motion and the shape of the energy surfaces must now be taken into account [19, 20]. Typically one ignores the effect of rotation, simplifying the nuclear motion by freezing the molecule at a fixed angle with respect to the linear

polarized fields. Usually the axis of the molecule is chosen to coincide with the polarization of the linearly polarized incoming fields, but studies have also been done on alignment effects [21]. To model ATAS in molecules, one therefore needs to calculate the electronic adiabatic energies over a range of molecular geometries, as well as calculating their geometry dependent dipole moment functions and the non-adiabatic coupling elements which allow for the interaction between different surfaces and nuclear wave packets.

Calculation of the potential energy as a function of the nuclear geometry can be obtained using electronic structure theory methods, such as the wave functions based Multi-configuration Self-Consistent Field (MCSCF) method. Excited state energies can be found using linear-response and state averaging [22]. Dipole moments between the ground and excited states can also be obtained through linear response, while the elements between excited states requires quadratic response [23]. The non-adiabatic couplings elements between the ground and excited states have been derived and can be calculated for MCSCF method by linear response [24], but calculations of elements between excited states are not yet available.

The effect of non-adiabatic couplings in ATAS for diatomic molecules have not been considered yet, though a look into the effect of a two-dimensional conical intersection have been published [25]. The aim of this project is therefore the implementation of the non-adiabatic couplings into the established theory. This requires the implementation of the physical model used to simulate the experiment. The method consists of propagating the nuclear wave functions described by their time-dependent Schrödinger equation (TDSE), using the split-operator Fourier method [26]. This method has been used in prior studies [19] and has already been implemented and used [21]. To include the effect of the non-adiabatic couplings, which both depend on the nuclear coordinate and momentum, we will use the adiabatic to diabatic transformation [27] to remove the kinetic part at the prices of acquiring a non-diagonal potential energy. In this form, the non-adiabatic couplings are of a more suitable form for the propagation method.

Main Theory

2.1 Attosecond Transient Absorption Spectroscopy and the Response function

In the introduction we described the setup for ATAS, where a femtosecond and an attosecond pulse separated by a time delay τ are sent into a target, and how the signal recorded by the detector is the interference between the generated field from the target and the incoming attosecond field. In this chapter we introduce the response function, which is the time integrated signal that the detector captures. We will not give a derivation of this expression, and restrict ourselves to a short introduction. More comprehensive treatments can be found in ref. [10] and ref. [19].

Under the assumption of the fields propagating as plane waves linearly polarized in the z-direction, the spectral distribution function is given as [28]

$$\begin{aligned} S(\omega, \tau) &= |\tilde{\mathbf{F}}_{\text{in}}(\omega, \tau) + \tilde{\mathbf{F}}_{\text{gen}}(\omega, \tau)|^2 \\ &= |\tilde{\mathbf{F}}_{\text{in}}(\omega, \tau)|^2 + 2\text{Re}[\tilde{\mathbf{F}}_{\text{in}}^*(\omega, \tau) \cdot \tilde{\mathbf{F}}_{\text{gen}}(\omega, \tau)] + |\tilde{\mathbf{F}}_{\text{gen}}(\omega, \tau)|^2, \end{aligned} \quad (2.1)$$

where $\tilde{\mathbf{F}}_{\text{in}}(\omega, \tau)$ and $\tilde{\mathbf{F}}_{\text{gen}}(\omega, \tau)$ are the Fourier transformed incoming and generated fields respectively. The variable τ denotes the time delay between the incoming attosecond and femtosecond fields. We will use the following convention for the Fourier transform (indicated by a tilde)

$$\tilde{f}(\omega) = \frac{1}{\sqrt{2\pi}} \int_{\mathbb{R}} dt f(t) e^{-i\omega t}. \quad (2.2)$$

We simplify the expression by noting that the term $|\tilde{\mathbf{F}}_{\text{in}}(\omega, \tau)|^2$ contains no information of the system and the term $|\tilde{\mathbf{F}}_{\text{gen}}(\omega, \tau)|^2$ is weak compared to the interference term. Neglecting these two terms leave us with the expression

$$S(\omega, \tau) = 2\text{Re}[\tilde{\mathbf{F}}_{\text{in}}^*(\omega, \tau) \cdot \tilde{\mathbf{F}}_{\text{gen}}(\omega, \tau)], \quad (2.3)$$

which is what we will refer to as the response function. Since the incoming field is assumed to be linearly polarized along the z-direction, only the z-component of the generated field will contribute and we will therefore drop the boldface and will only keep the z-component.

The attosecond pulse will usually be in the XUV or the UV range and the femtosecond pulse in the IR or NIR range. In the rest of this chapter we will refer to the attosecond pulse as F_{XUV} and the femtosecond pulse as F_{IR} .

The incoming field is known and its Fourier transform can be readily calculated, and we are therefore left with calculating the generated field. Under the assumption of the target being a dilute gas [4], we can neglect the complicated and computationally demanding effects that entail the field propagating through a medium, and adopt a single-system approximation wherein the field is generated by the interaction with a single molecule. The generated field will then be entirely due to the radiation from the induced dipole of the molecule, where it can be shown that the generated field is proportional to the z-component of the dipole moment in the frequency domain [19]

$$\tilde{F}_{\text{gen}}(\omega, \tau) = -i \frac{2\pi\omega\rho}{c} \tilde{D}(\omega, \tau). \quad (2.4)$$

For the incoming field $\tilde{F}_{\text{in}}^*(\omega, \tau)$ it is sufficient to use the XUV $\tilde{F}_{\text{XUV}}^*(\omega, \tau)$, as the XUV and IR are usually well separate in frequency and the energies of interest are in the range of the XUV.

Putting all this together we arrive at the final expression

$$S(\omega, \tau) = \frac{4\pi\rho\omega}{c} \text{Im}[\tilde{F}_{\text{XUV}}^*(\omega, \tau) \tilde{D}(\omega, \tau)], \quad (2.5)$$

where the only unknown is the induced dipole moment $\tilde{D}(\omega, \tau)$. The constant ρ denotes the density of the gas, which will arbitrarily be set to one since it is just a global constant. We note that a negative value of the response function corresponds to absorption, while a positive value corresponds to emission.

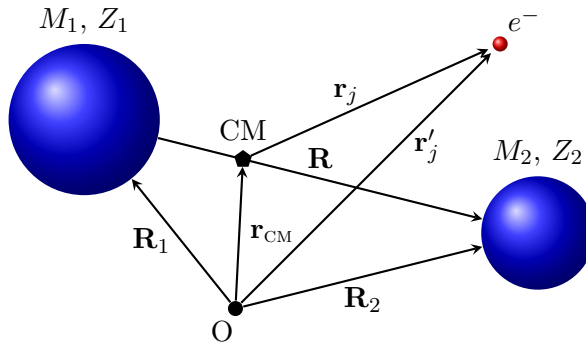


Figure 2.1: Sketch of coordinates used to describe the diatomic molecule. For simplicity only one electron is shown. Due to the very large difference in mass between the nuclei and the electrons, the center of mass of the whole system is approximately given by the center of mass of the two nuclei. See Eq. (2.9), Eq. (2.10), and Eq. (2.11).

2.2 The Molecular System

The systems under consideration in this thesis are diatomic molecules. In non-relativistic quantum mechanics the physical state of a system is described by its wave function Ψ , which is governed by the time-dependent Schrödinger equation

$$i\partial_t\Psi(\mathbf{x}, t) = \hat{H}\Psi(\mathbf{x}, t). \quad (2.6)$$

Here the operator \hat{H} is the Hamiltonian of the system, usually given by the energy

$$\hat{H} = \hat{T} + \hat{V}, \quad (2.7)$$

where \hat{T} is the kinetic energy and \hat{V} is the potential. The full Hamiltonian of a diatomic molecule, without the presence of an external field, will contain; the kinetic energy of the two nuclei, the kinetic energy of the N_e electrons, and the potential energy coming from the Coulomb interaction between the electrons, between the two nuclei, and between the electrons and the nuclei

$$\hat{H}_0 = \hat{T}_n + \hat{T}_e + \hat{V}_{ee} + \hat{V}_{nn} + \hat{V}_{ne} = \hat{T}_n + \hat{T}_e + \hat{V}. \quad (2.8)$$

To describe the position of the two nuclei together with the N_e electrons, naively one would need the $3 \times 2 + 3 \times N_e$ laboratory fixed coordinates $\mathbf{R}_1, \mathbf{R}_2, \mathbf{r}'_1, \mathbf{r}'_2, \dots, \mathbf{r}'_{N_e}$. However, by changing to the center of mass frame

and the relative coordinates

$$\mathbf{R} = \mathbf{R}_2 - \mathbf{R}_1 \quad (2.9)$$

$$\mathbf{r}_{\text{CM}} = \frac{M_1 \mathbf{R}_1 + M_2 \mathbf{R}_2 + \sum_{j=1}^{N_e} \mathbf{r}'_j}{M_{\text{tot}}} \approx \frac{M_1 \mathbf{R}_1 + M_2 \mathbf{R}_2}{M_1 + M_2} \quad (2.10)$$

$$\mathbf{r}_j = \mathbf{r}'_j - \frac{M_1 \mathbf{R}_1 + M_2 \mathbf{R}_2}{M_1 + M_2} \quad (2.11)$$

the center of mass motion can be separated out, and the number of coordinates needed is reduced by 3. In the above transformation, which can be seen illustrated in figure 2.1, we will later use the very good approximation that the center of mass of the full system is very close to the center of mass between the two nuclei since the nuclear masses are much larger than the electron mass. In the new coordinates the kinetic energy of the nuclei is given by the derivative with respect to the internuclear distance

$$\hat{T}_n = -\frac{1}{2\mu} \frac{\partial^2}{\partial \mathbf{R}^2}, \quad (2.12)$$

with the reduced mass of the two nuclei $\mu = M_1 M_2 / (M_1 + M_2)$.

In our description we will freeze out the much slower rotational motion and only include the vibrational dynamics of the nuclei. In this case the nuclear kinetic energy is simply

$$\hat{T}_n = -\frac{1}{2\mu} \frac{\partial^2}{\partial R^2}. \quad (2.13)$$

The separation of the kinetic energy for the electrons in the center of mass will not be exact in general, but by neglecting the small coupling, known as the mass polarization term $\hat{T}_{\text{mp}} = 1/(2(M_1 + M_2)) \sum_{i,j=1}^{N_e} \partial^2 / (\partial \mathbf{r}_i \partial \mathbf{r}_j)$, we can write the kinetic energy of the electrons as

$$\hat{T}_e = -\sum_{j=1}^{N_e} \frac{1}{2} \frac{\partial^2}{\partial \mathbf{r}_j^2}. \quad (2.14)$$

It is customary to group the electronic kinetic energy together with the potential energy and write the Hamiltonian as

$$\hat{H}_0 = \hat{T}_n + (\hat{T}_e + \hat{V}) = \hat{T}_n + \hat{H}_e, \quad (2.15)$$

where \hat{H}_e is denoted as the electronic Hamiltonian.

Factoring out the center of mass motion and freezing out the rotational motion, the system now only depends on the internuclear distance R and the relative electronic coordinates $\mathbf{r} = \{\mathbf{r}_1, \mathbf{r}_2, \dots, \mathbf{r}_{N_e}\}$. We will position the molecule such that the internuclear axis is along the z-axis i.e. parallel to the polarization of the two incoming fields. We will use this orientation throughout the thesis

2.2.1 Field interaction

As was discussed when we introduced the single-system response function 2.1, we will treat the fields classically and then include them in the quantum description of the molecule by the usual minimal substitution in the Hamiltonian. As is customary we will further assume the dipole approximation, where the spatial variation of the field over the molecule is neglected, to be valid.

In our work we use fields define through

$$F(t) = -\partial_t A(t), \quad (2.16)$$

with a vector potential with central frequency ω and a Gaussian envelope

$$A(t) = A_0 e^{-\frac{(t-t_c)^2}{T^2/4}} \cos[\omega(t-t_c) + \phi]. \quad (2.17)$$

For the parameters of the fields we have $A_0 = F_0/\omega$, with F_0 being the field amplitude, related to the intensity of the field by $I = |F_0|^2$; t_c is the center of the pulse; ϕ is the carrier-envelope phase (CEP); and $T = N_c T_c = N_c \frac{2\pi}{\omega}$ is the duration of the pulse, with T_c the period of a single cycle and N_c the number of cycles. As discussed earlier we consider only linearly polarized fields, with the polarization axis parallel to the internuclear separation.

Working in the length gauge the interaction of the molecule with the field is given by

$$\hat{V}_L(t) = -\mathbf{F}(t) \cdot \hat{\mathbf{D}} = -F(t)\hat{D}, \quad (2.18)$$

where, since the field is polarized along the z-direction, only the z-component \hat{D} of the dipole operator is used.

2.2.2 The Molecular Dipole Operator

For a diatomic molecule the total dipole operator of the system is given by [29]

$$\hat{\mathbf{D}} = Z_1 \mathbf{R}_1 + Z_2 \mathbf{R}_2 - \sum_{j=1}^{N_e} \mathbf{r}'_j, \quad (2.19)$$

in the laboratory fixed coordinates. Using instead the center of mass coordinates defined by Eq. (2.9), Eq. (2.10) and Eq. (2.11), we find

$$\hat{\mathbf{D}} = (Z_1 + Z_2 - N_e)\mathbf{r}_{\text{CM}} + \alpha\mathbf{R} - \beta \sum_{j=1}^{N_e} \mathbf{r}_j, \quad (2.20)$$

with the constants

$$\alpha = \frac{M_1 Z_2 - M_2 Z_1}{M_1 + M_2}, \quad \beta = 1 + \frac{Z_1 + Z_2 - N_e}{M_1 + M_2}. \quad (2.21)$$

In the case of a neutral molecule, which is the only systems we will consider, the total charge $Z_1 + Z_2 - N_e$ is zero, and the dipole operator reduces to

$$\hat{\mathbf{D}} = \alpha\mathbf{R} - \sum_{j=1}^{N_e} \mathbf{r}_j. \quad (2.22)$$

For homonuclear molecules, such as H_2 , O_2 or N_2 , where $M_1 = M_2$ and $Z_1 = Z_2$ the constant α reduces to zero, and the only contribution to the dipole is from the electrons.

2.2.3 Nuclear wave functions and the Born-Oppenheimer expansion

The time-dependent Schrödinger equation for the molecular system in the presence of an external field is

$$i\partial_t\Psi(\mathbf{r}, R, t) = \hat{H}(t)\Psi(\mathbf{r}, R, t) \quad (2.23)$$

with the total time-dependent Hamiltonian

$$\hat{H}(t) = \hat{H}_0 + \hat{V}_L(t), \quad (2.24)$$

where \hat{H}_0 is the field-free Hamiltonian Eq. (2.8) and $\hat{V}_L(t)$ is the interaction with the field Eq. (2.18).

The Schrödinger equation contains both the fast moving lightweight electrons and the slow moving heavy nuclei, and performing the time evolution numerically of the total system would be extremely demanding due to the very different time scales of their respective motion. The usual approach to this problem is to write the full wave function as an expansion

$$\Psi(\mathbf{r}, R, t) = \sum_{k=1}^N \chi_k^{(a)}(t, R)\Phi_k^{(a)}(\mathbf{r}; R) \quad (2.25)$$

in the basis of the time-independent electronic states defined by the electronic Hamiltonian

$$\hat{H}_e(R)\Phi_k^{(a)}(\mathbf{r}; R) = E_k^{(a)}(R)\Phi_k^{(a)}(\mathbf{r}; R). \quad (2.26)$$

This is known as the Born-Oppenheimer expansion [30], and the expansion coefficients $\chi_n(t, R)$ as the nuclear wave functions. The electronic Hamiltonian depends only on the nuclear coordinate and not its momentum. We can therefore consider the electronic eigenvalue equation above as being parametrically dependent on R , and consider it as an equation for each fixed geometry. This is similar to the viewpoint in adiabatic theory, where one considers a Hamiltonian that depends “slowly” on an external parameter [31]. In the case of the molecule, it is the nuclear coordinate R that varies slowly compared to the electronic coordinates \mathbf{r} , and one often adopts the picture that the fast electrons follows adiabatically the slower dynamics of the nuclei. The electronic Hamiltonian and states are therefore often referred to as the adiabatic electronic Hamiltonian and adiabatic electronic states and the electronic energies $E_k(R)$ as the adiabatic potential energy curves.

For the expansion in Eq. (2.25) to be exact, the electronic states must be a complete set at each fixed geometry, and the sum must be over all bound and continuum states. In practice this is not necessary, since the fields we are using are in the range where excitation to higher lying bound states and continuum states are very unlikely and can be neglected. We will therefore truncate the sum to only include the N most important states.

Inserting the expansion Eq. (2.25) into the Schrödinger equation Eq. (2.23), and using that the electronic state are eigenstates of the electronic Hamiltonian and are orthonormal, one finds after projecting onto the n^{th} electronic state Φ_n the following coupled equations for the nuclear wave functions

$$i\dot{\chi}_n^{(a)}(t, R) = \left(-\frac{1}{2\mu} \frac{\partial^2}{\partial R^2} + E_n^{(a)}(R) \right) \chi_n^{(a)}(t, R) - F(t) \sum_{k=1}^N D_{nk}^{(a)}(R) \chi_k^{(a)}(t, R) - \frac{1}{2\mu} \sum_{k=1}^N \left(2 \left\langle \Phi_n^{(a)} \left| \frac{\partial}{\partial R} \Phi_k^{(a)} \right\rangle_{\mathbf{r}} \frac{\partial}{\partial R} + \left\langle \Phi_n^{(a)} \left| \frac{\partial^2}{\partial R^2} \Phi_k^{(a)} \right\rangle_{\mathbf{r}} \right) \chi_k^{(a)}(t, R). \quad (2.27)$$

The first two terms on the right hand side are the usual kinetic energy operator working on the nuclear wave function χ_n and a potential energy curve $E_n^{(a)}(R)$ on which it can move. The third term is the interaction

with the field, where we have defined the dipole coupling element between two electronic states

$$D_{nk}^{(a)}(R) = \langle \Phi_n^{(a)} | \hat{D} | \Phi_k^{(a)} \rangle_{\mathbf{r}} \quad (2.28)$$

$$= \int d\mathbf{r}_1 d\mathbf{r}_2 \dots d\mathbf{r}_{N_e} [\Phi_n^{(a)}(\mathbf{r}; R)]^* \hat{D} \Phi_k^{(a)}(\mathbf{r}; R). \quad (2.29)$$

We use the subscript \mathbf{r} to indicate integration over all the electronic coordinates, but not the nuclear coordinate R . The dipole coupling elements are functions of the nuclear separation R , because the electronic wave functions are and will in general vary as the internuclear distance is changed. The fourth and fifth term arise because the electronic states depend on the nuclear coordinate R , and are therefore non-adiabatic in nature. The two coupling terms are in general referred to as the first- and second-order non-adiabatic coupling elements respectively as they appear in all cases where the Hamiltonian depends on a parameter which is treated adiabatically. In the specific case of molecules where the terms represent the couplings between vibrational motion of the nuclei and the electronic dynamics they are referred to as the vibronic coupling, a combination of “vibrational” and “electronic”. The vibronic coupling makes transitions between the adiabatic energy curves possible without the presence of an external field, a process known as a radiationless transition, which can be important in e.g. photochemical reactions.

Using the coupled nuclear equations that arise from the expansion of the full wave function in a sum over electronic states are often referred to as the N -surface model, as it describes the motion of the nuclear wave-packets moving on the N electronic surfaces. Fig. 2.2 shows a sketch of two examples of nuclear dynamics on the electronic potential curves. In both cases a part of the ground state wave function is excited by an XUV pulse onto an excited state. In (a) the excited state curve is dissociative leading to the excited wave packet moving away from the region overlapping with the ground state. In (b) the excited curve is binding the excited wave packet leading to an oscillation in and out of the region overlapping with the ground state.

An accurate description of the dynamics of the nuclear wave functions will in general need both the adiabatic energy curves $E_n^{(a)}$, the dipole matrix elements $D_{nk}^{(a)}$ as well as the two vibronic coupling elements. Obtaining these are no trivial matter and will be discussed later in sec. 2.3.

In the Born-Oppenheimer adiabatic approximation the two vibronic couplings are neglected, and without the presence of the field the nuclear

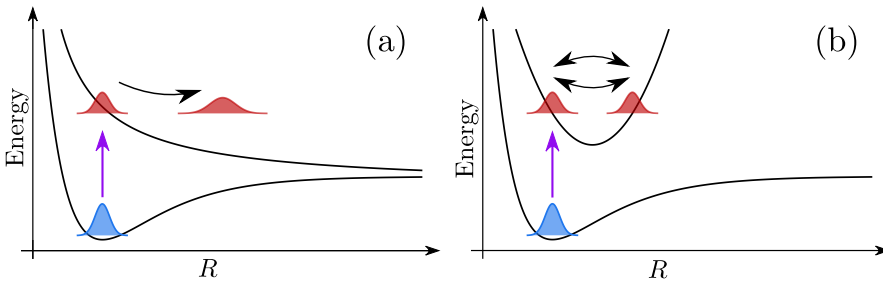


Figure 2.2: Sketch of dynamics of the nuclear wave packet excited by an UV/XUV pulse and subsequently propagating on an excited curve. Panel (a) shows the dynamics when the excited curve is dissociative, and the wave packet escapes. Panel (b) shows the dynamics when the excited curve is bounded, and the wave packet will return.

wave packets on different adiabatic curves are uncoupled. Calculating the non-adiabatic couplings are in general not a trivial matter, and the Born-Oppenheimer approximation is therefore often employed. The approximation works well as long as the vibronic couplings are small, which is generally the case when the different adiabatic curves considered are well separated, but breaks down when they approach each other. This can most clearly be seen through the relation

$$\left\langle \Phi_n^{(a)} \left| \frac{\partial}{\partial R} \Phi_k^{(a)} \right. \right\rangle_{\mathbf{r}} = \frac{\left\langle \Phi_n^{(a)} \left| \frac{\partial \hat{H}_e}{\partial R} \right| \Phi_k^{(a)} \right\rangle_{\mathbf{r}}}{E_n^{(a)}(R) - E_k^{(a)}(R)}, \quad \text{for } n \neq k, \quad (2.30)$$

which shows that the first-order coupling element between two curves can be very large if the two are close together. The sharp peak of the coupling strength arise because the behaviour of the adiabatic electronic states will dependent strongly on the internuclear distance R when the energy curves approach each other, an effect we will consider in more detail later .

In our work we are interested in the effect of the vibronic couplings on the ATA spectra, and we will therefore consider them in more detail, and describe how they can be handled.

2.2.4 Use of Symmetry and Selection Rules

In atomic systems selection rules for the dipole allowed transitions can be found by considering the symmetries of the Hamiltonian. For atoms the system is spherical symmetric and invariant under reflection, which

leads to selection rules based on the l and m quantum numbers, since these labels the irreducible representations of the group of all rotations in 3 dimensional space. The atomic systems are further symmetric under the reflection of all electronic coordinates $\mathbf{r} \rightarrow -\mathbf{r}$, leading to all states being of definite parity. For linearly polarized light along the z-direction, the dipole operator transform in a specific way under the symmetry operations giving the familiar rules $\Delta M_L = 0$ and $\Delta L = 0, \pm 1$. Noteworthy the dipole operator have negative parity, leading to all dipole moments between states belonging to the same irreducible representation being zero and especially all diagonal dipole moments vanishing. One usually adopt the notion of states being either bright or dark with respect to another given state depending on whether a dipole transition is allowed or not, a convention we will use in later description of systems and spectra.

For molecules the analysis is more involved, since different molecules posses different symmetries, but the approach is the same. One considers the symmetry operations which leaves the electronic Hamiltonian Eq. (2.8) invariant and classify the resulting electronic eigenstates by which irreducible representation of the group of symmetries they belong to. The dipole operator will also belong to one of the irreducible representations, and the selections rules can be determined by the condition that the matrix element $\langle \Phi_n | \hat{D} | \Phi_k \rangle$ vanish unless it transforms as the fully symmetric representation. Usually one refers to two states belonging to the same irreducible representation as belonging to the same symmetry, as similar two state of different representations being of different or opposite symmetry

An important point is that homonuclear diatomic molecules are symmetric under parity, and the irreducible representation therefore still being of definite parity. For heteronuclear systems this symmetry is broken, and transitions between states belonging to the same symmetry are therefore no longer forbidden, and the system can have non-negative diagonal dipole moments.

The method of determining selection rules by use of symmetry can also be used on other operators, as long as they belong to a specific symmetry. Use of symmetry can therefore vastly reduce the number of computations needed in calculations of the electronic structure, since one can ignore all matrix elements that vanish due to symmetry. In practice most electronic structure programs (see sec. 2.3) will not consider the full non-abelian symmetry group of the diatomic molecules, which is $C_{\infty v}$ for heteronuclear systems and $D_{\infty h}$ for homonuclear, but restrict the treatment to the largest abelian subgroups C_{2h} and D_{2h} respectively.

2.3 Obtaining Molecular Properties - Electronic Structure Theory

The physical model for the nuclear wave functions is now established, but for it to be useful for real systems, we need to be able to solve the adiabatic electronic equation Eq. (2.26) to obtain the potential energy curves as well as the dipole moments, and if significant, the vibronic couplings. The equation depends parametrically on the nuclear coordinate. The approach is therefore to fix the nuclei, solve the equation for several geometries and then stitch together the properties.

An important part of theoretical quantum chemistry is to obtain these properties using ab initio methods known collectively as electronic structure theory. In this theory there are roughly two main approaches; methods based on wave functions and methods based on density functional theory (DFT). We will only give a short introduction to the former, but the latter is also widely used. We will further give a short description of response theory, which is a method used to obtain the molecular properties from the ground state without the need of explicitly constructing the excited states.

For a textbook introduction to electronic structure theory we refer to ref. [32] and for a more advance treatment ref. [22]. For an introduction to response theory used in electronic structure we refer to the textbook of ref. [33] or the chapter in ref. [34].

2.3.1 Calculating the Ground State

The electronic equation Eq. (2.26) can only be solved exactly for the H_2^+ molecule and similar one-electron systems, so approximate methods must be applied. We consider here a series of ab initio wave function models based on the variational principle.

In variational methods, one seeks wave functions that minimizes the energy

$$E_e = \frac{\langle \Phi | \hat{H}_e | \Phi \rangle}{\langle \Phi | \Phi \rangle}, \quad (2.31)$$

as this condition determine the systems ground state. The electronic wave function must obey the Pauli principle, and one can therefore use Slater determinants of single-electron functions $\Phi_{\text{SD}} = |\phi_{p_1} \phi_{p_2} \dots \phi_{p_{N_e}}|$ to build trial wave functions. The one-electron functions $\{\phi_i\}$ are called molecular orbitals (MOs), and are usually expressed as a linear combination of a set of

basis functions $\phi_i = \sum_{j=1}^M c_{ji} f_j$. The basis functions $\{f_j\}$ are referred to as atomic orbitals (AOs), and their form are chosen based on computational efficiency and how well they suit the problem. Gaussian functions are often used, since the required integrals for the variational methods are easily calculated, but numerous different sets are in use with their application depending on the problem at hand. The number of AOs are typically much larger than the number of electrons, and the solution will consequently produce a number of unoccupied or virtual orbitals in addition to the occupied MOs. These virtual orbitals have no direct physical meaning, but can be used to generate excited configurations.

The simplest method is the Hartree-Fock (HF) method, where a single Slater determinant is used. Variation of the energy Eq. (2.31) with respect to the MOs yields a set of pseudo-eigenvalue equations. An iterative method must therefore be used, and a set of solutions is called self-consistent field (SCF) orbitals. The electron-electron repulsion is only accounted for in an average fashion in the HF method, and the method is therefore only a mean-field approximation.

The HF method is usually good enough to give $\sim 99\%$ of the total energy, but the remaining $\sim 1\%$ is often very important for the description of chemical and physical phenomena. The difference between the HF energy and the lowest energy of the given basis set is therefore called the correlation energy. The difference is due to the fact that the electron motion is correlated and that the electrons on average are further apart than the mean-field theory predicts. The correlation energy is usually divided into two contributions; dynamic correlation and static correlation. Dynamic correlation is associated with the instantaneous Coulomb repulsion between pairs of electrons. It is short-ranged and will in general require a very large orbital set for an accurate description. The static correlation is due to near-degeneracies of configurations. It can be substantial at stretched geometries, where the dissociative wave functions are described by different configurations with similar energies. The distinction is; however, not clear-cut and is more meant as a conceptual tool.

The HF method gives the optimal one-determinant energy in a given basis set, and improvements must therefore come from the use of a multi-determinant wave function. In the configuration interaction method (CI), one uses the converged HF orbitals to generate new excited configurations by replacing one or more of the occupied MOs by the unoccupied orbitals. The determinants are usually referred to as singly, doubly, triply, etc. excited determinants relative to the HF. The new trial wave function is then a linear combination of such determinants. The orbitals are already

optimized by the HF method, so the variation is done with respect to the coefficients and the method is thus linear. Building the CI wave function is a combinatorial problem and scales as a factorial. Full CI is therefore unfeasible even for small systems, and one must truncate the expansion. Including only the singly excited determinants yields no improvement to the energy, since Brillouin's theorem gives that the matrix elements between the HF reference and singly excited states are zero. The lowest expansion that gives an improvement is therefore the inclusion of the doubly excited determinants, which are the only states that have a non-zero matrix element with the HF.

The CI method is based on the improvement of the HF wave function, and thus fails when the HF function is inadequate at describing the system. This will occur when multiple configurations are important, since the HF by its very nature is a single configuration. The multiconfigurational self-consistent field (MCSCF) method varies the configurational coefficients and the orbitals simultaneously, and do not introduce a bias towards a single configuration. The downside is that the optimization is highly nonlinear and must be solved iteratively like the HF, making it much more complicated. Convergence is usually harder to obtain and second order methods, such as Newton-Raphson, are often needed. The MCSCF method describes static correlation by being a multiconfigurational method, but does not describe the dynamic correlation very well. Because optimization is done with respect to both the configuration coefficients and the orbitals, the number of configurations that can be included in the MCSCF method is much less than for CI.

To simplify the problem, one therefore introduces a smaller number of active orbitals and uses these to build the configurations, while keeping the other orbitals inactive. For smaller active spaces, it is then possible to do full CI in the restricted space. This method is known as the complete active space self-consistent field (CASSCF) method. In contrast to the HF and CI methods, where the procedure was clearly laid out, the MCSCF methods relies on some physical and chemical insight when choosing the active space. The active space should include all orbitals where the occupation number changes significantly as we scan over the different geometries, or where the occupation number differs noticeably from two or zero.

The MCSCF method includes static correlation, but not the short-range dynamical correlation. We are however only interested in the relative energies, and therefore only need to consider the part of the correlation that changes. Core electrons for example have high dynamic correlation. This means that even though we cannot recover the dynamic correlation

we can get lucky since typically a large contribution comes from the core electrons which are unchanged under variations of the geometry.

MCSCF is one of the few methods that allows direct calculation of excited states, but calculations are often problematic and convergence can be difficult to achieve. In the simplest approach optimization is done on the individual states, and orthogonality can therefore not be guaranteed. Instead one can do a state average by considering an ensemble energy consisting of a weighted average of energies

$$E_{\text{avg}} = \sum_I \omega_I E_I. \quad (2.32)$$

Optimization of this energy will result in identical orbitals but different configuration coefficients for the different states and orthogonality between states is retained.

2.3.2 Response Theory

By using the variational methods of one of the methods above it is possible for a given nuclear geometry to obtain the electronic ground state. Some method, such as the MCSCF, also allows the construction of excited state. There exists another approach to obtain excited properties such as energies and dipoles, which can be done without explicitly computing the excited state wave functions. In response theory one considers how the ground state is perturbed by the presence of an external field, and uses the way the ground state responds to calculate properties not only of the ground state but also of the excited states.

By using an electric field as the external perturbation, it is possible to obtain both the electric dipole moments between the ground and the excited states using linear response and the dipole moments between excited state by going to quadratic order. Response theory also gives a method to get the excited state energies. For MCSCF this is readily implemented in the Dalton program [35, 36].

Obtaining the vibronic couplings through response methods was part of the aim of a research stay at the Arctic University of Norway in Tromsø at the Theoretical Quantum Chemistry group of Professor Kenneth Ruud during the spring of 2019. The group is involved in the development of a library for calculation of molecular properties using response theory with DFT [37]. Calculation of the vibronic couplings is however not as straight forward as e.g. the dipole moment. Calculations of vibronic couplings between the ground state and an excited state are available, but further research is needed for the implementation couplings between excited states.

2.3.3 Stitching Curves Together and the Problem of Sign

The electronic structure methods used to calculate the ground state and the subsequent response theory to obtain the additional molecular properties are all done for a fixed molecular geometry, but for the description of the nuclear dynamics the properties are needed for a wide range of internuclear distances. At first glance this may seem as a simple task, one just repeats the calculation at several different geometries, however certain important aspects should be noted. Calculations of the electronic energies and properties for a wide range of different geometries is however not a trivial task. Different methods and basis sets are usually optimized to describe different regimes to save on computation time, and the need of an accurate results over the full range of internuclear distances will lead to both more expensive and more involved calculations.

Calculations of the properties at different geometries are independent in nature, and, even if one uses preceding converged wave functions as initial inputs, the wave function at neighbouring points does not in general share a common phase. Since the Hamiltonian for the molecular system is real, the corresponding wave functions can be assumed real as well and the phase difference reduces to a difference of sign between the functions.

For the ground and excited state energies this is not a problem, since energies are invariant under a change of sign of the wave functions $|\Phi_k\rangle \rightarrow -|\Phi_k\rangle$

$$E_k = \langle \Phi_k | \hat{H}_e | \Phi_k \rangle \rightarrow (-1)^2 \langle \Phi_k | \hat{H}_e | \Phi_k \rangle = E_k, \quad (2.33)$$

as they arise as diagonal matrix elements. For converged results the potential energy curves will therefore be continuous functions as the internuclear distance is varied.

For the dipole moments, and the vibronic couplings, we are also interested in off-diagonal elements, where a change of sign of one state $|\Phi_k\rangle \rightarrow -|\Phi_k\rangle$ will give a change of sign of the property

$$D_{nk} = \langle \Phi_n | \hat{D} | \Phi_k \rangle \rightarrow -\langle \Phi_n | \hat{D} | \Phi_k \rangle = -D_{nk}. \quad (2.34)$$

Plotting the resulting dipole moments, or vibronic couplings, will therefore in general lead to highly discontinuous curves that jump between positive and negative values.

If the properties could be assumed not to cross the horizontal line, one could just use the absolute value. For the dipoles, however, the behaviour can be quite complex and taking the absolute value will not be sufficient. The presence of avoided crossings (see sec. 2.4.1) will further complicate

the behaviour, since the rapid change of the electronic wave functions at the crossings will lead to a large change in the dipole elements.

One also have to be careful when correcting the sign between different geometries to make sure this is done in a consistent matter. Since the change of sign of the dipole, and other properties, in the end comes from the sign of the electronic states, there is a mutual shared sign one has to consider. As mentioned above, the change in sign of a single electronic state will change the signs of all properties coming from an off-diagonal matrix element involving the given state. Correcting the sign of a single dipole curve will therefore introduce a discrepancy unless all other curves coming from the state are changed as well.

In the adiabatic two- and three-level models, which we will describe in sec. 2.5, where the two incoming fields are treated to second order the dipole moments only enters as squares and the problem of mutual sign is therefore not important. However, a small numerical test on He has shown a visible effect if one assigns random signs, whether this comes from higher order effects or the interplay of multiple levels was not investigated. The effect of the latter can be seen from the semi-analytical results of the multi-level model, where the sign of the dipole moments does matter when working to second order, see Eq. (2.105) and Eq. (2.106).

One way to approach the problem of mutual sign, is to initial disregard the problem and focus on making the dipole moments continuous. Afterwards one can then choose a single geometry and use the mutual signs obtained at that point. The problem remaining is thus to construct continuous curves from the discontinuous data from the electronic structure calculations. For well behaved curves this is quite unproblematic and one can use linear extrapolation. However, as mentioned above, the presence of the avoided crossings can complicated the process. Automation is therefore difficult, and in practice some work must be done by hand.

The simplest solution to the problem of sign and calculation of the dipole moments, is to circumvent the problem by considering transitions to occur mainly through the Franck-Condon window and therefore use a constant value, e.g. the one found at the ground state minima, for the dipoles. This approximations is a good description for all the coupling to the ground state, both the initial excitation by the XUV as well as the main contribution to the signal which comes from the dipole moment of the ground state with the excited wave packets. It does not necessary capture the interaction between the excited states at the same precision, but due to the fact that most of the population being in the ground state this is could still constitute a good approximation.

2.4 The Adiabatic and Diabatic Representations

In the description of the molecular system above in sec. 2.2.3 we considered the adiabatic representation, where the full wave function of the system was expanded in the adiabatic electronic states obtained from the electronic Hamiltonian Eq. (2.26), and subsequently could describe the nuclear motion by wave packets moving on the adiabatic potential energy surfaces. For ease of reading we repeat here the resulting Schrödinger equation for the nuclear wave functions Eq. (2.27)

$$i\dot{\chi}_n^{(a)}(t, R) = \left(-\frac{1}{2\mu} \frac{\partial^2}{\partial R^2} + E_n^{(a)}(R) \right) \chi_n^{(a)}(t, R) - F(t) \sum_{k=1}^N D_{nk}^{(a)}(R) \chi_k^{(a)}(t, R) - \frac{1}{2\mu} \sum_{k=1}^N \left(2 \left\langle \Phi_n^{(a)} \left| \frac{\partial}{\partial R} \Phi_k^{(a)} \right\rangle_{\mathbf{r}} \frac{\partial}{\partial R} + \left\langle \Phi_n^{(a)} \left| \frac{\partial^2}{\partial R^2} \Phi_k^{(a)} \right\rangle_{\mathbf{r}} \right) \chi_k^{(a)}(t, R). \quad (2.35)$$

As discussed earlier the electronic Hamiltonian, and therefore the adiabatic states and potential energy curves, depends parametrically on the nuclear geometry through the internuclear distance R , and this leads to the two vibronic coupling terms involving the two matrix elements

$$P_{nk}(R) = \left\langle \Phi_n^{(a)} \left| \frac{\partial}{\partial R} \Phi_k^{(a)} \right\rangle_{\mathbf{r}}, \quad Q_{nk}(R) = \left\langle \Phi_n^{(a)} \left| \frac{\partial^2}{\partial R^2} \Phi_k^{(a)} \right\rangle_{\mathbf{r}}. \quad (2.36)$$

The couplings arise as the adiabatic electronic states change due to the geometry, coupling the electronic and nuclear degrees of freedom, and they therefore measure the non-adiabatic interaction.

The electronic Hamiltonian in Eq. (2.8) is real, and the corresponding adiabatic electronic states can therefore be chosen to be real valued, which further means that the first- and second-order matrix elements P_{nk} and Q_{nk} are real as well. In this case P_{nk} can further be shown to be skew-symmetric $P_{nk} = -P_{kn}$, and therefore especially zero along the diagonal $P_{nn} = 0$. There is then no diagonal vibrational coupling coming from the first-order element, and the diagonal contribution from the second-order term Q_{nn} can in principle be included as a change to the adiabatic potential energy, since it only depends on the nuclear coordinate and not the nuclear momentum. Usually the effect on the shape of the potential energy is so small that it can be neglected [38].

The terms of interest are therefore the off-diagonal couplings which can transfer population of the nuclear wave packets between different

potential energy curves without the presence of an external field. The first-order coupling contains the matrix element $P_{nk}(R)$, which depends on the nuclear coordinate and the nuclear momentum. This clearly shows the non-adiabatic nature of the coupling, as a slow moving wave packet with low momentum could pass through an area of significant coupling without much effect. As was shown in Eq. (2.30) the matrix element P_{nk} between different electronic states is inversely proportional to the distance in energy between the two adiabatic potential energy curves

$$P_{nk}(R) = \frac{\left\langle \Phi_n^{(a)} \left| \frac{\partial \hat{H}_e}{\partial R} \right| \Phi_k^{(a)} \right\rangle_{\mathbf{r}}}{E_n^{(a)}(R) - E_k^{(a)}(R)}. \quad (2.37)$$

Due to the dependence on the difference between the energy curves the matrix elements grows rapidly for curves close together and approaches an infinite coupling in the limit where they touch. Fortunately the latter will not happen for diatomic molecules due to the noncrossing rule which we will discuss in more detail in the next section.

The second-order coupling $Q_{nk}(R)$ is only dependent on the nuclear coordinate R and not the momentum, and is therefore independent on how quickly the wave packets move. We will not give more attention to the second-order term, as we later consider another representation where the couplings are transformed away and were only information of the first-order matrix element is needed, see sec. 2.4.2.

2.4.1 Avoided crossings and the noncrossing rule

As we saw earlier in Eq. (2.37) the first-order vibronic coupling grows as the inverse of the energy distance between the two adiabatic curves. This could in principle lead to an infinite coupling for intersecting curves, but due to the noncrossing rule this can in general not happen for diatomic molecules.

The noncrossing rule was originally described by von Neumann and Wigner [39] and it gives a condition for when two adiabatic curves can intersect and when this will not be possible. For a textbook description we refer to ref. [29] and ref. [40], both on which the argument below is based.

Let us consider here for simplicity two potential energy curves $E_1(R)$ and $E_2(R)$ that are very close, but not equal, at the internuclear distance R_0 . At R_0 the energies $E_1^0 = E_1(R_0)$ and $E_2^0 = E_2(R_0)$ are eigenvalues of the electronic Hamiltonian $\hat{H}_{e,0} = \hat{H}_e(R_0)$ with corresponding eigenstates

Φ_1^0 and Φ_2^0 , which can be assumed real again because the electronic Hamiltonian is real valued. At a neighbouring geometry $R_0 + \Delta R$ the electronic Hamiltonian is

$$\hat{H}_e(R_0 + \Delta R) \approx \hat{H}_e(R_0) + \Delta R \frac{\partial \hat{H}_e}{\partial R} = \hat{H}_{e,0} + \hat{H}'. \quad (2.38)$$

The change in the internuclear distance introduces a perturbation \hat{H}' , which alters the energy levels such the the difference in energy is now

$$E_2(R_0 + \Delta R) - E_1(R_0 + \Delta R) = \sqrt{(E_2^0 + H'_{22} - E_1^0 - H'_{11})^2 + 4H'_{12}{}^2}. \quad (2.39)$$

The conclusion is then, that the two adiabatic curves can only intersect if $E_2^0 + H'_{22} - E_1^0 - H'_{11} = 0$ and $H'_{12} = 0$. As the electronic Hamiltonian and electronic states are all real, the matrix elements of the perturbation $H'_{nk} = \langle \Phi_n^0 | \hat{H}' | \Phi_k^0 \rangle_{\mathbf{r}}$ are real as well, and we are left with two independent conditions.

For diatomic molecules there is only one parameter, i.e. the internuclear distance R , and it will in general not be possible to satisfy both conditions simultaneously and the curves will therefore never intersect. For systems with two parameters the conditions can in general be met at a single point, leading to conical intersections of the adiabatic surfaces. In polyatomic molecules, where there are many more parameters, the conditions are easily satisfied and there can therefore be intersections not only at points but also as curves or of higher dimensional surfaces.

Intersections in diatomic molecules can however happen if the off-diagonal matrix element H'_{12} vanishes identically. This will happen when the two adiabatic states considered belong to different symmetries of the symmetry group of the system. The non-crossing rule therefore states that the avoided crossings only occur between states belonging to the same symmetry, but that curves stemming from different symmetry can cross. Similarly the same matrix element appears in the expression for the vibronic coupling Eq. (2.37), and the coupling is therefore only present between states of the same symmetry.

The argument given above considers only the interaction of two states. A more rigorous proof is given in ref. [41] where the rule is proven in general. An important detail is however that the result is not a strict rule, it is possible by chance that the two conditions are satisfied at the same distance without the help of symmetry, but this is highly unlikely and for all intents and purposes it is impossible. In the language of probability theory, one would say that the rule holds almost surely.

For the diatomic molecules the noncrossing rule removes the divergence of the vibronic couplings since the term is only present between states of the same symmetry where crossings are avoided. However the vibronic coupling still contain both the nuclear coordinate and the nuclear momentum, and we will in the next section consider an alternative representation.

2.4.2 Transforming to the diabatic representation

When we expanded the full wave function of the molecule in Eq. (2.25) we chose to do this in the adiabatic electronic states defined by the electronic Hamiltonian Eq. (2.26), but we could just as well have used any other basis to represent the state

$$\Psi(\mathbf{r}, R, t) = \sum_{k=1}^N \chi_k^{(a)}(t, R) \Phi_k^{(a)}(\mathbf{r}; R) \quad (2.40)$$

$$= \sum_{k=1}^N \chi_k^{(d)}(t, R) \Phi_k^{(d)}(\mathbf{r}; R). \quad (2.41)$$

The set of nuclear wave functions in the new representation are related to the ones in the adiabatic representation through a unitary transformation

$$\chi_k^{(a)}(\mathbf{r}; R) = \sum_{j=1}^N U_{kj}(R) \chi_j^{(d)}(\mathbf{r}; R) \quad (2.42)$$

with $U_{kj} = \langle \Phi_k^{(a)} | \Phi_j^{(d)} \rangle_{\mathbf{r}}$. In the adiabatic transformation the electronic states are chosen to satisfy the electronic Hamiltonian, which makes the potential energy curves diagonal, but introduces off-diagonal terms in the kinetic energy due to the non-adiabaticity of the electronic states.

Since we are working with finite sums, it can be advantageous to write the nuclear equations Eq. (2.35) in matrix form

$$i\dot{\boldsymbol{\chi}}^{(a)} = \left[-\frac{1}{2\mu} \left(\mathbf{I} \frac{\partial^2}{\partial R^2} + 2\mathbf{P}(R) \frac{\partial}{\partial R} + \mathbf{Q}(R) \right) + \mathbf{V}^{(a)}(R) - F(t)\mathbf{D}^{(a)}(R) \right] \boldsymbol{\chi}^{(a)}, \quad (2.43)$$

where we introduce the diagonal adiabatic potential matrix $V_{nk}^{(a)}(R) = E_k(R)\delta_{nk}$, the nuclear wave function vector $\boldsymbol{\chi}^{(a)} = (\chi_1^{(a)}, \chi_2^{(a)}, \dots, \chi_N^{(a)})^T$ and use P_{nk} and Q_{nk} as defined in Eq. (2.36). The unitary transform between the nuclear function Eq. (2.42) similarly becomes

$$\boldsymbol{\chi}^{(a)} = \mathbf{U}\boldsymbol{\chi}^{(d)}. \quad (2.44)$$

The nature of the vibronic couplings make them ill suited for numerical integration of the equations around the avoided crossings. They grow rapidly around the crossings and they mix the nuclear coordinate and momentum, where the later cannot be treated by our propagation scheme (see sec. 3.2.1).

Using the transformation of Eq. (2.44) the coupled equations for the nuclear wave functions in the new representation becomes

$$\begin{aligned}
 i\dot{\chi}^{(d)} = & \left(-\frac{1}{2\mu} \mathbf{I} \frac{\partial^2}{\partial R^2} + \mathbf{U}^\dagger \mathbf{V}^{(a)} \mathbf{U} \right) \chi^{(d)} - F(t) \mathbf{U}^\dagger \mathbf{D}^{(a)} \mathbf{U} \chi^{(d)} \\
 & - 2\frac{1}{2\mu} \mathbf{U}^\dagger \left(\frac{\partial}{\partial R} \mathbf{U} + \mathbf{P} \mathbf{U} \right) \frac{\partial}{\partial R} \chi^{(d)} \\
 & - \frac{1}{2\mu} \mathbf{U}^\dagger \left(\frac{\partial^2}{\partial R^2} \mathbf{U} + 2\mathbf{P} \frac{\partial}{\partial R} \mathbf{U} + \mathbf{Q} \mathbf{U} \right) \chi^{(d)}. \tag{2.45}
 \end{aligned}$$

The first three terms describe a simpler Schrödinger equation with diagonal kinetic energy, a transformed potential energy and a transformed coupling to the field, while the two other terms are the transformed first- and second order vibronic couplings respectively.

Up until now the new basis set, and therefore the unitary transform, has been arbitrary, but we will now use a particular choice to transform away the vibronic couplings. If we choose the transform to satisfy the equation [27]

$$\frac{\partial}{\partial R} \mathbf{U} + \mathbf{P} \mathbf{U} = 0, \tag{2.46}$$

we can remove the first-order coupling, and if the basis is complete one can further show that

$$\frac{\partial^2}{\partial R^2} \mathbf{U} + 2\mathbf{P} \frac{\partial}{\partial R} \mathbf{U} + \mathbf{Q} \mathbf{U} = 0, \tag{2.47}$$

which removes the second-order term as well. Due to this last relation, we only need to know the first-order coupling in order to calculate the transformation matrix. In our case however we use a truncated basis, and the second equation is then only approximately true, but valid as long as the first-order couplings to the neglected levels are small.

Using the basis defined by Eq. (2.46) we obtain the so-called diabatic representation, where the Schrödinger equation reads

$$i\dot{\chi}^{(d)} = \left(-\frac{1}{2\mu} \mathbf{I} \frac{\partial^2}{\partial R^2} + \mathbf{V}^{(d)} - F(t) \mathbf{D}^{(d)} \right) \chi^{(d)}, \tag{2.48}$$

with the transformed diabatic potential

$$\mathbf{V}^{(d)} = \mathbf{U}^\dagger \mathbf{V}^{(a)} \mathbf{U} \quad (2.49)$$

and diabatic dipole moments

$$\mathbf{D}^{(d)} = \mathbf{U}^\dagger \mathbf{D}^{(a)} \mathbf{U}. \quad (2.50)$$

Or in non-matrix form

$$\begin{aligned} i\dot{\chi}_n^{(d)}(t, R) = & \sum_{k=1}^N \left(-\frac{1}{2\mu} \delta_{nk} \frac{\partial^2}{\partial R^2} + V_{nk}^{(d)}(R) \right) \chi_k^{(d)}(t, R) \\ & - F(t) \sum_{k=1}^N D_{nk}^{(d)}(R) \chi_k^{(d)}(t, R). \end{aligned} \quad (2.51)$$

The adiabatic representation was defined by having the electronic states being solutions to the electronic time-independent Schrödinger equation, making the adiabatic potential energy diagonal by design, but introducing off diagonal terms in the kinetic energy, the first- and second-order vibronic couplings, coming from the non-adiabaticity as the states change with the geometry. The diabatic representation on the other hand removes the off-diagonal kinetic terms making it more suitable for our numerical propagation of the nuclear dynamics, but it comes at the price of the potential energy no longer being diagonal.

2.4.3 An illustrative example of two adiabatic and diabatic curves

In this section we consider for simplicity a system consisting of two curves with a vibronic coupling and an avoided crossing. The system of only two curves is the simplest one can consider, but is still useful to illustrate the underlying aspects.

In an ab initio treatment of a real physical system, the approach is to obtain the properties of the molecule in the adiabatic representation through electronic structure theory calculation and transform these to the diabatic representation for simulating of the nuclear dynamics. In the case of model systems, as we will consider later in chap. 5, it is easier to start by defining the curves and couplings in the diabatic representation and transform to the adiabatic properties to see whether they resemble the properties of a real system.

For a system of two curves the diabatic potential matrix is of the form

$$\mathbf{V}^{(d)} = \begin{bmatrix} V_{11}^{(d)} & V_{12}^{(d)} \\ V_{12}^{(d)} & V_{22}^{(d)} \end{bmatrix}, \quad (2.52)$$

where we have assumed real electronic states such that matrix elements are all real and $V_{12}^{(d)} = V_{21}^{(d)}$. We can diagonalize the 2×2 matrix analytically at each value of the internuclear distance R to obtain the adiabatic curves

$$V_1^{(a)} = \frac{V_{11}^{(d)} + V_{22}^{(d)}}{2} - \frac{1}{2} \sqrt{[V_{22}^{(d)} - V_{11}^{(d)}]^2 + 4[V_{12}^{(d)}]^2} \quad (2.53)$$

$$V_2^{(a)} = \frac{V_{11}^{(d)} + V_{22}^{(d)}}{2} + \frac{1}{2} \sqrt{[V_{22}^{(d)} - V_{11}^{(d)}]^2 + 4[V_{12}^{(d)}]^2}. \quad (2.54)$$

In the limit of vanishing off-diagonal coupling $V_{12}^{(d)} \rightarrow 0$ the adiabatic curves reduce to the diabatic with the correspondence depending on the sign of $V_{22}^{(d)} - V_{11}^{(d)}$. This behaviour results in the adiabatic curves transforming from one diabatic state to the other over the range of the crossing. At the crossing point R_c of the two diabatic curves, we have $V_{11}^{(d)}(R_c) = V_{22}^{(d)}(R_c)$ and therefore get the splitting of the avoided crossing of the adiabatic curves to be

$$\Delta V_{21}^{(a)}(R_c) = V_2^{(a)}(R_c) - V_1^{(a)}(R_c) = 2|V_{12}^{(d)}(R_c)|. \quad (2.55)$$

Fig. 2.3 shows an illustration of two crossing diabatic curves and the resulting adiabatic curves calculated through Eq. (2.53) and Eq. (2.54) assuming a constant off-diagonal diabatic coupling. The figure clearly shows how the adiabatic curves initially agree with the diabatic before the crossing, repel at the crossing point leading to the avoided crossing and ends up agreeing with the opposite diabatic curve on the other side away from the crossing point.

For the system of two curves the transformation matrix Eq. (2.44) can, with the right boundary conditions, be chosen as a rotation matrix

$$\mathbf{U}(R) = \begin{bmatrix} \cos \alpha(R) & \sin \alpha(R) \\ -\sin \alpha(R) & \cos \alpha(R) \end{bmatrix}, \quad (2.56)$$

where $\alpha(R)$ is the mixing angle. It can be shown [27] that the first-order vibronic matrix element P_{12} can be found as the derivative of the angle

$$P_{12}(R) = \frac{\partial}{\partial R} \alpha(R). \quad (2.57)$$

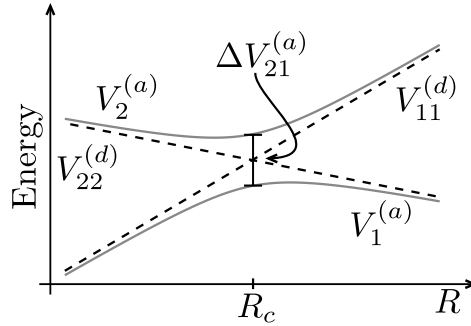


Figure 2.3: Illustration of diabatic (full gray lines) and adiabatic (dotted black lines) curves for a simple two-level model with diagonal diabatic terms depending linearly on the distance R and a constant off-diagonal diabatic coupling $V_{12}^{(d)}$.

For the simplified case where the off-diagonal element is constant the vibronic coupling P_{12} can be found to be

$$P_{12}(R) = \frac{V_{12}^{(d)}}{[V_{22}^{(d)} - V_{11}^{(d)}]^2 + [2V_{12}^{(d)}]^2} \frac{\partial}{\partial R} (V_{22}^{(d)} - V_{11}^{(d)}). \quad (2.58)$$

For the case where the diagonal diabatic curves are linear, such that the derivative of their difference is constant, the coupling is given by a Lorentzian. If the curves are only approximately linear the coupling will still be mostly Lorentzian, but with a change to the amplitude, and similarly if the diabatic coupling $V_{12}^{(d)}$ is only changing slowly over the area of the crossing, the coupling P_{12} mostly keeps its Lorentzian form. The Lorentzian form of the coupling is in agreement with what has been observed in the literature (see ref. [42] and ref. [43]), and what we observe from numerical studies in the model system considered in chap. 5.

In Fig. 2.4 we show in (a) the adiabatic and diabatic curves, (b) the mixing angle and (c) the vibronic coupling P_{12} for the curves in Fig. 2.3 for a larger interval of the internuclear distance. For the potential energy curves we see even more clearly how the diabatic and adiabatic curves will agree far away from the coupling. This is further manifested in the mixing angle which smoothly changes from $\alpha = 0$ to $\alpha = -\pi/2$ as it passes over the crossing point, corresponding to the curves switching. Fig. 2.4 also shows how the coupling is most important at the crossing, and falls off quickly as the curves move away from each other.

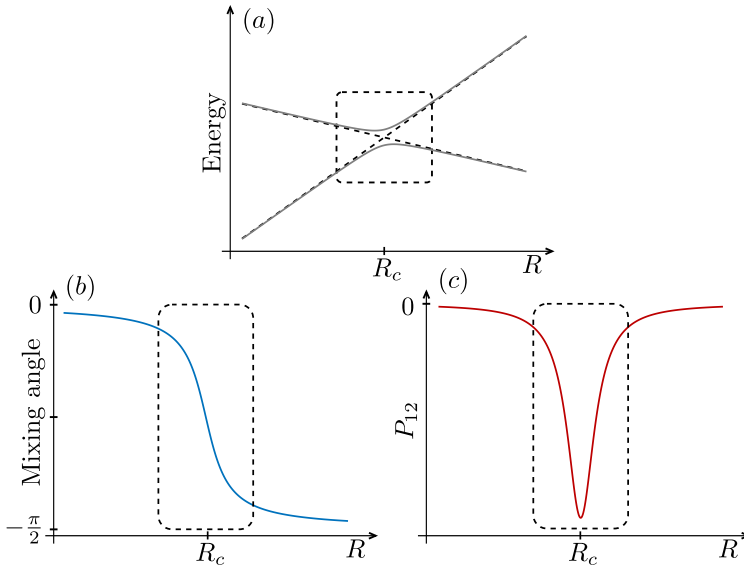


Figure 2.4: (a) Diabatic and adiabatic curves. (b) Mixing angle of transformation matrix $\alpha(R)$. (c) First-order vibronic coupling matrix element $P_{12}(R)$. Dashed box corresponds to the interval of internuclear distance R in Fig. 2.3.

Another useful tool in the analysis of the nuclear dynamics at the crossing is the Landau-Zener formula [44]

$$\text{Prob}(1 \rightarrow 2) = 1 - e^{-2\pi q}, \quad (2.59)$$

which gives the probability of a transition from the first to the second diabatic state for a trajectory passing through the crossing. The formula is derived in a semiclassical model, where the diabatic coupling is assumed to be constant over the region where the transition occurs. The constant q is proportional to the square of the energy separation Eq. (2.55)

$$q = \frac{[V_{12}^{(d)}]^2}{|a|}, \quad (2.60)$$

and inversely proportional to the parameter

$$a = \left\{ \frac{\partial}{\partial R} [V_{22}^{(d)} - V_{11}^{(d)}] \frac{\partial R}{\partial t} \right\}, \quad (2.61)$$

which depends linearly on the “velocity” $\partial R/\partial t$ of the classical path through the crossing. The interpretation of Eq. (2.59) is that a slow moving wave packet ($q \gg 1$) will have a large probability of changing diabatic states, or stay on the same adiabatic state, and that a fast moving wave packet ($q \ll 1$) will have a small probability of staying on the same diabatic state, or changing adiabatic state. The velocity of the nuclear wave packet should be compared with the energy separation of the adiabatic curves and the slope of the diabatic curves to determine which regime is valid.

Using the relation between the adiabatic and diabatic curves at the crossing Eq. (2.55), we see that the amplitude of the vibronic coupling is inversely proportional to the diabatic coupling at the crossing,

$$P_{12}(R_c) = \frac{\langle \Phi_1^{(a)} | \frac{\partial \hat{H}_{el}}{\partial R} | \Phi_2^{(a)} \rangle}{2 |V_{12}^{(d)}|}. \quad (2.62)$$

We note therefore that there are two ways of describing the strength of the coupling between the two curves. Either through the strength of the vibronic coupling P_{12} , which acts in the adiabatic representation, or through the strength of the diabatic coupling $V_{12}^{(d)}$, which acts in the diabatic representation. But since these are (roughly) inverse proportional to each other, it is most clear if we stick to one convention. When we consider our model system in chap. 5, we construct the curves initially in the diabatic representation and transform these to the adiabatic representation, where we will further completely neglect the vibronic coupling, and it is therefore most natural for us to choose the diabatic representation as our standard convention.

2.5 Fundamental Features of the ATA spectra

The spectrograms of ATAS contain multiple features that characterize the different underlying processes in the system. In the case of atoms, the dynamics are simpler and more analytical result can be obtained. Many of the same features are nonetheless also present for the more complicated case of molecules, and the features can be described by similar processes. There is, however, a significant difference between the atomic and molecular systems, since the nuclear motion must be taken into account in the case of a molecule and can not be neglected if one wants the full picture [19].

The shape of the potential energy curves of the system plays an important role, since it determines the movement of the excited nuclear

wave packet as we illustrated in Fig. 2.2. For dissociative excited curves the excited wave packet will move towards larger values of the nuclear coordinate R , and thereby move outside the Franck-Condon window of the ground state. This will effectively cut-off the dipole moment between ground and excited state, and will lead to broadening of the features, since the dipole now has less time to establish a signal.

The central features of the ATA spectra include the main absorption lines coming from direct transitions between the ground and a excited curve, hyperbolic sidebands along the main line [11], oscillating fringes [45] and the light-induced structures (LIS) [11, 20]. The sidebands are usually present at large negative delays, where the delay dependent signal stemming from a “waiting” time of the state excited by the XUV until the later arrival of the IR. The oscillating fringes are signals coming from quantum interferences between pathways of a direct excitation of the XUV with and initial excitation of the XUV and subsequent two IR photon absorption. The fringes will therefore be seen for negative delays, where the XUV arrives before the IR. The LIS are the result of non-linear processes stemming from the absorption of a XUV photon and the absorption or emission of a IR photon. The processes needed for the LIS involve both the XUV and the IR fields and can therefore only be seen in the part of the spectrum when the two pulses have a temporal overlap. Work on the LIS have previously been focused on atoms and homonuclear molecules, where the inversion symmetry forbids transitions between vibrational levels belonging to the same parity. In polar molecules this inversion symmetry is broken, leading to a change of the LIS and the creation of an additional ladder feature.

In the following we will present a series of simple models used to describe the different feature. The initial three-level model was proposed in ref. [11]. We adapted this to a two-level model to describe the features in a polar system in ref. [1], and will further extend it to describe multiple levels, which will be used later in the analysis of chap 5

2.5.1 Adiabatic Three-level Model

In ref. [11] an adiabatic three-level model was used to described the features of the ATA spectrum in an atomic system. We note here that “adiabatic” in this section, refers to the slow change of the dressed states with respect to the IR field, and not with the change of the internuclear distance, which is what was discussed earlier in sec. 2.2.3 and in sec. 2.4.

In the model the IR pulse is assumed to be slowly varying, such that the system follows the field adiabatically and the XUV field is assumed to

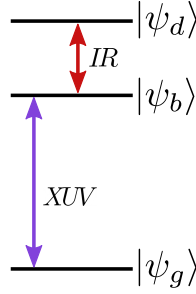


Figure 2.5: Sketch of the three-level system consisting of; a ground state $|\psi_g\rangle$, a bright state $|\psi_b\rangle$ and a dark state $|\psi_d\rangle$. The XUV pulse can couple the ground with the bright state, and the IR pulse can couple the bright and dark state.

be weak, such that it can be treated as a perturbation to first order. In the original formulation the three levels were atomic levels, but they could also be some of the vibrational levels of a molecule.

The three-level model consists, as the name suggest, of three separate levels; a ground state $|\psi_g\rangle$, and two excited states $|\psi_b\rangle$ and $|\psi_d\rangle$. The excited state $|\psi_b\rangle$, denoted the bright state, is coupled with the ground state through a dipole allowed transition, while the other excited state $|\psi_d\rangle$, the dark state, have no dipole allowed coupling with the ground state. We further assume that transitions between the bright and dark states is dipole allowed. See Fig. 2.5 for a sketch of the system.

The system starts in the ground state, and since we only consider the weak XUV pulse to first order, the XUV can effectively only couple the ground state and the bright state. The IR field is not strong enough to couple the excite state to the ground state through a multiphoton process, but it can couple the two excited states with each other. The effective Hamiltonian can therefore be written in the basis of the field-free states as

$$\hat{H} = \hat{H}_0 - F_{\text{IR}}\hat{D} - F_{\text{XUV}}\hat{D} \approx \begin{bmatrix} 0 & -F_{\text{XUV}}D_{gb} & 0 \\ -F_{\text{XUV}}D_{gb} & E_b & -F_{\text{IR}}D_{bd} \\ 0 & -F_{\text{IR}}D_{db} & E_d \end{bmatrix}, \quad (2.63)$$

where $D_{gb} = \langle\psi_g|\hat{D}|\psi_b\rangle$ and $D_{bd} = \langle\psi_b|\hat{D}|\psi_d\rangle$ are the only non-zero dipole moments.

Assuming that the system follows the slowly varying IR field adiabatically, we will express the full wave function with respect to the adiabatic

states defined by the time-independent Schrödinger equation

$$[\hat{H}_0 - F_{\text{IR}}(t)\hat{D}]|\psi_{ka}(t)\rangle = E_{ka}(t)|\psi_{ka}(t)\rangle. \quad (2.64)$$

As mentioned above we assume that the IR field only couples the two excited states, and the adiabatic Hamiltonian can therefore be written in the basis of the field-free states as

$$[\hat{H}_0 - F_{\text{IR}}\hat{D}] = \begin{bmatrix} E_b & -F_{\text{IR}}D_{bd} \\ -F_{\text{IR}}D_{bd} & E_d \end{bmatrix}. \quad (2.65)$$

This Hamiltonian can be diagonalized exactly yielding the adiabatic energies

$$E_{ba} = \frac{1}{2} \left\{ E_d + E_b - \sqrt{(E_d - E_b)^2 + 4D_{bd}^2 F_{\text{IR}}^2} \right\} \quad (2.66)$$

$$E_{da} = \frac{1}{2} \left\{ E_d + E_b + \sqrt{(E_d - E_b)^2 + 4D_{bd}^2 F_{\text{IR}}^2} \right\} \quad (2.67)$$

and the corresponding adiabatic states

$$|\psi_{ba}\rangle = \frac{E_d - E_{ba}}{\sqrt{D_{bd}^2 F_{\text{IR}}^2 + (E_d - E_{ba})^2}} |\psi_b\rangle + \frac{D_{bd} F_{\text{IR}}}{\sqrt{D_{bd}^2 F_{\text{IR}}^2 + (E_d - E_{ba})^2}} |\psi_d\rangle \quad (2.68)$$

$$|\psi_{da}\rangle = \frac{-D_{bd} F_{\text{IR}}}{\sqrt{D_{bd}^2 F_{\text{IR}}^2 + (E_{da} - E_b)^2}} |\psi_b\rangle + \frac{E_{da} - E_b}{\sqrt{D_{bd}^2 F_{\text{IR}}^2 + (E_{da} - E_b)^2}} |\psi_d\rangle. \quad (2.69)$$

The exact energies and states can be used to validate the model through numerical analysis, which was done in ref. [11].

To get analytical results for the response function we need simpler expressions, and we will thus restrict ourselves to work to second order in the IR field. This can be obtained either by expanding the exact equations above, or by using second order time-independent perturbation theory directly on the Hamiltonian, both yielding the same result. The former has the advantage that the expansion can more easily be compared with a numerical solution of the exact equation, but requires that an exact solution can actually be found. Perturbation theory on the other hand, has the advantage of not needing an exact solution as a starting point and can therefore be used later when we expand the model from three to multiple levels. Most textbooks stop their treatment of perturbation

theory at second order for the energy and first order for the states, but an expression for the second order states can be found in ref. [40]. We note that our use of time-independent perturbation theory is in accordance with the approximation that the states follow the IR field adiabatically.

To second order in the IR field the adiabatic energies are

$$E_{ba}(t) = E_b - \frac{D_{bd}^2 F_{\text{IR}}^2(t)}{E_d - E_b} \quad \text{and} \quad E_{da}(t) = E_d + \frac{D_{bd}^2 F_{\text{IR}}^2(t)}{E_d - E_b}. \quad (2.70)$$

To zero order in the field the energies reduces, as expected, to the field free energies. There is no linear term, but there is a second order term coming from the coupling between the bright and dark state. The corresponding eigenstates to second order are

$$|\psi_{ba}\rangle \approx \left(1 - \frac{1}{2} \frac{D_{bd}^2 F_{\text{IR}}^2}{(E_d - E_b)^2}\right) |\psi_b\rangle + \frac{D_{bd} F_{\text{IR}}}{E_d - E_b} |\psi_d\rangle \quad (2.71)$$

$$|\psi_{da}\rangle \approx -\frac{D_{bd} F_{\text{IR}}}{E_d - E_b} |\psi_b\rangle + \left(1 - \frac{1}{2} \frac{D_{bd}^2 F_{\text{IR}}^2}{(E_d - E_b)^2}\right) |\psi_d\rangle. \quad (2.72)$$

As was the case for the energies, the states reduces to the field free states at zero field. For the states there is both a linear term, mixing the dark state into the bright states and vice versa, as well as a quadratic term altering the field-free state further.

Using the adiabatic IR-dressed states we write the following ansatz for the wave function of the full system

$$|\Psi_a\rangle = a_g(t) |\psi_g\rangle + a_b(t) e^{-i \int_{\tau}^t dt' E_{ba}} |\psi_{ba}(t)\rangle + a_d(t) e^{-i \int_{\tau}^t dt' E_{da}} |\psi_{da}(t)\rangle. \quad (2.73)$$

Inserting this ansatz into the time-dependent Schrödinger equation with the full Hamiltonian Eq. (2.63), we get the following equations for the expansion coefficients

$$\dot{a}_b = i F_{\text{XUV}} \langle \psi_{ba} | \hat{D} | \psi_g \rangle e^{i \int_{\tau}^t dt' E_{ba}} a_b \quad (2.74)$$

$$- \langle \psi_{ba} | \dot{\psi}_{ba} \rangle a_b - \langle \psi_{ba} | \dot{\psi}_{da} \rangle e^{-i \int_{\tau}^t dt' E_{da} - E_{ba}} a_d \quad (2.75)$$

$$\dot{a}_d = i F_{\text{XUV}} \langle \psi_{da} | \hat{D} | \psi_g \rangle e^{i \int_{\tau}^t dt' E_{da}} a_g \quad (2.76)$$

$$- \langle \psi_{da} | \dot{\psi}_{ba} \rangle e^{i \int_{\tau}^t dt' E_{da} - E_{ba}} a_b - \langle \psi_{da} | \dot{\psi}_{da} \rangle a_d. \quad (2.77)$$

The first term describes the interaction with the XUV field between the ground state and the two states dressed by the IR field, while the last two

terms contain the non-adiabatic terms, which measures the change of the dressed states with respect to the change in the IR field over time. The term containing $\langle \psi_{ba} | \dot{\psi}_{ba} \rangle$ or $\langle \psi_{da} | \dot{\psi}_{da} \rangle$ is zero in our case since the dressed states are real, and the second term can be rewritten as

$$\langle \psi_{ba} | \dot{\psi}_{da} \rangle = -\frac{\dot{F}_{\text{IR}} \langle \psi_{ba} | \hat{D} | \psi_{da} \rangle}{E_{da} - E_{ba}} \quad (2.78)$$

$$\langle \psi_{da} | \dot{\psi}_{ba} \rangle = \frac{\dot{F}_{\text{IR}} \langle \psi_{da} | \hat{D} | \psi_{ba} \rangle}{E_{da} - E_{ba}}, \quad (2.79)$$

by taking the time-derivative of the Schrödinger equation defining the adiabatic states in Eq. (2.64). Neglecting these two terms constitute the adiabatic approximation [31], and it is justified since the IR field is assumed to vary slowly compared to the energy gap between the two states, i.e. that the change of the IR field over time is small compare to the dynamics of the states. Keeping only the first term in the two equations for the expansion coefficients and working to first order in the XUV field, with the initial condition that the system is purely in the ground state, we finally get the simplified equations

$$\dot{a}_b^{(1)} = iF_{\text{XUV}} \langle \psi_{ba} | \hat{D} | \psi_g \rangle e^{i \int_{\tau}^t dt' E_{ba}} \quad (2.80)$$

$$\dot{a}_d^{(1)} = iF_{\text{XUV}} \langle \psi_{da} | \hat{D} | \psi_g \rangle e^{i \int_{\tau}^t dt' E_{da}}. \quad (2.81)$$

The time-dependent dipole moment of the wave function Eq. (2.73) can be written, working only to first order in the coefficients, i.e. to first order in the XUV field

$$\langle D \rangle_a = a_b^{(1)} \langle \psi_g | \hat{D} | \psi_{ba} \rangle e^{-i \int_{\tau}^t dt' E_{ba}} + a_d^{(1)} \langle \psi_g | \hat{D} | \psi_{da} \rangle e^{-i \int_{\tau}^t dt' E_{da}} \quad (2.82)$$

$$+ [a_b^{(1)}]^* \langle \psi_{ba} | \hat{D} | \psi_g \rangle e^{i \int_{\tau}^t dt' E_{ba}} + [a_d^{(1)}]^* \langle \psi_{da} | \hat{D} | \psi_g \rangle e^{i \int_{\tau}^t dt' E_{da}}. \quad (2.83)$$

To calculate the response function Eq. (2.5) we need to take the Fourier transform of the dipole. The expression can be simplified, by noting that exponentials with positive phases will correspond to positive frequencies after the Fourier transform, while negative phases gives negative frequencies. The response function Eq. (2.5) is only evaluated for positive frequencies, and the negative frequencies in the dipole can therefore be ignored. We are then left with the expression

$$\langle D \rangle_a = [a_b^{(1)}]^* \langle \psi_{ba} | \hat{D} | \psi_g \rangle e^{i \int_{\tau}^t dt' E_{ba}} + [a_d^{(1)}]^* \langle \psi_{da} | \hat{D} | \psi_g \rangle e^{i \int_{\tau}^t dt' E_{da}}. \quad (2.84)$$

Remembering that the ground state $|\psi_g\rangle$ only couples to the field-free bright state $|\psi_b\rangle$, we get to second order in the IR field the two matrix elements

$$\langle\psi_{ba}|\hat{D}|\psi_g\rangle \approx d_{gb} \left(1 - \frac{1}{2} \frac{D_{bd}^2 F_{\text{IR}}^2}{(E_d - E_b)^2} \right) \quad (2.85)$$

$$\langle\psi_{da}|\hat{D}|\psi_g\rangle \approx -D_{gb} \frac{D_{bd} F_{\text{IR}}}{(E_d - E_b)}. \quad (2.86)$$

Similarly we can expand the exponential of the adiabatic energies

$$e^{i \int_{\tau}^t dt' E_{ba}} \approx \left(1 - i \frac{D_{bd}^2}{E_d - E_b} \int_{\tau}^t dt' F_{\text{IR}}^2(t') \right) e^{i E_b(t-\tau)} \quad (2.87)$$

$$e^{i \int_{\tau}^t dt' E_{da}} \approx \left(1 + i \frac{D_{bd}^2}{E_d - E_b} \int_{\tau}^t dt' F_{\text{IR}}^2(t') \right) e^{i E_d(t-\tau)}. \quad (2.88)$$

We have now established the adiabatic model, and the differential equations Eq. (2.80) and Eq. (2.81) can be solved numerically by using the approximative results Eq. (2.70), Eq. (2.85) and Eq. (2.86). This was done in ref. [11] to validate the model, and will not be repeated here.

To get an analytical expression instead, we used the further approximation that the short XUV pulse can be written as a delta function in time

$$F_{\text{XUV}}(t - \tau) \rightarrow \gamma \delta(t - \tau), \quad (2.89)$$

where the constant γ is related to the intensity of the field. The approximation is valid if the duration of the XUV is much shorter compared to the change of the IR field and the natural time scale of the field-free system.

Solving the equations for the coefficients Eq. (2.80) and Eq. (2.81) can now be done exactly and yields

$$a_b^{(1)} = \int_{\tau}^t dt' \dot{a}_b^{(1)} = i\gamma\theta(t - \tau) D_{gb} \left(1 - \frac{1}{2} \frac{D_{bd}^2 F_{\text{IR}}^2(\tau)}{(E_d - E_b)^2} \right) \quad (2.90)$$

$$a_d^{(1)} = \int_{\tau}^t dt' \dot{a}_d^{(1)} = -i\gamma\theta(t - \tau) D_{gb} \frac{D_{bd} F_{\text{IR}}(\tau)}{(E_d - E_b)}, \quad (2.91)$$

whith $\theta(t - \tau)$ being the Heaviside step function. We consider the two terms of the dipole moment in Eq. (2.84) separately, since it will later be clear that they correspond to different features.

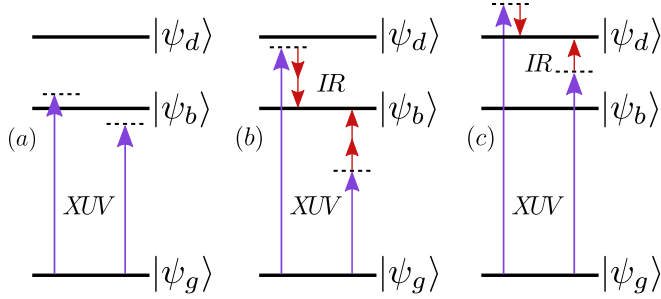


Figure 2.6: Sketch of the processes that gives rise to the three different main features of ATAS spectra. (a) Hyperbolic sidebands centered around the main absorption line of the bright state. (b) Oscillating fringes centered two IR away from the main absorption line of the bright state. (c) LIS centered one IR away from the dark state. We note that both the bright and the dark states are necessary for all of the three features to be present.

For the first term, describing the interaction between the ground state and the IR dressed bright state, we have

$$\begin{aligned}
 \langle D \rangle_{a1} &= [a_b^{(1)}]^* \langle \psi_{ba} | \hat{D} | \psi_g \rangle e^{i \int_{\tau}^t dt' E_{ba}} \\
 &\approx -i\gamma\theta(t - \tau) D_{gb}^2 e^{iE_b(t-\tau)} \\
 &\quad \times \left(1 - \frac{1}{2} \frac{D_{bd}^2 [F_{\text{IR}}^2(t) + F_{\text{IR}}^2(\tau)]}{(E_d - E_b)^2} - i \frac{D_{bd}^2}{E_d - E_b} \int_{\tau}^t dt' F_{\text{IR}}^2(t') \right),
 \end{aligned} \tag{2.92}$$

$$\tag{2.93}$$

to second order in the IR field. To calculate the response function we need the Fourier transform of the dipole moment.

Before the Fourier transform is performed the dipole moment will usually be multiplied by a Window function $W(t - t_w)$, used to dampen the signal and emulate the effect of decoherence (see discussion in sec. 3.4). To continue with the analytical model we will neglect the Window function and we set the step function to one $\theta(t - \tau) \rightarrow 1$. The effect of this approximation is described in detail in ref. [11]. We will further drop the terms in the dipole moment that only depends trivially on time through the phase $e^{iE_b(t-\tau)}$. These terms are responsible for the main absorption line, and as this feature is well understood there is no need to included them. The Fourier transform of the remaining dipole is calculated in detail in appendix A.

The resulting response function is therefore finally

$$\begin{aligned}
S_{a1}(\omega, \tau) = & - \frac{\sqrt{\pi}\gamma^2\rho D_{gb}^2 D_{bd}^2 F_{0,\text{IR}}^2 T_{\text{IR}}}{4\sqrt{2}(E_d - E_b)c} \left[\frac{1}{\omega - E_b} + \frac{1}{2(E_d - E_b)} \right] \\
& \times \omega \cos [(E_b - \omega)\tau] \\
& \times \left[\exp\left(-\frac{T_{\text{IR}}^2(\omega - E_b - 2\omega_{\text{IR}})^2}{32}\right) + \exp\left(-\frac{T_{\text{IR}}^2(\omega - E_b + 2\omega_{\text{IR}})^2}{32}\right) \right. \\
& \left. - 2 \exp\left(-\frac{T_{\text{IR}}^2(\omega - E_b)^2}{32}\right) \right]. \tag{2.94}
\end{aligned}$$

This equation describes the hyperbolic sidebands and the oscillating fringes. As mentioned above it comes from the interaction between the ground state and the bright dressed state. The two terms we Fourier transformed, the square of the IR field and the time integral over the square of the IR field, comes from the matrix element of the dipole between the ground state and the dressed state Eq. (2.85) and the exponential of the adiabatic energy Eq. (2.87) respectively. The first give rise to the $(E_d - E_b)^{-1}$ term, which is always positive, while the second gives the term $(\omega - E_b)^{-1}$, which changes sign depending on the magnitude of ω . For $\omega > E_b$ the two term interfere constructively and for $\omega < E_b$ they interfere destructively, leading to an asymmetrically signal around E_b . The three Gaussian functions indicate the positions of the features centered around the bright state, E_b , for the hyperbolic sidebands and two IR away from the bright state, $E_b \pm 2\omega_{\text{IR}}$, for the oscillating fringes. See Fig. 2.6 for a sketch of the positions of the features. The two IR frequencies comes from the square of the IR carrier, $\sin(\omega_{\text{IR}}t)$, and working to higher order we would therefore expect additional features further away from the bright state, probably an even multiple away from the bright state due to the dipole transition rules. Without the carrier of the IR field, the fringes would therefore disappear, but the sidebands would still be present with only the envelope left. Increasing the width of the IR envelope, giving by the duration, T_{IR} , of the field, increases the amplitude of the signal linearly and narrows the features, since the longer pulse gives more energy to the system and has a more well defined frequency. The delay dependence of the signal comes through the factor, $\cos[(E_b - \omega)\tau]$, and causes a modulation of the features. To get a clearer understanding of this dependence on the time delay, we can consider how this cosine behaves for photon energies centered

around the different features, represented here by the small detuning δ ,

$$\cos [(E_b - \omega)\tau] = \begin{cases} \cos(\delta\tau), & \text{for sidebands with} \\ & \omega = E_b + \delta \\ \cos [(2\omega_{\text{IR}} \pm \delta)\tau], & \text{for fringes with} \\ & \omega = E_b \pm 2\omega_{\text{IR}} + \delta. \end{cases} \quad (2.95)$$

For the sidebands we get oscillations with a small frequency, δ , and there is almost no modulation for fixed ω . If we instead consider the curves traced out by constant argument, $\delta\tau = \text{const.}$, we see that this gives rise to hyperbolic lines. A spectrum showing the part of the response function responsible for the hyperbolic sidebands can be seen in Fig. 2.7. For the oscillating fringes we get oscillations with a frequency around $2\omega_{\text{IR}}$, i.e. half the period of the IR carrier. Finally we note that the response function depends both on the dipole moment between the ground and the bright state as well as the dipole moment between the bright and dark state, meaning that all three states are necessary for the features to be present. The analytical expressions for the sidebands and fringes are symmetrical around zero delay, where in reality they will not be present for positive delays as the process needed for their establishment rely on the XUV arriving before the IR. The discrepancy comes from the approximation used when we simplified the dipole in Eq. (2.93) by letting $\theta(t - \tau) \rightarrow 1$, and this must be kept in mind when comparing with more accurate spectra.

For the second term in the dipole Eq. (2.84), which is from the interaction of the ground state with the dressed dark state, we have

$$\langle D \rangle_{a2} = [a_d^{(1)}]^* \langle \psi_{da} | \hat{D} | \psi_g \rangle e^{i \int_{\tau}^t dt' E_{da}} \quad (2.96)$$

$$\approx -i\gamma\theta(t - \theta) D_{gb}^2 D_{bd}^2 \frac{F_{\text{IR}}(\tau) F_{\text{IR}}(t)}{(E_d - E_b)^2} e^{iE_d(t-\tau)}, \quad (2.97)$$

to second order in the IR field. Following the same approach as above, where we set $\theta(t - \tau) \rightarrow 1$ and ignore the window function, we arrive at the response function (again the calculation of the appropriate Fourier transforms are given in appendix A)

$$S_{a2}(\omega, \tau) = \frac{\sqrt{\pi}\gamma^2 \rho D_{gb}^2 D_{bd}^2 F_{0,\text{IR}}^2 T_{\text{IR}}}{2c(E_d - E_b)^2} \exp\left(-\frac{4\tau^2}{T_{\text{IR}}^2}\right) \omega \sin(\omega_{\text{IR}}\tau) \sin[(E_d - \omega)\tau] \\ \times \left[\exp\left(-\frac{T_{\text{IR}}^2(\omega - E_d - \omega_{\text{IR}})^2}{16}\right) - \exp\left(-\frac{T_{\text{IR}}^2(\omega - E_d + \omega_{\text{IR}})^2}{16}\right) \right]. \quad (2.98)$$

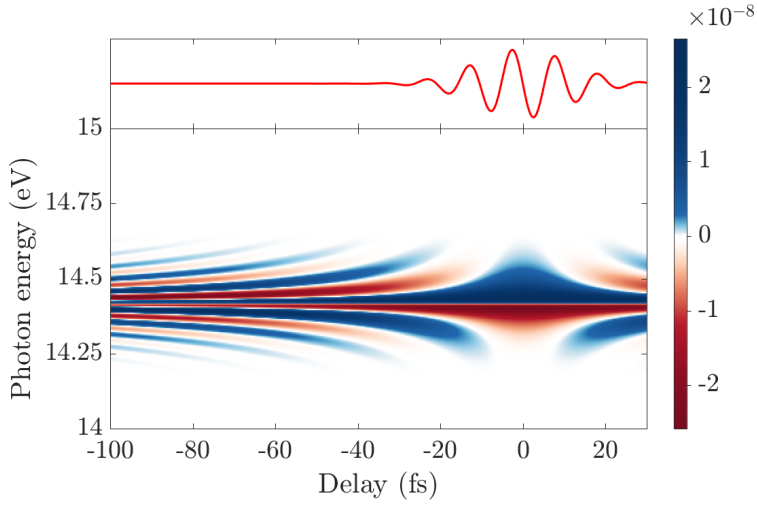


Figure 2.7: Example of Hyperbolic sidebands calculated using (part of) the analytical response function in Eq. (2.94). In a real spectrum the sidebands would be harder to see due to the much brighter main absorption line which is situated at the same photon energy. The top panel depicts the IR pulse centered at $\tau = 0$ fs.

This equation describes the LIS, and comes from the interaction of the ground state with the IR dressed dark state. Contrary to the response function of the sidebands and fringes in Eq. (2.94), this comes entirely from the dipole between the ground and the dressed state Eq. (2.86) and the exponential of the adiabatic energy Eq. (2.88) only contributes with the field free term $e^{iE_d(t-\tau)}$. In this equation there are two Gaussians centered one IR away from the dark state, $E_d \pm \omega_{\text{IR}}$ giving the position of the LIS, see Fig. 2.6. This comes from the Fourier transform of the IR field to the first power, and as was the case for the fringes, there would be no signal to this order without the carrier term $\sin(\omega_{\text{IR}}t)$. There is the same dependence on the duration of the IR field, where longer duration leads to stronger and more narrow features. The presence of the IR field evaluated at the delay time, see Eq. (2.97), gives another Gaussian, which centers the features at zero delay, and sine factor oscillating with the IR

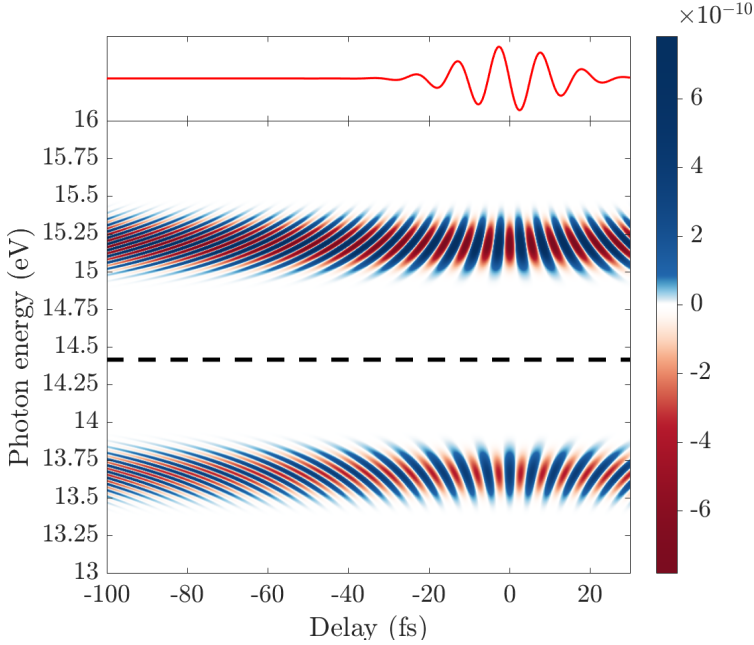


Figure 2.8: Example of oscillating fringes calculated using (part of) the analytical response function Eq. (2.94). Note the asymmetry of the features around the bright state indicated by the dashed line. The top panel depicts the IR pulse centered at $\tau = 0$ fs.

frequency. Looking closer at the oscillating term of the two sine functions

$$\begin{aligned} & \sin(\omega_{\text{IR}}\tau) \sin[(E_d - \omega)\tau] \\ &= \frac{1}{2} \left\{ \cos[(E_d - \omega_{\text{IR}} - \omega)\tau] - \cos[(E_d + \omega_{\text{IR}} - \omega)\tau] \right\} \end{aligned} \quad (2.99)$$

$$= \frac{1}{2} \left\{ \pm \cos[(2\omega_{\text{IR}} \pm \delta)\tau] \mp \cos(\delta\tau) \right\}, \quad (2.100)$$

for LIS with $\omega = E_d \pm \omega_{\text{IR}} + \delta$

we see that, like in the case of the fringes, we find an oscillation at twice the IR frequency. Again we note the dependence on both d_{gb} and d_{bd} such that both the bright and the dark states are necessary. We note that the sign difference between the last two Gaussians in Eq. (2.98) is offset by the sign coming from the sine functions in Eq. (2.99) such that the features are symmetric around the dark state.

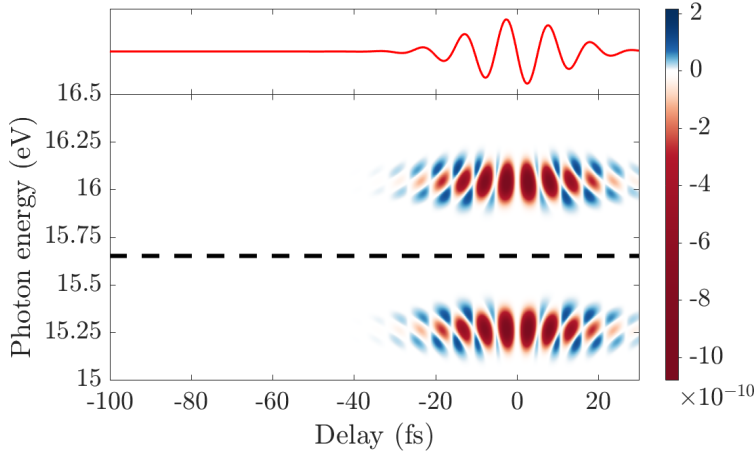


Figure 2.9: Example of the LIS calculated using the analytical response function in Eq. (2.98). Note the symmetry of the features around the dark state indicated by the dashed line. The top panel depicts the IR pulse centered at $\tau = 0$ fs.

2.5.2 Expanding the Three-level Model to multiple levels

In this section we expand the adiabatic three-level model to include a manifold of bright $\{|\psi_{b,n}\rangle\}$ and dark $\{|\psi_{d,m}\rangle\}$ states. In practice this could be a molecular system, where we consider multiple vibrational levels of two excited state curves, one bright and one dark with respect to the ground state. Description of LIS using an expansion in vibrational states have previously been explored in a simpler model in ref. [19] and ref. [20]. A sketch of the model system is shown in Fig. 2.10.

We follow the same procedure as in sec. 2.5.1 and consider the adiabatic states dressed by the IR field to second order. We keep the derivation here brief as it is nearly identical to what was done in the previous section, and refer to appendix B for more detail.

The ground state is coupled by the XUV field to the bright state manifold and the IR field couples the bright with the dark manifold.

The adiabatic energies corresponding to Eq. (2.70) are

$$E_{ba,n} = E_{b,n} - \sum_m \frac{D_{b,n;d,m}^2 F_{\text{IR}}^2}{E_{d,m} - E_{b,n}} \quad (2.101)$$

$$E_{da,m} = E_{d,m} + \sum_n \frac{D_{b,n;d,m}^2 F_{\text{IR}}^2}{E_{d,m} - E_{b,n}}, \quad (2.102)$$

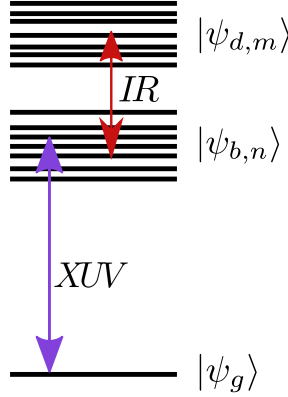


Figure 2.10: Sketch of the multilevel system consisting of a ground state $|\psi_g\rangle$ together with a manifold of bright states $\{|\psi_{b,n}\rangle\}$ and a manifold of dark states $\{|\psi_{d,m}\rangle\}$. The ground state is coupled by the XUV field to the bright state manifold and the IR field couples the bright with the dark manifold.

where the energies are now altered by all the other states of the opposite manifold, but there is no contribution from states inside the same manifold, i.e. it is a simple linear extension of Eq. (2.70). The corresponding adiabatic states, compared to Eq. (2.71) and Eq. (2.72), are

$$\begin{aligned}
 |\psi_{ba,n}\rangle = & \left(1 - \frac{1}{2} \sum_m \frac{D_{b,n;d,m}^2 F_{\text{IR}}^2}{(E_{d,m} - E_{b,n})^2}\right) |\psi_{b,n}\rangle + \sum_m \frac{D_{b,n;d,m} F_{\text{IR}}}{E_{d,m} - E_{b,n}} |\psi_{d,m}\rangle \\
 & + \sum_m \sum_{k \neq n} \frac{D_{b,k;d,m} D_{b,n;d,m} F_{\text{IR}}^2}{(E_{d,m} - E_{b,n})(E_{b,k} - E_{b,n})} |\psi_{b,k}\rangle \quad (2.103)
 \end{aligned}$$

and

$$\begin{aligned}
 |\psi_{da,m}\rangle = & - \sum_n \frac{D_{b,n;d,m} F_{\text{IR}}}{E_{d,m} - E_{b,n}} |\psi_{b,n}\rangle + \left(1 - \frac{1}{2} \sum_n \frac{D_{b,n;d,m}^2 F_{\text{IR}}^2}{(E_{d,m} - E_{b,n})^2}\right) |\psi_{d,m}\rangle \\
 & + \sum_n \sum_{l \neq m} \frac{D_{b,n;d,m} D_{b,n;d,l} F_{\text{IR}}^2}{(E_{d,m} - E_{b,n})(E_{d,m} - E_{d,l})} |\psi_{d,l}\rangle. \quad (2.104)
 \end{aligned}$$

As with the adiabatic energies, we see that the states are now coupled to all the other states of the opposite manifold, such that we get a sum over similar terms as in Eq. (2.71) and Eq. (2.72), but we also get an additional sum for each of the states which couples the states inside the same manifold mediated by the other manifold, i.e. two different bright

states coupled through a dark state or vice versa. We will refer to the terms coupling between different manifolds as inter-manifold, and terms coupling inside the same manifold as intra-manifold. When we calculate the dressed dipole matrix elements, similar to Eq. (2.85) and Eq. (2.86), the only parts of the dressed states that contributes are the ones made from the field-free bright states. For the dressed bright states, $|\psi_{ba,n}\rangle$, both the inter- and the intra-manifold term will contribute, while for the dressed dark states, $|\psi_{da,m}\rangle$, only the inter-manifold term contributes.

Following the same procedure as in sec. 2.5.1, we write the full wave function in the basis of the adiabatic states and work to first order in the XUV field, we find the two response functions analogous to Eq. (2.94) and Eq. (2.98).

The first response function describing the oscillating fringes and hyperbolic sidebands in the multilevel model is

$$\begin{aligned}
S_{a1}(\omega, \tau) = & - \sum_n \sum_m \frac{\sqrt{\pi}\gamma^2 \rho D_{g;b,n}^2 D_{b;n;d,m}^2 F_{0,\text{IR}}^2 T_{\text{IR}}}{4\sqrt{2}(E_{d,m} - E_{b,n})c} \left[\frac{1}{\omega - E_{b,n}} + \frac{1}{2(E_{d,m} - E_{b,n})} \right] \\
& \times \omega \cos[(E_{b,n} - \omega)\tau] \\
& \times \left[\exp\left(-\frac{T_{\text{IR}}^2(\omega - E_{b,n} - 2\omega_{\text{IR}})^2}{32}\right) + \exp\left(-\frac{T_{\text{IR}}^2(\omega - E_{b,n} + 2\omega_{\text{IR}})^2}{32}\right) \right. \\
& \quad \left. - 2 \exp\left(-\frac{T_{\text{IR}}^2(\omega - E_{b,n})^2}{32}\right) \right] \\
& + \sum_n \sum_m \sum_{k \neq m} \frac{\sqrt{\pi}\gamma^2 \rho D_{g;b,n} D_{g;b,k} D_{b,k;d,m} D_{b;n;d,m} F_{0,\text{IR}}^2 T_{\text{IR}}}{2\sqrt{2}(E_{d,m} - E_{b,n})(E_{b,k} - E_{b,n})c} \\
& \times \omega \cos[(E_{b,n} - \omega)\tau] \\
& \times \left[\exp\left(-\frac{T_{\text{IR}}^2(\omega - E_{b,n} - 2\omega_{\text{IR}})^2}{32}\right) + \exp\left(-\frac{T_{\text{IR}}^2(\omega - E_{b,n} + 2\omega_{\text{IR}})^2}{32}\right) \right. \\
& \quad \left. - 2 \exp\left(-\frac{T_{\text{IR}}^2(\omega - E_{b,n})^2}{32}\right) \right]. \tag{2.105}
\end{aligned}$$

The first term, stemming from the inter-manifold coupling, is just a linear generalization of the three-level model, where the double sum run over all possible combination of three-level systems in the two manifolds. The second term is almost identical to the second part of the first term, the difference being the dipole moments in the numerator and the energies in the denominator are from two different bright states. An important part being that we get the difference in energy between the two bright

states, $(E_{d,m} - E_{b,k})^{-1}$, which will in general be much smaller than the difference between the energy of a bright and a dark state, and can therefore potentially give a much stronger signal.

The second response function responsible for the LIS is now

$$\begin{aligned}
S_{a2}(\omega, \tau) = & \sum_n \sum_m \frac{\sqrt{\pi}\gamma^2 \rho D_{g;b,n}^2 D_{b;n;d,m}^2 F_{0,\text{IR}}^2 T_{\text{IR}}}{2c(E_{d,m} - E_{b,n})^2} \exp\left(-\frac{4\tau^2}{T_{\text{IR}}^2}\right) \\
& \times \omega \sin(\omega_{\text{IR}}\tau) \sin[(E_{d,m} - \omega)\tau] \\
& \times \left[\exp\left(-\frac{T_{\text{IR}}^2(\omega - E_{d,m} - \omega_{\text{IR}})^2}{16}\right) - \exp\left(-\frac{T_{\text{IR}}^2(\omega - E_{d,m} + \omega_{\text{IR}})^2}{16}\right) \right] \\
+ & \sum_n \sum_m \sum_{k \neq n} \frac{\sqrt{\pi}\gamma^2 \rho D_{g;b,n} D_{g;b,k} D_{b;n;d,m} D_{b;k;d,m} F_{0,\text{IR}}^2 T_{\text{IR}}}{2c(E_{d,m} - E_{b,n})(E_{d,m} - E_{b,k})} \exp\left(-\frac{4\tau^2}{T_{\text{IR}}^2}\right) \\
& \times \omega \sin(\omega_{\text{IR}}\tau) \sin[(E_{d,m} - \omega)\tau] \\
& \times \left[\exp\left(-\frac{T_{\text{IR}}^2(\omega - E_{d,m} - \omega_{\text{IR}})^2}{16}\right) - \exp\left(-\frac{T_{\text{IR}}^2(\omega - E_{d,m} + \omega_{\text{IR}})^2}{16}\right) \right].
\end{aligned} \tag{2.106}$$

The first term is again a sum over the three-level response function Eq. (2.106), where we run over all the possible different three-level subsystems. The second term is exactly the same as the first, but now containing two different bright states. We could have written both terms together, but chose to separate them to highlight the comparison with the three-level case.

2.6 Two-level Model for a system with a permanent dipole

In ref. [1] we considered the two lowest potential energy curves of the diatomic LiF molecular system, a heteronuclear molecule have a permanent dipole. Numerical investigations, which will be examined later in sec. 4.2, showed additional features of the ATAS spectrum. To gain more insight into the physics behind these, we introduced a modification of the adiabatic three-level model. In the LiF system we only consider two levels, one representing each of the two curves. The presence of the permanent dipole complicates the description of the system, since interactions of a single energy level with the IR and XUV fields are now possible. The derivation of analytical expressions will therefore not be as straight forward as earlier.

The system we consider consist of two energy levels coupled by an XUV and an IR field. As every transition is dipole allowed we drop the notion of bright and dark states, and refer instead to the two states as E_1 and E_2 . As both fields can couple the two levels with each other and with themselves, the full Hamiltonian of the system can be written as

$$\hat{H} = \hat{H}_0 - F_{\text{IR}}\hat{d} - F_{\text{XUV}}\hat{d} \quad (2.107)$$

$$= \begin{bmatrix} E_1 - F_{\text{IR}}D_{11} - F_{\text{XUV}}D_{11} & -F_{\text{IR}}D_{12} - F_{\text{XUV}}D_{12} \\ -F_{\text{IR}}D_{12} - F_{\text{XUV}}D_{12} & E_1 - F_{\text{IR}}D_{11} - F_{\text{XUV}}D_{11} \end{bmatrix} \quad (2.108)$$

in the field free-basis.

We will employ a similar approach as in the three-level model, where we treat the two different fields in a separately way. The slowly changing NIR field is treated as an adiabatic parameter, and we will again expand the full wave function in the basis of the instantaneous adiabatic states defined by the time-independent Schrödinger equation

$$[\hat{H}_0 - F_{\text{IR}}(t)\hat{D}] |\phi_i(t)\rangle = E_{ia}(t) |\phi_i(t)\rangle, \quad (2.109)$$

with Hamiltonian

$$\hat{H} = \hat{H}_0 - F_{\text{IR}}\hat{D} = \begin{bmatrix} E_1 - F_{\text{IR}}D_{11} & -F_{\text{IR}}D_{12} \\ -F_{\text{IR}}D_{12} & E_2 - F_{\text{IR}}D_{22} \end{bmatrix}, \quad (2.110)$$

while the weak UV field is introduced as a small parameter through first-order time-dependent perturbation theory.

For the three-level model and its expansion we chose to use time-independent perturbation theory to find the dressed energies and states to second order in the IR field. This was done, since it was easier to generalize to multiple levels. In the case here, the permanent dipole, giving rise to diagonal dipole couplings makes the full treatment much more complicated. To describe a new ladder feature arising in the system due to the permanent dipole moment, we will later expand beyond second order in the NIR field. We will therefore instead diagonalize the Hamiltonian exact and later consider expansions to the needed order.

The exact adiabatic energies can be found to be

$$E_{1a} = \frac{1}{2} \left\{ E_2 - D_{22}F_{\text{IR}} + E_1 - D_{11}F_{\text{IR}} - \sqrt{\left[E_2 - E_1 - (D_{22} - D_{11})F_{\text{IR}} \right]^2 + 4D_{12}^2} \right\} \quad (2.111)$$

$$E_{2a} = \frac{1}{2} \left\{ E_2 - D_{22}F_{\text{IR}} + E_1 - D_{11}F_{\text{IR}} + \sqrt{\left[E_2 - E_1 - (D_{22} - D_{11})F_{\text{IR}} \right]^2 + 4D_{12}^2} \right\}. \quad (2.112)$$

Comparing with the exact energies for the three level model in Eq. (2.66) and Eq. (2.67) we see the diagonal dipole couplings altering both energies. We can also find the corresponding exact adiabatic states of the two dimensional system

$$|\psi_{1a}\rangle = \frac{E_2 - D_{22}F_{\text{IR}} - E_{1a}}{\sqrt{D_{12}^2 F_{\text{IR}}^2 + (E_2 - D_{22}F_{\text{IR}} - E_{1a})^2}} |\psi_1\rangle + \frac{D_{12}F_{\text{IR}}}{\sqrt{D_{12}^2 F_{\text{IR}}^2 + (E_{1a} - E_2 + D_{22}F_{\text{IR}})^2}} |\psi_2\rangle \quad (2.113)$$

$$|\psi_{2a}\rangle = \frac{-D_{12}F_{\text{IR}}}{\sqrt{D_{12}^2 F_{\text{IR}}^2 + (E_{1a} - E_2 + D_{22}F_{\text{IR}})^2}} |\psi_1\rangle + \frac{E_{2a} - E_1 + D_{11}F_{\text{IR}}}{\sqrt{D_{12}^2 F_{\text{IR}}^2 + (E_{1a} - E_2 + D_{22}F_{\text{IR}})^2}} |\psi_2\rangle, \quad (2.114)$$

which again are altered compared to the states in the three level model in Eq. (2.68) and Eq. (2.69).

Expanding these to second order in the IR field, which is equal to the result obtained from second order time-independent perturbation theory as we discussed earlier, we find the approximate energies

$$E_{1a} = E_1 - D_{11}F_{\text{IR}} - \frac{D_{12}^2 F_{\text{IR}}^2}{E_2 - E_1} \quad (2.115)$$

$$E_{2a} = E_2 - D_{22}F_{\text{IR}} + \frac{D_{12}^2 F_{\text{IR}}^2}{E_2 - E_1}. \quad (2.116)$$

We see that the presence of the diagonal dipole couplings, D_{11} and D_{22} , introduces an additional linear term for the two levels. For the states we

get the following expansions

$$|\psi_{1a}\rangle = \left(1 - \frac{1}{2} \frac{D_{12}^2 F_{\text{IR}}^2}{(E_2 - E_1)^2}\right) |\psi_1\rangle + \left(\frac{D_{12} F_{\text{IR}}}{E_2 - E_1} - \frac{(D_{11} - D_{22}) D_{12} F_{\text{IR}}^2}{(E_2 - E_1)^2}\right) |\psi_2\rangle \quad (2.117)$$

$$|\psi_{2a}\rangle = -\left(\frac{D_{12} F_{\text{IR}}}{E_2 - E_1} - \frac{(D_{11} - D_{22}) D_{12} F_{\text{IR}}^2}{(E_2 - E_1)^2}\right) |\psi_1\rangle + \left(1 - \frac{1}{2} \frac{D_{12}^2 F_{\text{IR}}^2}{(E_2 - E_1)^2}\right) |\psi_2\rangle. \quad (2.118)$$

To first order there is no change in the states, but we get an additional second order term dependent on the difference of the two diagonal dipoles, $D_{22} - D_{11}$.

The ansatz for the full system using the adiabatic states is now

$$|\Psi_a(t)\rangle = a_1(t) e^{-i \int_{t_0}^t dt' E_{1a}} |\psi_{1a}(t)\rangle + a_2(t) e^{-i \int_{t_0}^t dt' E_{2a}} |\psi_{2a}(t)\rangle, \quad (2.119)$$

and inserting this into the time-dependent Schrödinger equation with the full Hamiltonian Eq. (2.107), yields the equations

$$\begin{aligned} \dot{a}_1 = & iF_{\text{XUV}} \langle \psi_{1a} | \hat{D} | \psi_{1a} \rangle a_1 - \langle \psi_{1a} | \dot{\psi}_{2a} \rangle e^{-i \int_{t_0}^t dt' E_{2a} - E_{1a}} a_2 \\ & + iF_{\text{XUV}} \langle \psi_{1a} | \hat{D} | \psi_{2a} \rangle e^{-i \int_{t_0}^t dt' E_{2a} - E_{1a}} a_2 \end{aligned} \quad (2.120)$$

$$\begin{aligned} \dot{a}_2 = & iF_{\text{XUV}} \langle \psi_{2a} | \hat{D} | \psi_{2a} \rangle a_2 - \langle \psi_{2a} | \dot{\psi}_{1a} \rangle e^{i \int_{t_0}^t dt' E_{2a} - E_{1a}} a_1 \\ & + iF_{\text{XUV}} \langle \psi_{2a} | \hat{D} | \psi_{1a} \rangle e^{i \int_{t_0}^t dt' E_{2a} - E_{1a}} a_1, \end{aligned} \quad (2.121)$$

with the initial condition of all the population in the ground state, $a_1(t_0) = 1$ and $a_2(t_0) = 0$.

To zeroth order in the XUV field the two coefficients stay constant, while to first order they follow the equations

$$\dot{a}_1^{(1)} = iF_{\text{XUV}} \langle \psi_{1a} | \hat{D} | \psi_{1a} \rangle \quad (2.122)$$

$$\dot{a}_2^{(1)} = iF_{\text{XUV}} \langle \psi_{2a} | \hat{D} | \psi_{1a} \rangle e^{i \int_{t_0}^t dt' E_{2a} - E_{1a}}, \quad (2.123)$$

if we again neglect the non-adiabatic terms containing $\langle \psi_{1a} | \dot{\psi}_{2a} \rangle$ and $\langle \psi_{2a} | \dot{\psi}_{1a} \rangle$. The difference, if we compare with the three-level model, is that the ground state itself is altered.

The time-dependent dipole moment of the full wave function is

$$\langle \Psi_a | \hat{D} | \Psi_a \rangle = |a_1|^2 \langle \psi_{1a} | \hat{D} | \psi_{1a} \rangle + 2\text{Re} \left[a_1^* a_2 \langle \psi_{1a} | \hat{D} | \psi_{2a} \rangle e^{-i \int_{t_0}^t dt' E_{2a} - E_{1a}} \right], \quad (2.124)$$

where we ignore the term with the factor $|a_2|^2$, since this is second order in the XUV and therefore much smaller than the other two terms. Compared with the three-level model, we now have just one term describing interference of ground and excited state, since there is only one excited state, but we also retain the term of the ground states interaction with itself.

2.6.1 Light-induced structures

In the three-level model the LIS was seen to arise from the interaction of the ground state with the dark state, while the interaction of the ground with the bright state gave the oscillating fringes and the hyperbolic sidebands. Due to the dipole transition rules, the features must come from a process involving an odd or an even number of photons respectively. In the system with a permanent dipole, the distinction between bright and dark states become meaningless, since all transitions are now allowed.

We therefore look at the second term in Eq. (2.124), which describe the interaction with the excited state

$$\langle \hat{D} \rangle_{\text{LIS}} = 2\text{Re} \left[a_2 \langle \psi_{1a} | \hat{D} | \psi_{2a} \rangle e^{-i \int_{t_0}^t dt' E_{2a} - E_{1a}} \right]. \quad (2.125)$$

We have used here that to first order in the XUV the product of the two coefficients is $a_1^* a_2 = a_2$.

Due to the much more complicated expressions for the adiabatic energies and states, we will not include all terms or calculate fully analytical expressions since this was done in the three-level case. We will instead simplify and using numerical solutions to investigate which term give rise to the relevant features.

We first need to find the expansion coefficient of the excited state, a_2 , which is found by integration of Eq. (2.123)

$$a_2^{(1)} = i \int_{t_0}^t dt' F_{\text{XUV}}(t') \langle \psi_{2a} | \hat{D} | \psi_{1a} \rangle e^{i \int_{t_0}^{t'} dt'' E_{2a} - E_{1a}}. \quad (2.126)$$

In the three-level model this equation was solved by approximating the XUV as a delta function. In the case here we will keep the form of the UV, but still use that the duration of the UV is again much shorter than the

oscillations of the NIR pulse and the dynamics of the system. Under this condition the time dependence of the terms in the integrand are of less importance compare to the constant part and we assume

$$\langle \psi_{2a} | \hat{D} | \psi_{1a} \rangle \approx D_{12} \quad (2.127)$$

for the dipole element and

$$e^{-i \int_{t_0}^t dt' E_{2a} - E_{1a}} \approx e^{-i(E_2 - E_1)(t - t_0)} \quad (2.128)$$

for the phase, thus the coefficient becomes

$$a_2^{(1)} = iD_{12} \int_{t_0}^t dt' F_{XUV}(t') e^{i(E_2 - E_1)(t' - t_0)}. \quad (2.129)$$

Numerical investigation further showed that for the given parameters, the term contributing most to the LIS of the two remaining terms is the exponential of the adiabatic energies, giving the dipole moment

$$\langle \hat{D} \rangle_{\text{LIS}} = 2D_{12}^2 \text{Re} \left[e^{-i \int_{t_0}^t dt' E_{2a} - E_{1a}} \int_{t_0}^t dt' F_{XUV}(t') e^{i(E_2 - E_1)(t' - t_0)} \right]. \quad (2.130)$$

Lastly we expand the exponential to second order in the NIR field

$$\begin{aligned} e^{-i \int_{t_0}^t dt' E_{2a} - E_{1a}} &\approx e^{-i(E_2 - E_1)(t - t_0)} \\ &\times \left[1 + i(D_{22} - D_{11}) \int_{t_0}^t dt' F_{\text{IR}} \right. \\ &\quad \left. - \frac{1}{2}(D_{22} - D_{11})^2 \left(\int_{t_0}^t dt' F_{\text{IR}} \right)^2 \right], \quad (2.131) \end{aligned}$$

where we neglect the second order term, $-iD_{12}^2/(E_2 - E_1) \int_{t_0}^t dt' F_{XUV}^2(t')$.

Inserting this into Eq. (2.130) now constitute the adiabatic model describing the LIS features for the system considered. Further numerical analysis is given later, when we consider it applied to the two lowest energy curves of the LiF molecule.

2.6.2 Ladder structures

From the full numerical simulation of the molecule with a permanent dipole moment, and additional new ladder-like structure consisting of features

separated by one IR photon like the rungs of a ladder was observed in the ATAS spectrum.

Numerical studies showed that the dynamics leading to the ladder were independent on the presence of the UV pulse, although it is still included in the calculation of the response function Eq. (2.5). This corresponds to a somewhat strange experimental setup, where the system only interact with the IR field, but the generated field still interferes with the UV pulse. We do not propose such an experiment, but use the formalism to aid or description of the features.

Returning to the full differential equations for the coefficients in Eq. (2.120) and Eq. (2.120), they reduce to

$$\dot{a}_1 = -\langle \psi_{1a} | \dot{\psi}_{2a} \rangle e^{-i \int_{t_0}^t dt' E_{2a} - E_{1a}} a_2 \quad (2.132)$$

$$\dot{a}_2 = -\langle \psi_{2a} | \dot{\psi}_{1a} \rangle e^{i \int_{t_0}^t dt' E_{2a} - E_{1a}} a_1, \quad (2.133)$$

in the absence of the UV field, where we have kept the non-adiabatic terms. We will keep the non-adiabatic terms, since the multiphoton processes leading to the ladder will include higher orders of the NIR field. This will lead to faster oscillation, which takes us out of the region of the adiabatic approximation. From the initial condition of all population in the ground state, $a_1(t_0) = 1$ and $a_2(t_0) = 0$, we can simplify the equations for the coefficient by assuming that the NIR field is so weak and detuned that almost no population is moved from the ground state to the excited state. Thus giving us

$$\dot{a}_1 = 0 \quad (2.134)$$

$$\dot{a}_2 = \langle \psi_{2a} | \dot{\psi}_{1a} \rangle e^{i \int_{t_0}^t dt' E_{2a} - E_{1a}}, \quad (2.135)$$

where we see that the coefficient of the dressed ground state a_1 stays constant.

The dipole moment of the system becomes

$$\langle \hat{D} \rangle_{\text{ladder}} = \langle \psi_{1a} | \hat{D} | \psi_{1a} \rangle + 2\text{Re} \left[a_2 \langle \psi_{1a} | \hat{D} | \psi_{2a} \rangle e^{-i \int_{t_0}^t dt' E_{2a} - E_{1a}} \right]. \quad (2.136)$$

From the above analysis we can see that the first term is independent of the non-adiabatic terms and is still in the adiabatic model, while the second term is zero without the non-adiabatic term. Later numerical analysis show that both terms contribute to the features, but for simplicity, and

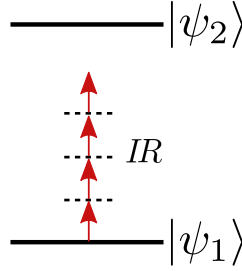


Figure 2.11: Sketch of the process leading to the ladder features, where the rungs are separated by one IR photon starting from the ground state. Note that from Eq. (2.138) it is clear that the presence of the excited state is needed for the features.

to get an analytical expression, we consider only the adiabatic first term, $\langle \psi_{1a} | \hat{D} | \psi_{1a} \rangle$.

Using the exact expression for the adiabatic states Eq. (2.68) and Eq. (2.69), we can expand the dipole moment to higher orders in the NIR (using e.g. the Maxima program [46]). Up to fourth order in the NIR field the dipole moment reads

$$\langle \psi_{1a} | \hat{D} | \psi_{1a} \rangle \approx D_{12} + D_{12}^2 \sum_{n=1}^4 (n+1) \frac{(D_{22} - D_{11})^{n-1}}{(E_2 - E_1)^n} F_{\text{IR}}^n. \quad (2.137)$$

The expansion above is only true approximately, since we have neglected some additional terms that arise from third order and above. However these extra terms, can for the parameters we consider in chap. 4 be neglected to give us a simpler expression.

Using this as the dipole moment we can take the Fourier transform (see appendix A) and calculate the response function. Again we neglect the constant term, since this will not contribute to delay dependent features. The resulting response function is

$$\begin{aligned} S(\omega, \tau) &= \frac{\pi \rho D_{12}^2 T_{\text{IR}} T_{\text{XUV}} F_{0,\text{XUV}}}{4c} \frac{\omega^2}{\omega_{\text{XUV}}} \exp\left(-\frac{T_{\text{XUV}}^2 (\omega - \omega_{\text{XUV}})^2}{16}\right) \\ &\times \sum_{n=2}^4 (-1)^n \frac{n+1}{2^n} \frac{(D_{22} - D_{11})^{n-1}}{(E_2 - E_1)^n} \frac{F_{0,\text{IR}}^n}{\sqrt{n}} \\ &\times \exp\left(-\frac{T_{\text{IR}}^2 (\omega - n\omega_{\text{IR}})^2}{16n}\right) \text{Im}\left[i^{n+1} e^{i\omega\tau} e^{i(n-1)\varphi}\right] \end{aligned} \quad (2.138)$$

From the approximate expression derived here, we can note some of the overall properties of the features. We see that each rung of the ladder depends on the energy difference $(E_2 - E_1)^{-n}$ of the two levels, such that closer lying levels corresponds to a stronger signal. The power of the difference grows with the level of the ladder, such that the effect is stronger as one move up the rungs. This in accordance with the mixing of the states being weaker as the energy difference increases. The rungs are also dependent on the difference of the two diagonal dipole moments $(D_{22} - D_{11})$, again with increasing powers. The last Gaussian indicates the position of the features at photon energies $\omega = n\omega_{\text{IR}}$. As sketch of the processes leading to the rungs of the ladder is shown in Fig. 2.11.

Numerical Methods

In this chapter we describe the numerical methods used to propagate the one-dimensional coupled nuclear equations as well as other methods used in the calculation and analysis of the spectra.

The main problem we want to tackle numerically is the one-dimensional time-dependent solution of a Schrödinger(like) equation

$$i\partial_t\Psi(x,t) = \hat{H}(t)\Psi(x,t), \quad (3.1)$$

where the Hamiltonian is dependent on time. In our specific case it is the one-dimensional effective radial Schrödinger equation of the nuclear wave function either in the adiabatic Eq. (2.35) or diabatic Eq. (2.51) representation, but it could in principle be any other equation of a similar form.

Many, if not all, of the methods described in this chapter can be generalized and used on higher dimensional problems, but to ease notation and description, and since we only consider one-dimensional problems, we stick to the notation of the one-dimensional case. The methods and algorithms are rather general and can be used on a wide set of problems. We therefore choose to use slightly different notation compared to the rest of the thesis. We will use x to describe the spatial axis instead of R and p to describe the conjugate momenta. Time is still t and the solution to the Schrödinger equation is denoted by Ψ .

3.1 Grid Representation

To implement a numerical solution of the Schrödinger equation of the system, one needs to choose how to represent the wave functions and the

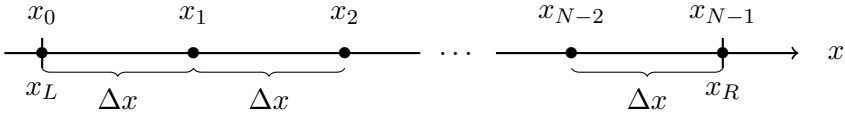


Figure 3.1: Equidistant spatial grid.

Hamiltonian. In our numerical approach we choose to represent the wave functions of the system on a grid, where the continuous functions are given in terms of a discrete set of amplitude at a set of grid points. We use a spatial grid of N points inside a finite box $[x_L, x_R]$,

$$x_n \in [x_L, x_R], \quad x_n = x_L + n\Delta x, \quad \Delta x = \frac{x_R - x_L}{N - 1}, \quad n = 0, 1, \dots, N - 1, \quad (3.2)$$

where we have chosen the grid to be equidistant with separation Δx , see figure 3.1 for a sketch. Similarly we define a corresponding momentum grid

$$p_k \in [p_L, p_R], \quad p_k = p_L + k\Delta p, \quad \Delta p = \frac{p_R - p_L}{N - 1}, \quad k = 0, 1, \dots, N - 1, \quad (3.3)$$

where the relation between the two grid spacings is given by

$$\Delta x \Delta p = \frac{2\pi}{N}. \quad (3.4)$$

The choice of this relation is related to the propagation scheme described in sec. 3.2.2. We further choose our momentum grid to be symmetric around 0,

$$-p_L = p_R = \frac{N - 1}{2} \Delta p, \quad (3.5)$$

such that we equally well describe wave packets moving to the left and the right.

3.1.1 Grid Hamiltonian for vibrational levels and eigenstates

To aid in the analysis it can be helpful to know the vibrational levels of the system. To obtain these we use a representation of the Hamiltonian, which becomes an $N \times N$ matrix on the spatial grid

$$\hat{H} = \hat{T} + \hat{V} \quad \rightarrow \quad H_{ij} = T_{ij} + V_{ij}, \quad (3.6)$$

that we can then diagonalize to calculate the vibrational energy levels and eigenstates.

On the spatial grid the potential energy is diagonal, since it is just given by its value at a given grid point

$$V_{ij} = V(x_j)\delta_{ij}. \quad (3.7)$$

The kinetic energy on the other hand is more complicated, with one of the simplest being a finite difference approach. In our case we use the Fourier Grid Hamiltonian method [47], where for even N the kinetic energy is

$$T_{ij} = \frac{\hbar^2}{2\mu} \begin{cases} \frac{\pi^2}{3(x_R - x_L)^2} (N^2 + 2), & \text{for } i = j \\ \frac{\pi^2}{(x_R - x_L)^2} \frac{(-1)^{j-i}}{\sin^2(\pi \frac{j-i}{N})}, & \text{for } i \neq j. \end{cases} \quad (3.8)$$

3.2 Time Evolution

The wave function $\Psi(x, t)$ of a quantum system given by the Hamiltonian $\hat{H}(t)$ can be evolved in time by use of the time evolution propagator, see e.g. ref. [31] for a textbook description. It is defined as the operator which evolves an arbitrary quantum state in time

$$\Psi(x, t) = \mathcal{U}(t, t_0)\Psi(x, t_0), \quad (3.9)$$

and can be shown to satisfy the time-dependent Schrödinger equation

$$i\partial_t \mathcal{U}(t, t_0) = \hat{H}(t)\mathcal{U}(t, t_0). \quad (3.10)$$

The time evolution operator must preserve norm and is therefore unitary

$$\mathcal{U}^\dagger(t, t_0)\mathcal{U}(t, t_0) = I, \quad (3.11)$$

and for a vanishing time step it reduces to the identity

$$\lim_{\epsilon \rightarrow 0} \mathcal{U}(t_0 + \epsilon, t_0) = I. \quad (3.12)$$

Physically evolution over a larger time step must equal evolution over smaller time steps adding to the same, meaning that the operator must fulfil the composition property

$$\mathcal{U}(t_2, t_0) = \mathcal{U}(t_2, t_1)\mathcal{U}(t_1, t_0). \quad (3.13)$$

In the general case where the dynamics of the system are given by a time-dependent Hamiltonian, that does not commute with itself at all times, the solution is a Dyson series. This infinite series is useful in e.g. the description of scattering theory, but not appropriate for a numerical solution. For small time steps Δt however, it is approximately given by the matrix exponential of the Hamiltonian at a given time

$$\mathcal{U}(t_0 + \Delta t, t_0) \approx e^{-i\hat{H}(t_0)\Delta t}, \quad (3.14)$$

For this approximation to be valid, the time step has to be chosen short enough, i.e. much shorter than the natural time scales of the system, such that the Hamiltonian can be considered constant over the interval. By subdividing an arbitrarily large interval into multiple small time-steps one can, using the composition property Eq. (3.13), obtain

$$\mathcal{U}(t_M, t_0) = \prod_{m=0}^{M-1} \mathcal{U}(t_{m+1}, t_m) \approx \prod_{m=0}^{M-1} e^{-i\hat{H}(t_m)\Delta t}, \quad (3.15)$$

which is what we will be using. We therefore only need to calculate the short-time operator to do time evolution over any time interval.

3.2.1 Split Operator Method

Calculating the matrix exponential is in general an expensive procedure unless the matrix is diagonal, and we therefore want an effective way to calculate the short-time operator.

The Split Operator method [26] is an approach, which can be used when the Hamiltonian can be divided into a term depending only on the momentum and a term depending only on the position

$$\hat{H}(\hat{x}, \hat{p}) = \hat{T}(\hat{p}) + \hat{V}(\hat{x}). \quad (3.16)$$

For the diatomic molecules this is the case in the diabatic representation or for the adiabatic representation when the vibronic coupling can be ignored. For the interaction with the field this also holds in the length gauge, but would not be applicable if we worked in the velocity gauge. The Split-Operator method has previously been used in the study of ATAS of diatomic molecules in ref. [19, 20].

In the Split Operator method the short-time operator is approximated as a product of a kinetic and a potential propagator

$$e^{-i\hat{H}(\hat{x}, \hat{p})\Delta t} \approx e^{-i\hat{T}(\hat{p})\Delta t} e^{-i\hat{V}(\hat{x})\Delta t}, \quad (3.17)$$

which is only true to first order in the small time step Δt , since the two terms of the Hamiltonian will not commute due to the canonical commutation relation $[\hat{x}, \hat{p}] = i\hbar$. The trick is then to take advantage of the fact that the term depending on the position $\hat{V}(\hat{x})$ is diagonal on the spatial grid, while the term depending on the momentum $\hat{T}(\hat{p})$ is diagonal on the momentum grid, such that the respective matrix exponentials are easy to calculate.

By using a symmetric splitting instead of the simpler one in Eq. (3.17)

$$e^{-i\hat{H}(\hat{x}, \hat{p})\Delta t} \approx e^{-i\hat{T}(\hat{p})\Delta t/2} e^{-i\hat{V}(\hat{x})\Delta t} e^{-i\hat{T}(\hat{p})\Delta t/2}, \quad (3.18)$$

we get an expression which is correct up to second order without much more computation, and this is the form we will be using. The small time interval Δt must therefore be chosen with two conditions in mind; such that the exponential expansion in Eq. (3.14) is valid and the expansion Eq. (3.18) can be used.

Transformation between the wave functions on the spatial grid and on the momentum grid is given by the Fourier transform. The time evolution over a short time step can therefore be calculated in the following way: propagate the momentum wave function by the first factor, which is diagonal, Fourier transform the momentum wave function to the spatial wave function and propagate with the next factor, which is now the diagonal one, Fourier transform back to the momentum wave function and finally propagate with the last factor.

Fig. 3.2 shows a flowchart of the Split Operator method using the Fast-Fourier transform described in the next section to calculate the Fourier transform. Due to the small time step needed for a converged time evolution the the calculated time-dependent dipole moment of the wave function is only written out every 10th step.

3.2.2 The Fast-Fourier Transform

In the Split Operator method we need to transform between the spatial and momentum wave functions. The transformation between the two is given by the Fourier transform and the inverse Fourier transform respectively

$$\Psi(x) = \frac{1}{\sqrt{2\pi}} \int_{\mathbb{R}} \Phi(p) e^{ipx} dp \quad (3.19)$$

$$\Phi(p) = \frac{1}{\sqrt{2\pi}} \int_{\mathbb{R}} \Psi(x) e^{-ipx} dx. \quad (3.20)$$

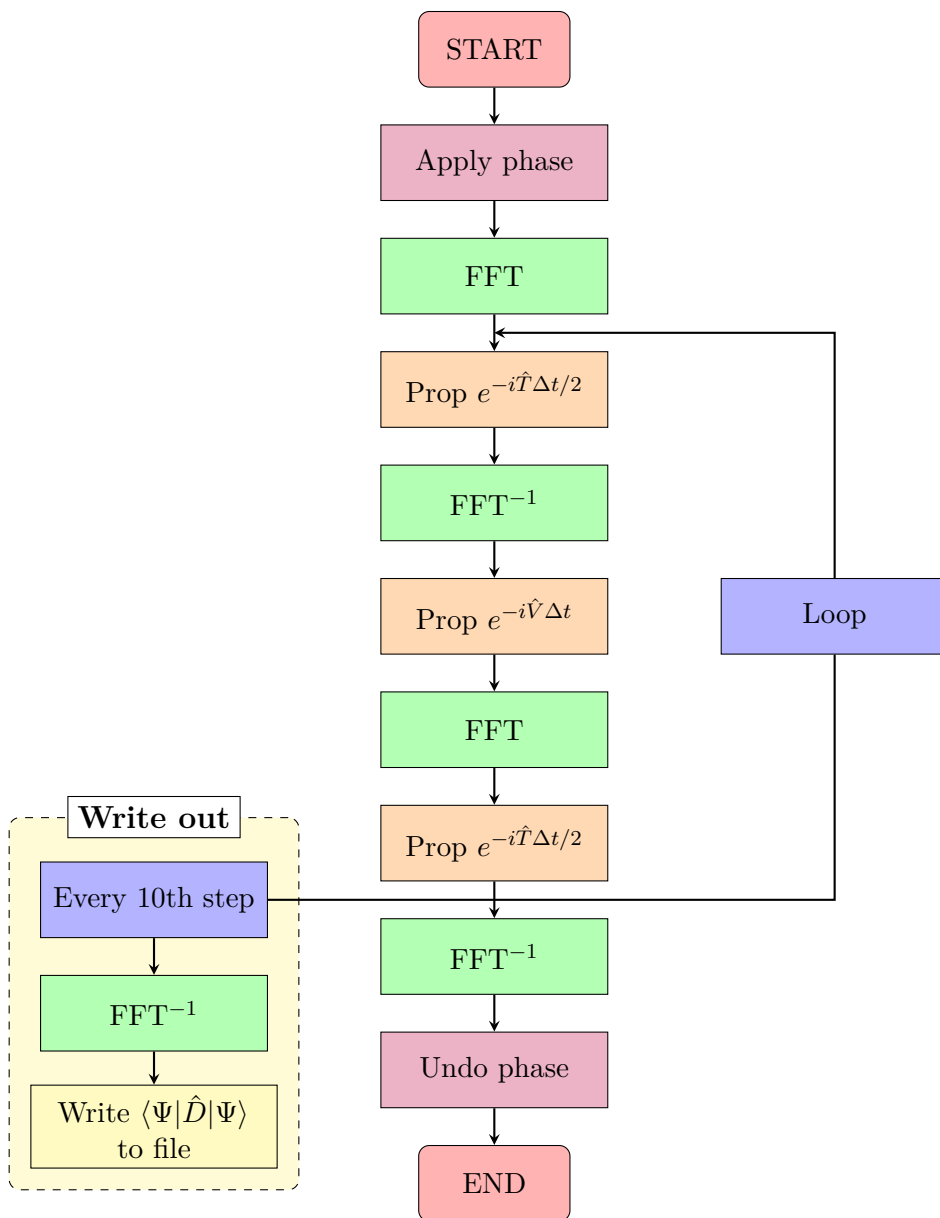


Figure 3.2: Flowchart for our time-propagation scheme using the Split Operator method together with the Fast-Fourier Transform (FFT), see main text. Every 10th step the spatial wave function is found and the time-dependent dipole moment of the system is calculated and written to file. The undoing of the phase at the end is not necessary, but is included for completion.

On the discrete equidistant grids Eq. (3.2) and Eq. (3.3) the integral transformations becomes

$$\Psi(x_n) = \frac{1}{\sqrt{2\pi}} \sum_{k=0}^{N-1} \Phi(p_k) e^{ip_k x_n} \Delta x \quad (3.21)$$

$$\Phi(p_k) = \frac{1}{\sqrt{2\pi}} \sum_{n=0}^{N-1} \Psi(x_n) e^{-ip_k x_n} \Delta p. \quad (3.22)$$

Transforming the wave function using this consists of N sums, i.e. one for each grid points, with N terms in each resulting in a scaling of N^2 . But by introducing the phase transformed quantities

$$f_n = \Psi(x_n) e^{-ip_L x_L} e^{-ip_L \Delta x n} \quad (3.23)$$

$$\tilde{f}_k = \Phi(p_k) e^{i\Delta p x_L k} \sqrt{\frac{\Delta p}{\Delta x}}, \quad (3.24)$$

and imposing the relation between the two grids Eq. (3.5) mentioned above, we can get the sums on the form of the discrete Fourier transform

$$f_n = \frac{1}{\sqrt{N}} \sum_{k=0}^{N-1} \tilde{f}_k e^{i2\pi kn/N} \quad (3.25)$$

$$\tilde{f}_k = \frac{1}{\sqrt{N}} \sum_{n=0}^{N-1} f_n e^{-i2\pi kn/N}, \quad (3.26)$$

where there exist the efficient Fast Fourier Transform (FFT) algorithm [48] which scales much more preferably as $N \log N$.

3.2.3 Imaginary Time Propagation

At the start of the simulation, we want the system to initially be in the ground state of the free field Hamiltonian \hat{H}_0 . We will therefore consider here, how the ground state of a time-independent Hamiltonian can be determined.

One way to obtain the ground state is to use the time evolution operator, but instead of propagating forward in real time, one uses the substitution $t = -i\tau$ with $\tau \in \mathbb{R}$ and propagates in imaginary time

$$\mathcal{U}(-i\tau, 0) = e^{-\hat{H}_0 \tau}. \quad (3.27)$$

To see how this works, we consider first an arbitrary initial guess for the wave function and expands this

$$\Psi(x, t) = \sum_n c_n(t) \psi_n(x) \quad (3.28)$$

in the eigenstates of the Hamiltonian

$$\hat{H}_0 \psi_n(x) = E_n \psi_n(x). \quad (3.29)$$

The imaginary time evolution operator works on this state

$$\mathcal{U}(-i\tau, 0) \Psi(x, 0) = \sum_n c_n(0) e^{-\hat{H}_0 \tau} \psi_n(x) = \sum_n c_n(0) e^{-E_n \tau} \psi_n(x), \quad (3.30)$$

by multiplying each of the eigenstates by an decreasing exponential. The ground state is, by definition, the state with the lowest energy and by letting τ be larger enough, i.e. by propagating for a sufficiently long time, and renormalizing along the way, the wave function will end up in the ground state as long as there was a non-zero initial population i.e. $c_0 \neq 0$.

3.3 Complex Absorbing Potential

Since we are doing the simulation in a box of finite size, we must consider behaviour that can arise due to the presence of a boundary. For the molecular system there is a real physical boundary at zero separation, and this will in general not be a problem, since the potential is highly repulsive when the two nuclei are close, but we impose an unphysical cutoff for large separation. Running the simulation without taking special care at this boundary could resolve in unwanted behaviour for a wave packet approaching. This could e.g. resolve in unphysical reflection and therefore a return of the wave packet, which could in principle give a significant discrepancy in the dynamics. One way to solve this problem, is to assume that the box is large enough, such that a wave packet moving far enough out will never, at least to a good approximation, return again, and we can therefore remove that part of the wave function.

This can be done in practice by introducing a so-called complex absorbing potential (CAP)

$$V(x) \rightarrow V(x) - iV_{\text{CAP}}(x). \quad (3.31)$$

This is a term added to the potential energy which is purely (negative) imaginary, and only non-zero near the boundary where we wish the wave

packet to be removed. When one takes the matrix exponential of the potential energy in the propagation scheme, this term will give an exponential dampening at the boundary which effectively removes the outgoing wave packet.

In our case we use a potential of the form

$$V_{\text{CAP}}(x) = \begin{cases} \eta(x - x_{\text{CAP}})^p, & \text{for } x > x_{\text{CAP}} \\ 0, & \text{otherwise,} \end{cases} \quad (3.32)$$

where the amplitude η , the start of the CAP x_{CAP} and the power p can be chosen to fit the system at hand.

3.4 The Window Function

In a real experimental set-up, the time dependent dipole moment of the system will dephase because of collisions between the molecules in the gas, spontaneous decay and due to finite detector resolution [45]. These effects are not taken into account in our model thus far, but can be included by the use of a window function

$$\langle D \rangle(t, \tau) \rightarrow W(t - t_w) \langle D \rangle(t, \tau), \quad (3.33)$$

which dampens the time dependent dipole moment over a given time scale.

In our work we use the following form for the window function

$$W(t - t_w) = \begin{cases} 1, & t < t_w \\ \exp\left[-\frac{(t - t_w)^2}{T_w^2/4}\right], & t \geq t_w, \end{cases} \quad (3.34)$$

which has been used in the previous descriptions of ATAS [11]. Other window functions used in studies of ATAS are often based on trigonometric functions [4, 19].

The start of the Window function t_w is set at the incident of the XUV, since this is what starts the non-trivial dynamics, and the width T_w is chosen by hand such that the qualitative features of interest are not altered, but the broadening of the features resembles that of an experiment. The FWHM of the Gaussian is given in terms of T_w by the relation $T_{\text{FWHM}} = \sqrt{\log 2} T_w$.

In figure 3.3 we have plotted the time-dependent dipole moment of the model system considered in Chap. 5 with a single XUV pulse incident

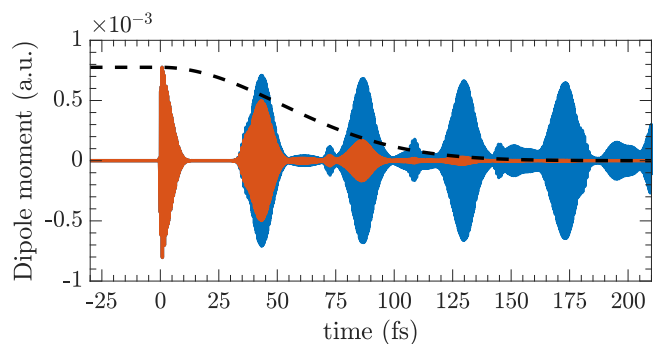


Figure 3.3: Time-dependent dipole moment for XUV only spectroscopy of model system. Blue curve shows the raw dipole moment, dashed line shows the window function (scaled) and the red curve shows their product. The parameters for the window function used is $t_w = 0$ fs, $T_w = 145$ fs and $T_{\text{FWHM}} = 121$ fs.

at time 0 fs. The blue curve shows the calculated dipole moment from the simulation, the dashed black curve shows the chosen window function scaled to the signal and the red curve shows the resulting product.

The LiF molecule, a polar diatomic molecule

In this chapter we present the ATAS spectra of the LiF molecule. Being a polar molecule, LiF exhibits a nonzero permanent dipole and it is the effect of this on the spectra that is the main point of the work. The majority of the previous studies, both in theory and experiments, on ATAS of molecules have been on nonpolar homonuclear systems such as H₂ [16, 19, 20], N₂ [15, 17, 21] and O₂ [18], with the exception of the work considering CO in [49].

We first present the properties of the LiF system; the potential energy curves and their dipole couplings. And provide the parameters of the incoming NIR and UV fields. In the subsequent section we provide a full numerical simulation of the system using the split operator method described in sec. 3.2.1 to propagate the N -surface model, together with a description of the features of the calculated spectra. Further analysis of the features are done with the aid of the two-level model given in sec. 2.6 used within a fixed nuclei approximation.

The context of this chapter is based on the work in ref. [1].

4.1 The LiF system and field parameters

An illustration of the LiF molecule together with the incoming NIR field is shown in Fig. 4.1. The internuclear axis is oriented along the z -axis parallel with the polarization of the linearly polarized NIR and UV pulses.

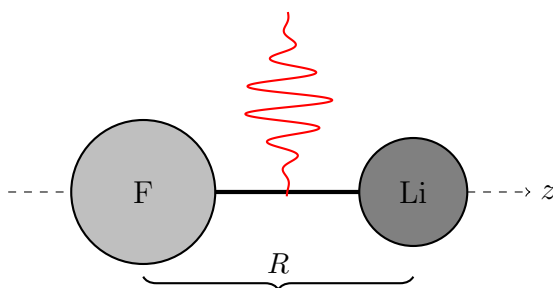


Figure 4.1: Illustration of the LiF molecule and incoming NIR field. The molecule is oriented in the z direction, which is parallel to the polarization of the UV and the NIR field. R is the internuclear distance. Reproduced with permissions from Phys. Rev. A **98**, 053401 (2018) [1]. Copyright 2018 American Physical Society.

In our study of the LiF molecule we restrict ourselves to the two lowest state of the fully symmetric representation, i.e. the ground state curve and the first excited curve belonging to the same symmetry. The adiabatic potential energy curves as well as the dipole moment functions were provided by Brett Esry and Greg Armstrong interpolated from data given in ref. [43]. The two energy curves $E_1(R)$ and $E_2(R)$ are shown in the bottom panel of Fig. 4.2 with the center of the ground state curve at $R_0 = 3$ (a.u.) indicated by a vertical dotted line. The slope of the excited curve at R_0 is negative, leading to the wave packet excited from the ground state curve by the UV pulse to propagate out towards larger R as illustrated in Fig 2.2 (a), this will lead to a cut-off of the dipole moment between the excited and ground state at a timescale shorter than the usual dephasing time, resulting in a broadening of the corresponding absorption features. In the shaded region of Fig. 4.2 the two curves exhibit an avoided crossing. Around this point it is usually necessary to include the vibrational coupling as their effect can be significant. However due to the shape of the curve, a wave-packet moving far enough out to interact significantly with the crossing will not return to the Frank-Condon window of the ground state, and will therefore have no impact on the spectrum. The avoided crossing can therefore be ignored in this system, and we continue to work in the adiabatic representation.

The dipole moments $D_{11}(R)$, $D_{12}(R)$ and $D_{22}(R)$ as functions of the internuclear distance are shown in the upper panel of Fig. 4.2. LiF, being a polar molecule, breaks parity symmetry such that the electronic states are no longer of a definite parity. Dipole transitions between states belonging

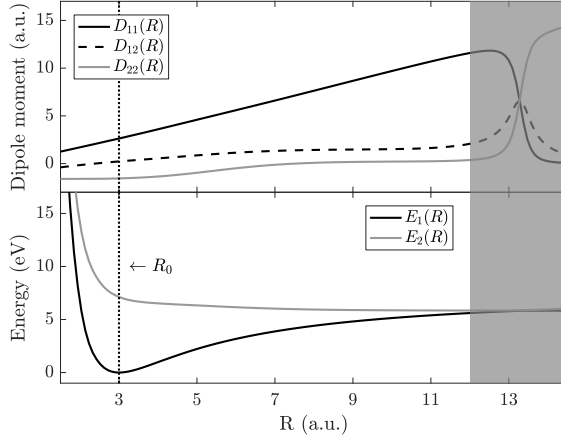


Figure 4.2: Dipole moments (top panel) and potential energy surfaces (bottom panel) of LiF, as functions of the internuclear distance R . Dotted line indicates center of ground state nuclear wave function at $R_0 = 3$, where $E_1(R_0) = 0$ eV, $E_2(R_0) = 7.07$ eV, $D_{11}(R_0) = 2.62$, $D_{12}(R_0) = 0.22$ and $D_{22}(R_0) = -1.55$. Curves are interpolated from data in ref. [43]. The shaded region shows the avoided crossing between the two curves. This part of the plot was not included in ref. [1], as the crossing has no influence on the spectra. Adapted with permissions from Phys. Rev. A **98**, 053401 (2018) [1]. Copyright 2018 American Physical Society.

to the same symmetry are no longer forbidden, meaning that transitions between the two curves considered, and more importantly, couplings of states on the same curve are allowed. We therefore have both a non zero dipole moment between the states $D_{12} \neq 0$, but also a dipole moment D_{11} , D_{22} of each of the electronic states.

Compared with earlier studies where homonuclear molecules were considered, the energy distance between the ground and excited state is relatively small. As the short pulse is usually chosen such that transitions occur through single photon excitations, we use here an UV pulse instead of an XUV. Both the short UV and the longer NIR pulse are defined by the vector potential given in Eq. (2.17), and their respected parameters are listed in table 4.1. Both fields are linearly polarized in the z-direction, i.e. along the axis of the molecule as indicated for the NIR pulse in Fig. 4.1.

Table 4.1: Field parameters of the NIR and UV pulses both defined by the vector potential Eq. (2.17). The CEP of both fields are 0, except for Fig. 4.6 where we consider orientation and alignment.

	NIR-pulse	UV-pulse
Central Wavelength λ [nm]	800	160
Central frequency ω [eV]	1.55	7.75
Intensity I [W/cm ²]	10^{12}	5×10^7
Duration T [fs]	40.01	1.07
Cycles N_c	15	2

4.2 Full numerical simulation

We start the analysis of the system by a full numerical simulation of the nuclear dynamics on the two adiabatic curves using the N -surface model. The nuclear wave packets are propagated using the Split Operator method, see sec. 3.2.1, with a time step of $\Delta t = 0.05$ a.u. = 1.2 as, a box size of $R_{\max} = 25$ a.u. and grid size $\Delta R = R_{\max}/N_R$ with the number of grid points $N_R = 1024$. A complex absorption potential, see Sec. 3.3, is used to remove the outgoing part of the wave packet at the boundary of the box. Prior to the simulation the ground state is found by imaginary time propagation with zero fields. From the obtained nuclear wave functions the time-dependent dipole moments can be calculated through numerical integration.

The dipole moment is multiplied by the Window function Eq. (3.34) with $T_w = 100$ fs before the Fourier transform, and the spectra is then calculated using Eq. (2.5). Due to the small energy difference between the two curves, it is possible for both the UV and the NIR to induce the dynamics, and the start of the window function is chosen to be at the center of the last of the two pulses.

In Fig. 4.3 we see the spectrum from the full numerical simulation in panel (a). At $E_2(R_0) - E_1(R_0) = 7.07$ eV we see the main absorption line, coming from a vertical Franck-Condon transition of the ground state centered at R_0 on the ground state curve E_1 up to the excited state curve E_2 , see Fig. 4.2. The absorption line is quite broad, due to the excited state energy curve being dissociative at the given energy leading to the nuclear wave packet moving away from the Franck-Condon window of the ground state. We further see a modulation of the main line roughly at delays $-40 \text{ fs} < \tau < 40 \text{ fs}$. This can be attributed to which-way interference [45],

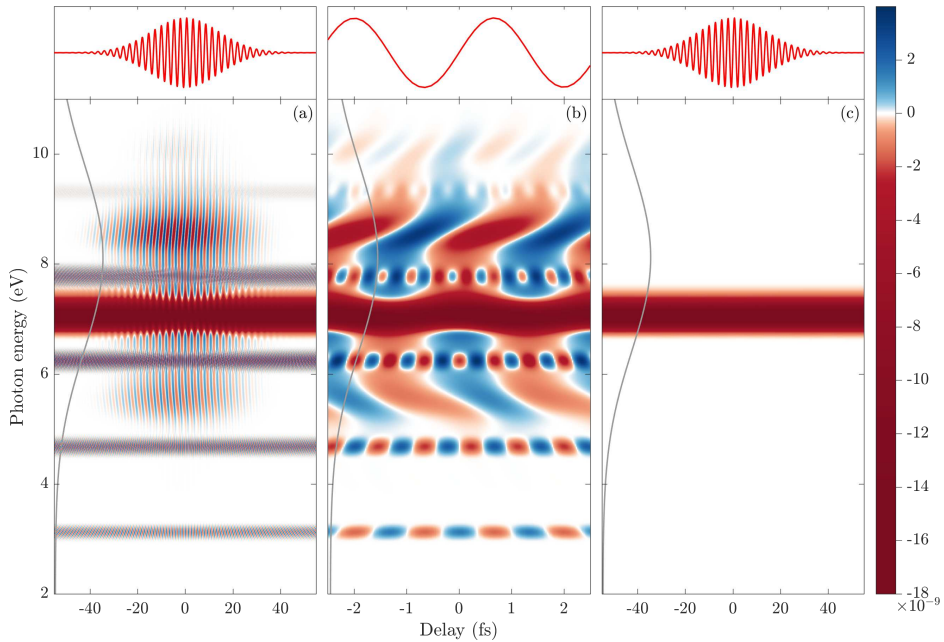


Figure 4.3: Attosecond transient absorption spectrum of the LiF molecule as calculated by Eq. (2.5), exhibiting the difference between systems with a permanent dipole moment (e.g., polar molecules) in panels (a) and (b), and systems with no permanent dipole moment (e.g. nonpolar molecules) in panel (c). The main features visible in panel (a) include the main absorption line at $E_2(R_0) = 7.07$ eV; light-induced structures centered at energies $E_2(R_0) \pm \omega_{\text{IR}}$ and $E_2(R_0) + 2\omega_{\text{IR}}$, i.e., at 5.51 eV, 8.61 eV and 10.16 eV; and the rungs of the ladder structure at $E_1(R_0) = n\omega_{\text{IR}}$, i.e. at n times 1.55 eV, with $n = \{2, 3, 4, 5, 6\}$. Panel (b) exhibits a zoomed in version of panel (a), which yields a clearer view of the characteristics of the ladder structure. In panel (c) the main absorption line is the only feature remaining. The frequency bandwidth of the UV pulse is shown in gray in each figure. The top panels depict the NIR pulse centered at $\tau = 0$ fs. The color scale on the right displays the signal strength in arbitrary units. The pulse parameters are given in table 4.1. Reproduced with permissions from Phys. Rev. A **98**, 053401 (2018) [1]. Copyright 2018 American Physical Society.

where multiple pathways leads to the same final destination. The different pathways are absorption of one UV photon and absorption or emission of one or more NIR photons.

We further see LIS features one NIR energy away from the main line, $E_2(R_0) \pm \omega_{\text{IR}}$, i.e. at 5.51 eV and 8.61 eV, and an additional 2 NIR above, at $E_2(R_0) + 2\omega_{\text{IR}} = 10.16$ eV. We do not see a feature at $E_2(R_0) - 2\omega_{\text{IR}}$, but this is most likely due to this energy not lying within the bandwidth of the UV.

Finally we observe a ladder like feature situated at multiples of the NIR energy away from the ground state $E_1(R_0) + n\omega_{\text{IR}}$, with the rungs of the ladder visible in the figure corresponding to $n = 2, 3, \dots, 6$. This is a new structure not previously seen and is due to the presence of the permanent dipole. In panel (b) we see a zoomed in view of the full numerical solution to get a clearer picture of the features. For the LIS we see that the modulation of the features as a function of the delay oscillates roughly with the period of the NIR pulse for the two features at $E_2(R_0) \pm \omega_{\text{IR}}$ and at twice the period of the NIR for the feature at $E_2(R_0) + 2\omega_{\text{IR}}$. For the ladder we see that the period decreases with photon energy and with a phase difference of the modulation of $\Delta\varphi = \pi/2$ between adjacent rungs.

We note that the spectrum lacks the hyperbolic sidebands as well as the oscillating fringes. As described earlier the dissociative shape of the excited state leads to the excited wave-packet quickly moving away from the Frank-Condon window of the ground state. Any features stemming from processes where the NIR arrives some time after the UV or which requires a dipole between the ground and excited state to endure for a longer period of time will therefore not be present, explaining the absence of the sidebands and fringes which typically extend over a wide range of negative delays.

In panel (c) we shown the spectrum of the system with no permanent dipole, i.e. $D_{11} = D_{22} = 0$. In this case the only feature that remain is the main absorption line. Without the permanent dipole, the excited state curve behaves as a bright state and without the presence of an additional dark state the three-level model (see sec. 2.5.1) predicts no LIS, fringes or sidebands.

4.3 Light-induced structures

In systems without a permanent dipole, both atoms and molecules, the LIS features are centered one NIR photon energy away from the dark state

and indicates a process with absorption if an UV photon together with the absorption or emission of an NIR photon. Transitions to the dark states are dipole forbidden and there will therefore be no visible signal of this state in the spectrum. In the three-level model described in sec. 2.5.1, we saw that both the dark and bright states are needed for the LIS. In the case of the LiF system, where there is a non-zero permanent dipole, both single UV photon transitions directly from the ground state to the excited states as well as transitions with a single UV plus a multiple of NIR photons are dipole allowed. We are thus able to see both the main absorption line as well as features off on or two NIR photons away from the line in the ATAS spectrum.

To aid in the analysis and description of the features of the spectra we will consider a simplified model, in which we consider fixed nuclei. In this case where we neglect the nuclear kinetic energy term, the system is reduced to the two levels given by the energies $E_1(R_0)$ and $E_2(R_0)$ coupled by the dipole moments $D_{11}(R_0)$, $D_{12}(R_0)$ and $D_{22}(R_0)$ and we employ the two-level adiabatic model of sec. 2.6. In the fixed nuclei case the excited state can no longer propagate away from the region overlapping with the ground state around R_0 , and the effect of this cut-off due to the dipole coupling between the two states have on the spectra must be included in another way. This is done by multiplying the excited state by another Window function Eq. (3.34), such that the population at R_0 is damped. The time of the Window function used is $T_{w,N} = 3.6$ fs and is related to the time it would take the excited wave packet to move out of the Frank-Condon window with the ground state.

In the case of the three-level model sec. 2.5.1, where one considers a ground state together with a bright and dark excited state, it was possible to obtain full analytical expression consistently to second order in the NIR field. In this model the LIS could be attributed to the interaction of the ground state with the dressed dark state. In the case of two levels with a permanent dipole as described in sec. 2.6, there is no dark or bright state, but similarly we consider the term describing the overlap of the ground state with the excited state (see Eq. (2.125)), where both states are now dressed by the NIR field. Due to the additional term coming from the diagonal dipole coupling, we consider a more simplified model where the NIR field only enters through its effect on the phase of the two dressed states. Fig. 4.4 shows a comparison of the full numerical solution of the N -surface model in panel (a) compared with the spectrum calculated numerically from the adiabatic two-level model in panel (b) using the time dependent dipole moment of Eq. (2.130), with phases given to

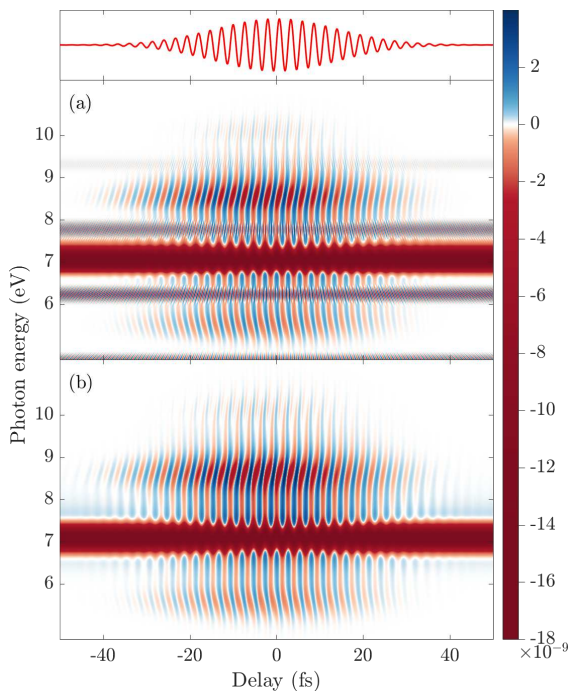


Figure 4.4: Attosecond transient absorption spectrum of the LiF molecule as calculated by Eq. (2.5), exhibiting the LISs. In panel (a) the LISs from the full numerical method of sec. 4.2 are shown. Panel (b) displays the LISs corresponding to the time dependent dipole moment of Eq. (2.130), with phases from Eq. (2.131). The top panel depicts the NIR pulse centered at $\tau = 0$ fs. The color scale on the right displays the signal strength in arbitrary units. The pulse parameters are given in table 4.1. Reproduced with permissions from Phys. Rev. A **98**, 053401 (2018) [1]. Copyright 2018 American Physical Society.

second order in the NIR field Eq. (2.131). The adiabatic model captures the main absorption line with the which-way interference together with the LIS features to good degree. From the two equations used in the adiabatic model, we see that the signal is dependent on both the diagonal, D_{11} and D_{22} , and the off-diagonal dipole matrix element D_{12} . The presence of a non-zero coupling between the levels D_{12} is needed for any of the features to be present at all, and dependence on the difference $D_{22} - D_{11}$ is consistent with the absence of the LIS in the case where the permanent dipole was removed in Fig. 4.3 (c). In the model here the position of the features comes from the expansion of the adiabatic energies Eq. (2.131), while in the three-level model it comes from the dipole moment of the dressed state with the ground state Eq. (2.86). It therefore seems that the origin of the LIS are not as simple for more complicated systems, and in general one needs to take into account the specific properties of the system.

4.4 Ladder feature

In the spectra calculated from the full numerical simulation in Fig. 4.3 we saw an additional feature resembling a ladder, which have not been observed in previous studies. In the section above we used the adiabatic two level model on the fixed nuclei energies to describe the LIS, and we will use the same model to analysis the ladder.

The rungs of the ladder are situated a multiple of NIR energies away from the ground state $E_1(R_0) + n\omega_{\text{IR}}$, suggesting that no absorption of a UV photon is needed. In Fig. 4.5 (a) we show the spectra of the full adiabatic model where the UV field is only directly in the calculation of the response function Eq. (2.5), but not in the amplitudes of the dressed states Eq. (2.132) and Eq. (2.133). In an experiment this would correspond to the UV pulse not interacting with the system, but only interfering afterwards with the generated light. Comparing the resulting spectra with Fig. 4.3 (b), we see that the adiabatic model reproduce a ladder almost indistinguishable with the full numerical simulation and conclude that the ladder is indeed an effect only dependent on the NIR field. The feature does however still depend on the delay between the two pulses, as the generated light still interact with the UV field.

The dipole moment in the two level model Eq. (2.136) consist of a term coming from the dressed ground state interacting with itself and a term coming from the interaction between the two dressed states. As the UV field is not included in the interaction with the system, the two

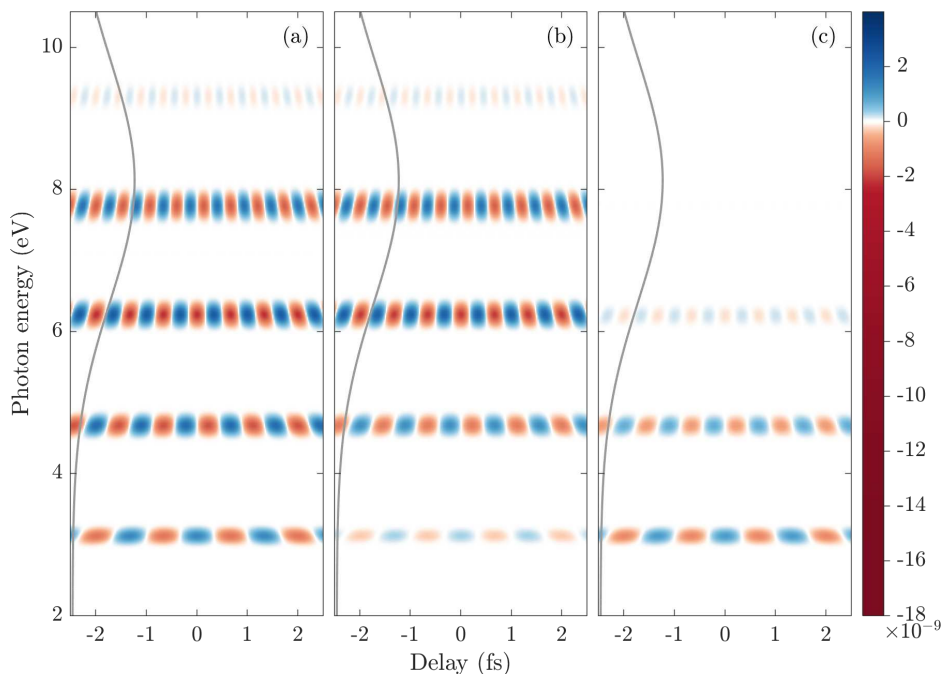


Figure 4.5: Attosecond transient absorption spectrum of the LiF molecule as calculated by Eq. (2.5), exhibiting an isolated view of the ladder feature. In panel (a) the ladder as calculated by the full adiabatic method of Eq. (2.132) and Eq. (2.133) with the dipole Eq. (2.124) is shown. In panel (b) the nonadiabatic component of the ladder, corresponding to the second term of Eq. (2.124) is displayed. In panel (c) the adiabatic component of the ladder is shown, corresponding to the first term of Eq. (2.124), which is indistinguishable from the spectrum derived from the analytical expression of Eq. (2.138) (Eq. (4.1)). The frequency bandwidth of the UV pulse is shown in gray in each figure. The color scale on the right displays the signal strength in arbitrary units. The pulse parameters are given in table 4.1. Reproduced with permissions from Phys. Rev. A **98**, 053401 (2018) [1]. Copyright 2018 American Physical Society.

dressed states are not coupled if the non-adiabatic coupling are neglected. The first term in the dipole can therefore be described as the adiabatic term and the second as the non-adiabatic term. In Fig. 4.5 we show the contribution of the non-adiabatic term in (b) and the adiabatic term in (c). From the two spectra it is clear that both terms contribute to the ladder, with the non-adiabatic term seeming to be the most important. The breakdown of the adiabatic approximation is expected, as the position of the rungs at higher multiples of the NIR energy suggest the underlying processes to be of higher order of the NIR field.

Getting an analytical expression for the response function of the full dipole would be to complicate and would not give a clear understanding of the contribution of the different parts. We instead focus on the adiabatic term, which is the simplest of the two. We repeat here the response function found in Eq. (2.138) (where $\varphi = 0$)

$$\begin{aligned}
 S(\omega, \tau) &= \frac{\pi\rho D_{12}^2 T_{\text{IR}} T_{\text{XUV}} F_{0,\text{XUV}}}{4c} \frac{\omega^2}{\omega_{\text{XUV}}} \exp\left(-\frac{T_{\text{XUV}}^2 (\omega - \omega_{\text{XUV}})^2}{16}\right) \\
 &\times \sum_{n=2}^4 (-1)^n \frac{n+1}{2^n} \frac{(D_{22} - D_{11})^{n-1}}{(E_2 - E_1)^n} \frac{F_{0,\text{IR}}^n}{\sqrt{n}} \\
 &\times \exp\left(-\frac{T_{\text{IR}}^2 (\omega - n\omega_{\text{IR}})^2}{16n}\right) \text{Im}\left[i^{n+1} e^{i\omega\tau}\right]. \tag{4.1}
 \end{aligned}$$

The form of this expression has already been discussed in sec. 2.6.2. The spectrum calculated from this analytical expression is indistinguishable from the numerical adiabatic component in Fig. 4.5.

The last factor containing the dependence on the time delay can be written, using that $i = e^{i\pi/2}$,

$$\text{Im}\left[i^{n+1} e^{i\omega\tau}\right] = \sin\left[\omega\tau + (n+1)\pi/2\right]. \tag{4.2}$$

As the rungs of the ladder are situated at multiples of the NIR, the oscillations becomes

$$\text{Im}\left[i^{n+1} e^{i\omega\tau}\right] = \sin\left[(n\omega_{\text{IR}} + \delta)\tau + (n+1)\pi/2\right] \quad \text{for } \omega = n\omega_{\text{IR}} + \delta. \tag{4.3}$$

We see here explicitly how the frequencies of the different rungs are $n\omega_{\text{IR}}$ and between each rung the phase changes with $\Delta\varphi = \pi/2$, which fits with what we observe in the full spectrum of Fig. 4.3.

4.5 Polar versus nonpolar molecules

The LIS and the ladder structure in the ATA spectra are both dependent on the difference of the diagonal dipole moments $D_{22} - D_{11}$, as can be seen from the adiabatic two-level model in Eq. (2.131) and Eq. (2.138). Heteronuclear nonpolar molecules such as HD^+ and HD can have a non-zero permanent dipoles D_{11} and D_{22} due to the mass asymmetry (see. Eq. (2.20) and Eq. (2.21)), but as they are symmetric with respect to parity they must fulfil $D_{22} = D_{11}$. It is therefore not sufficient for the molecule to be heteronuclear to see the new features, as being polar is necessary.

4.6 Orientation and alignment

In all calculation up to this point we have assumed a fixed orientation of all molecules in the sample as illustrated in Fig. 4.1. In a real experimental setup orientation of the molecules are possible [50–53], but alignment [54], where the molecules are in a mix of the two orientations, are simpler to realize. We will therefore compare the spectra obtained from an oriented sample with that of one that is only aligned. Alignment effects in ATAS have previously been considered in theory [21, 49].

Instead of interchanging the positions of the two nuclei, the same effect can be achieved by using a CEP of the two incoming fields of $\varphi = \pi$ instead of $\varphi = 0$. Since we work in the single system response approximation, and assume an even mixture of the two orientations, the response function for the aligned system is just the equal weighted average of the two opposite phases

$$S_{\text{aligned}}(\omega, \tau) = \frac{1}{2} [S(\omega, \tau; \varphi = 0) + S(\omega, \tau; \varphi = \pi)]. \quad (4.4)$$

Fig. 4.6 shows the comparison between the spectrum calculated from the oriented and the aligned systems. Both spectra are calculated using the full numerical model. We observe three major differences between the two signals. First, the LIS are significantly suppressed for the aligned molecules, second, the interference pattern on the absorption line has disappeared and third, the rungs of the ladder at even multiples of the NIR photon energy disappear. The different processes leading to these terms must still be present, as we are working in the approximation of single system response, but the generated signal must acquire opposite, or near opposite, phases resulting in destructive interference. This can be seen directly for the ladder if we consider the analytical expression for the non-adiabatic part of the response function, assuming that the adiabatic part follows the

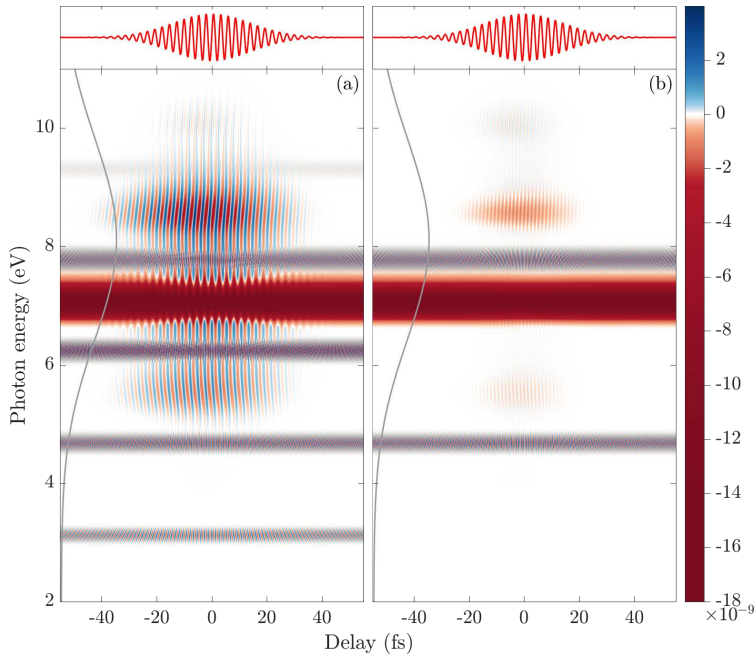


Figure 4.6: Attosecond transient absorption spectrum of the LiF molecule as calculated by Eq. (2.5), exhibiting the difference between oriented [panel (a)] and aligned [panel (b)] targets. Both spectra were calculated using the full numerical method of sec. 4.2. In panel (a) where the carrier-envelope phase φ of the fields is set to zero, corresponding to a target where all molecules are oriented relative to the field according to Fig. 4.1. Panel (b) corresponds to Eq. (4.4), i.e. with a target where molecules are aligned with respect to the field. The frequency bandwidth of the UV pulse is shown in gray in both figures. The top panel depict the NIR pulse centered at $\tau = 0$ fs. The color scale on the right displays the signal strength in arbitrary units. The pulse parameters are given in table 4.1. Reproduced with permissions from Phys. Rev. A **98**, 053401 (2018) [1]. Copyright 2018 American Physical Society.

same behaviour. The only difference between the two terms in Eq. (4.4) if we consider the analytical expression Eq. (4.1), is the last factor. Writing this last part out we find

$$\operatorname{Im}\left[i^{n+1}e^{i\omega\tau}\right] + \operatorname{Im}\left[i^{n+1}e^{i\omega\tau}e^{i(n-1)\pi}\right] = \begin{cases} 2\operatorname{Im}\left[i^{n+1}e^{i\omega\tau}\right], & n \text{ odd} \\ 0, & n \text{ even,} \end{cases} \quad (4.5)$$

and we therefore see that only the even rungs of the ladder will remain, since the odd ones will indeed interfere destructively.

Model System

In this chapter we examine the effect of an avoided crossing on the ATA spectra of a heteronuclear diatomic molecule. We consider a one-dimensional model system defined by a set of four diabatic potential energy curves, where the strength of the vibrational coupling, and thereby the avoided crossing, can be controlled. A similar one-dimensional model has been used to monitor non-adiabatic effects in the context of attosecond streaking [55], and in two-dimensional systems, where the non-adiabatic couplings are exemplified by conical intersections, model curves have been used to examine nuclear dynamics [56] as well as ATAS [25].

5.1 Parameters of the system and the fields

As a simple model for a homonuclear diatomic molecule we consider a set of four diabatic potential energy curves (see fig. 5.1), with a vibronic coupling between two of the excited states given by the off-diagonal diabatic coupling.

The ground state curve $V_0^{(d)}$ is chosen as a Morse potential [29], which is a commonly used empirical approximation to describe the ground state potential of diatomic molecules. For the excited diabatic curves $V_1^{(d)}$, $V_2^{(d)}$ and $V_3^{(d)}$ we use parabolas. We choose the parameters of the model such that the system resembles the N_2 molecule. The Morse potential is almost identical to the ground state found by an MCSCF calculation, and the position of the excited states relative to the ground state lies in the range of states probed in attosecond experiments [15, 17, 57]. The vibrational frequencies $\omega_1 = 0.0035$ a.u. and $\omega_2 = 1.2\omega_1$ of the two lowest excited

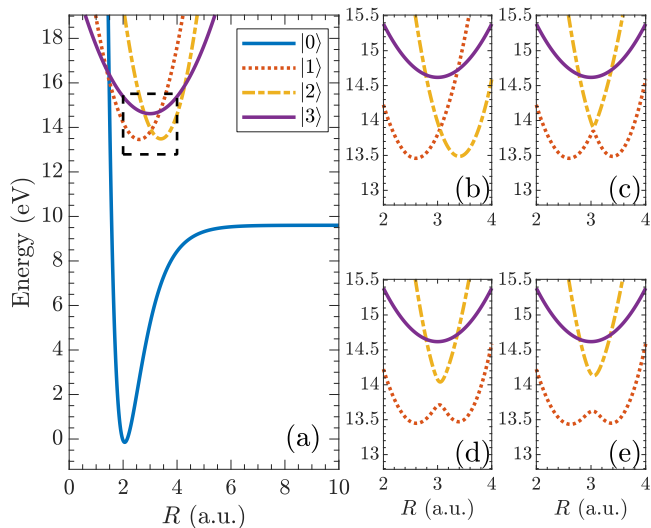


Figure 5.1: Potential energy curves of the model system. (a) ground state curve together with the three diagonal excited state curves in the diabatic representation. (b) Zoomed in view of the excited diagonal diabatic curves. (c) Zoomed in view of the adiabatic curves in the weak regime. (d) Zoomed in view of the adiabatic curves in the intermediate regime. (e) Zoomed in view of the adiabatic curves in the strong regime.

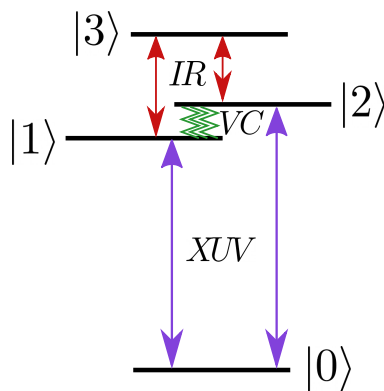


Figure 5.2: Level scheme of the model system. The ground state curve couples to the two lowest excited states through the XUV and these to further couple to the highest excited state through the IR. The two lowest excited curves are further coupled through a vibronic coupling (VC).

states $V_1^{(d)}$ and $V_2^{(d)}$ are roughly in the range of the excited states of N_2 from an MCSCF calculation. The frequency $\omega_3 = 0.6\omega_1$ of the highest excited state $V_3^{(d)}$ is further chosen, such that it extends over both of the two lower excited curves.

We assume dipole allowed transitions between the ground state and the two lowest excited states, as well as transitions between these and the two the highest lying state. This would correspond to the ground and highest excited state belonging to one symmetry and the two other excited states belonging to another. For the diabatic dipole moments we simply assume a constant with $D_{01}^{(d)} = D_{13}^{(d)} = 1$ a.u. and $D_{02}^{(d)} = D_{23}^{(d)} = 0.5$ a.u., where the values are comparable in magnitude to those found in a MCSCF calculation of N_2 . Lastly we introduce an off-diagonal diabatic coupling between the two lowest excited states. For the diabatic coupling $V_{12}^{(d)}$ we choose a Gaussian centered at the crossing R_c of the two diabatic curves

$$V_{12}^{(d)}(R) = Ae^{-(R-R_c)^2}, \quad (5.1)$$

which was previously used in a similar model in ref. [55]. As was discussed in relation to Eq. (2.62), we note that the strength of the diabatic coupling is inversely proportional to the vibronic coupling, i.e. that a weak diabatic coupling results and a strong vibronic coupling and vice versa. Fig. 5.2 shows a schematic of the couplings between the four states.

For a fixed amplitude of the diabatic coupling the corresponding adiabatic curves can be found by diagonalization of the diabatic potential matrix

$$\mathbf{V}^{(d)} = \begin{bmatrix} V_0^{(d)} & 0 & 0 & 0 \\ 0 & V_1^{(d)} & V_{12}^{(d)} & 0 \\ 0 & V_{12}^{(d)} & V_2^{(d)} & 0 \\ 0 & 0 & 0 & V_3^{(d)} \end{bmatrix}, \quad (5.2)$$

where we chose the boundary conditions such that the diabatic and adiabatic curves agree for small separation. In panels (c), (d) and (e) of Fig. 5.1 we show the adiabatic curves corresponding to three distinct amplitudes of the diabatic coupling. From panel (c) to (e) the amplitude of the diabatic coupling is increased, leading to a weakening of the vibronic coupling as can be seen through the larger separation in the avoided crossing (see Eq. (2.37)). The three different values of the amplitude indicate three different regimes, which will be discussed in more detail in the following section.

The diagonalization also provides the transformation matrix \mathbf{U} of Eq. (2.44), which can be used to calculate the adiabatic dipole moments

Table 5.1: Field parameters of the IR and XUV pulses both defined by the vector potential Eq. (2.17). The CEP of both fields are 0.

	IR-pulse	XUV-pulse
Central Wavelength λ [nm]	3200	84
Central frequency ω [eV]	0.386	14.7
Intensity I [W/cm ²]	10^{13}	5×10^7
Duration T [fs]	32	0.56
Cycles N_c	3	2

through Eq. (2.50). We note that in the adiabatic representation the dipole moments will no longer be constant due to the mixing of the diabatic states at the crossing. From the transformation matrix it is also possible to calculate the first-order vibronic coupling P_{12} using Eq. (2.46). In sec. 2.4.3 we noted that the coupling is often well approximated by a Lorentzian, and proved in Eq. (2.58) that a constant diabatic coupling leads to a Lorentzian shape of the vibronic coupling. Numerical investigations showed that the Gaussian shape of the diabatic coupling would also lead to a vibronic coupling of Lorentzian shape, and that the width of the Gaussian was of little importance, as the value of the diabatic coupling near the crossing was the dominant factor. It therefore seems as an appropriate choice to use a Gaussian with fixed width and only vary the amplitude.

The XUV and the IR field are both defined by the vector potential given in Eq. (2.17), with the parameters given in tab. 5.1. Both fields are linearly polarized in the z-direction, which coincides with the internuclear axis of the molecule. The central frequency of the XUV is chosen to coincide with the energy needed to excite the ground state up to the excited state curves.

In the subsequent analysis we will compare the result of an “exact” calculation in the diabatic representation, where all couplings are included, with an “approximate” calculation in the adiabatic representation, where we use all potential energy curves and dipole couplings but omit the vibronic couplings. This lets us first directly examine the influence on the vibronic coupling on the spectra, and explore when the adiabatic approximation is sufficient. We note that even though we ignore the vibronic coupling for the adiabatic curves, the effect of the diabatic coupling is still present in the resulting energy gap at the avoided crossing.

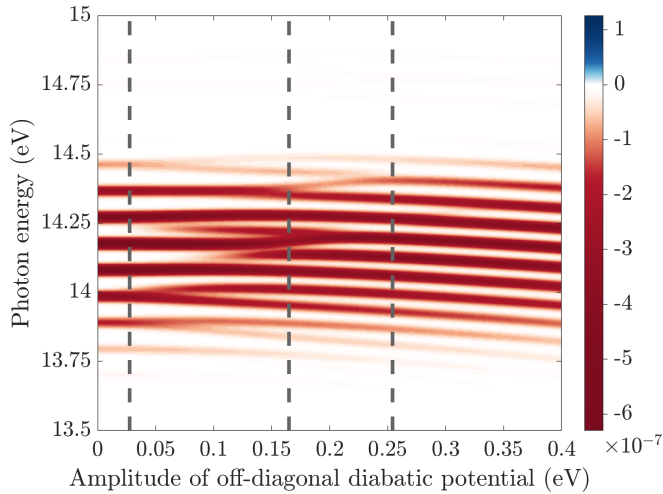


Figure 5.3: XUV-only spectra as a function of the amplitude of the off-diagonal diabatic potential for the exact diabatic curves. The three vertical dashed lines indicate values of the of the vibronic coupling corresponding to each of the three different regimes. From left to right; weak regime, intermediate regime and strong regime. See main text. Value of the response function is in arb. units.

5.2 XUV-only spectroscopy

We first calculate the spectrum from a simulation where we only apply the XUV, and not include the IR. We calculate this XUV-only spectrum for the exact diabatic and approximate adiabatic curves for varying values of the amplitude of the off-diagonal diabatic potential to highlight the difference between the two sets of curves. In Fig. 5.3 we show the spectrum of the exact diabatic curves, and in Fig 5.4 we show the corresponding spectrum for the approximate adiabatic curves, where the non-adiabatic coupling is neglected. The XUV-only absorption spectra allow us to see the impact of the vibronic coupling on the system. By comparing the spectra of the exact diabatic curves and the approximative adiabatic curves, we can also clearly see when omission of the vibronic coupling as a valid approximation.

For the approximate adiabatic curves in Fig. 5.4 there is only a small effect on the spectrum as the amplitude of the diabatic coupling is increased. Comparing the energy scale with the three different sets of adiabatic curves in Fig. 5.1, we see that the vibrational states we probe are all situated

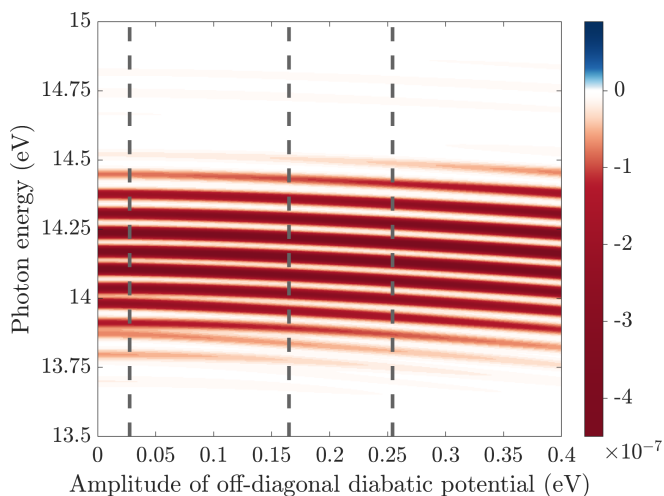


Figure 5.4: XUV-only spectra as a function of the amplitude of the off-diagonal diabatic potential of the approximate adiabatic curves. The three vertical dashed lines indicate specific values of the three different regimes. From left to right; weak regime, intermediate regime and strong regime. Value of the response function is in arb. units.

above where the adiabatic curves differ with the strength of coupling. We would therefore not expect a large change in these energy levels, as the potentials are only slightly perturbed as we omit the vibronic coupling.

For the exact diabatic curves in Fig. 5.3, we see a clear change of the absorption lines of the spectrum as the strength of the off-diagonal potential is increased. Based on the spectra and inspired by a similar analysis in ref. [25], we divide the curves into three regimes based on the amplitude of the off-diagonal diabatic potential; weak, intermediate and strong. In Fig. 5.3 and 5.4 we indicate three different values of the amplitude of the diabatic coupling that lies in each of the three regimes, and these three regimes will be used later in the analysis of the full ATA spectra.

In the weak regime the absorption lines are well separate, as would be expected since the coupling here can be neglected and we would therefore just see the vibrational energies of the harmonic diagonal diabatic curves. We note however, that the result is quite different compared with the approximate adiabatic curves. This is expected, since low amplitude of the diabatic coupling corresponds to a strong vibronic coupling (see Eq. (2.62)), with the latter being neglected in Fig. 5.4. However since the

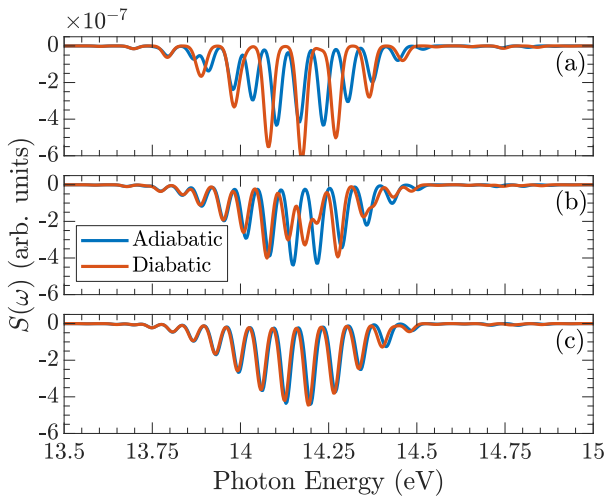


Figure 5.5: XUV only spectra as a function of the amplitude of the off-diagonal diabatic potential. (a) Weak regime, (b) intermediate regime and (c) strong regime. Red line is the spectrum for the exact diabatic curve, while the blue line is the spectrum for the approximate adiabatic curves.

vibronic coupling is very weak in this regime, one can get good results for the adiabatic curves by using a “crude diabaticization”, where one just connect opposite adiabatic curves over the avoided crossing to get a good approximation for the diabatic curves. In this picture it is also of no surprise that the absorption lines are well separated. The use of crude diabatic states have previously been used in the theoretical study of ATAS in N_2 in ref. [17].

In the intermediate regime the absorption lines now split and merge and the signal is overall more chaotic. This is the region of most interest, as the effect of the vibronic coupling has the biggest impact and where the spectra from the exact diabatic and approximate adiabatic differ the most when we take into account the possibility of using the crude diabaticization.

For the strong regime, the corresponding vibronic coupling will be small since the gap of the avoided crossing is large, and we therefore see that the two spectra are quite similar and the absorption lines are again regular and well defined. In this regime the adiabatic curves with neglected vibronic coupling is then expected to be a very good approximation, something we will analyse later for the full ATA spectra.

To see more clearly the differences and similarities between the spectra of Fig. 5.3 and 5.4 for the three different regimes, Fig. 5.5 shows the

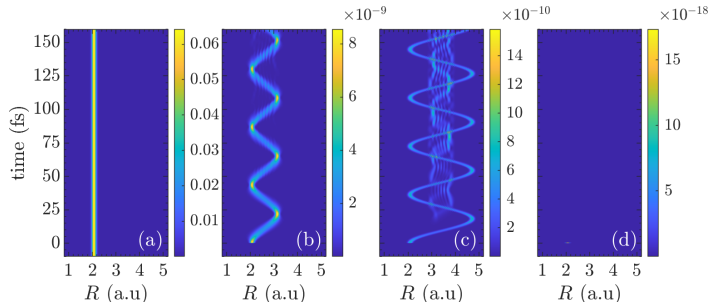


Figure 5.6: Density of the nuclear wave-packets on each of the four diabatic curves in the weak regime as a function of time for XUV-only spectroscopy with the XUV pulse incident at time 0 fs. (a) Wave-packet on ground state curve. (b) Wave-packet on first of the excited bright state curves. (c) Wave-packet on second excited bright state curve. (d) Wave-packet on dark state excited state curve.

absorption spectra of the three cuts. To reiterate; we see for the weak regime in (a) that the two spectra are quite different, but both spectra are regular with well-defined and well separated peaks. For the intermediate regime in (b) the adiabatic spectra is roughly the same, but the diabatic spectra is altered and there is some irregularity in the peaks around 14.2 eV. And for the strong regime in (c) the two spectra are nearly identical, both with regular peaks.

5.2.1 Dynamics of the nuclear wave-packets

To get a clearer view of the dynamics in the three different regimes and to further highlight where the similarities and differences between the exact diabatic and approximate adiabatic curves, we show the density of the individual wave-packets on each of the four curves in our model for the XUV-only spectroscopy. In each of the cases the XUV pulse is incident at time zero.

In Fig. 5.6 we see the nuclear dynamics on the exact diabatic curves in the weak regime. The ground state wave-packet in panel (a) is almost completely unchanged, as the intensity of the XUV is such that only a small part of the population is excited. Due to the small diabatic coupling, the wave-packets in panel (b) and (c) are mostly uncoupled, which is in accordance with the prediction of the Landau-Zener formula in Eq. (2.59), and perform simple oscillations. The highest lying excited state is dark with respect to the ground state, and there is therefore no significant

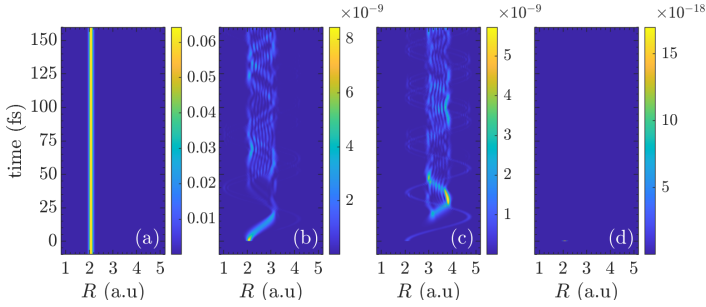


Figure 5.7: Density of the nuclear wave-packets on each of the four diabatic curves in the intermediate regime as a function of time for XUV-only spectroscopy with the XUV pulse incident at time 0 fs. (a) Wave-packet on ground state curve. (b) Wave-packet on first of the excited bright state curves. (c) Wave-packet on second excited bright state curve. (d) Wave-packet on dark state excited state curve.

excitation present with only the incident XUV.

For the diabatic curves in the intermediate regime depicted in Fig. 5.7 the behaviour of the wave-packet on the two lowest excited states in panel (b) and (c) are now much more chaotic. In panel (b) we can see how the wave-packet on the lowest excited state initial follows a simple oscillation until it reached the crossing at $R_c \sim 3$ a.u. The continuation of a significant part of the wave-packet can then be seen on the other excited curve in panel (c). After this wave-packet returns to the crossing, the mixing of the two states continue and becomes more chaotic.

In the strong regime in Fig. 5.8 the wave-packets on the two lowest excited diabatic curves are now so strongly coupled that every time they pass the crossing, we see an almost full transition between the two curves (again in accordance with the Landau-Zener model). We can compare this with the corresponding dynamics of the approximate adiabatic curves in the same regime shown in Fig. 5.9, where the two states uncoupled and there is no mixing of the states.

Calculation of the nuclear dynamics on the approximate adiabatic curves in the strong and weak regime are almost indistinguishable to the dynamics found in Fig. 5.9. This is as expected from the XUV-only spectrogram in Fig. 5.4, where there was only a small change of the energy levels probed by the XUV as the amplitude of the diabatic coupling was varied. This supports the physical intuition, that the omission of the vibronic approximation is a very good approximation in the strong diabatic

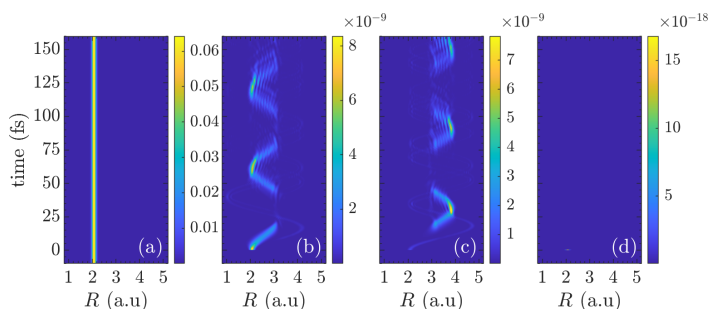


Figure 5.8: Density of the nuclear wave-packets on each of the four diabatic curves in the strong regime as a function of time for XUV-only spectroscopy with the XUV pulse incident at time 0 fs. (a) Wave-packet on ground state curve. (b) Wave-packet on first of the excited bright state curves. (c) Wave-packet on second excited bright state curve. (d) Wave-packet on dark state excited state curve.

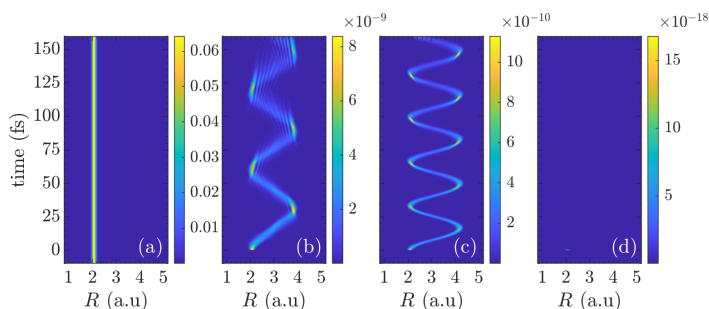


Figure 5.9: Density of the nuclear wave-packets on each of the four approximate adiabatic curves in the strong regime as a function of time for XUV-only spectroscopy with the XUV pulse incident at time 0 fs. (a) Wave-packet on ground state curve. (b) Wave-packet on first of the excited bright state curves. (c) Wave-packet on second excited bright state curve. (d) Wave-packet on dark state excited state curve.

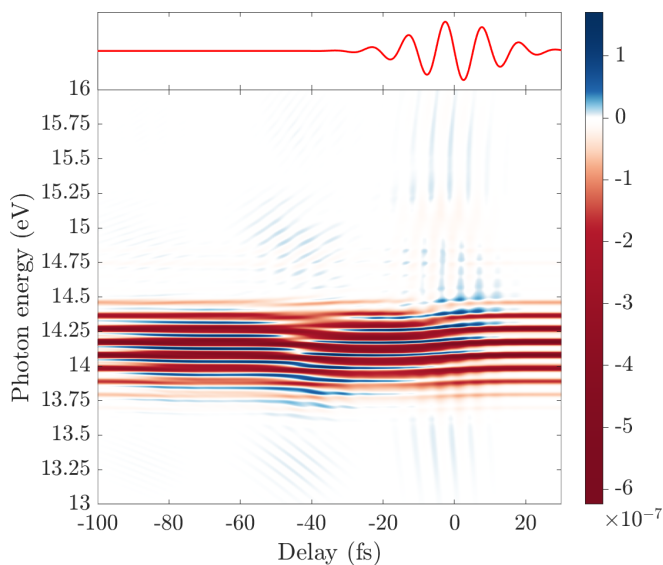


Figure 5.10: ATAS spectrum of exact diabatic curves for low amplitude of the diabatic coupling. The parameters of the XUV and the IR are given in table 5.1. An illustration of the IR pulse, centered at $\tau = 0$ fs, is shown in the top panel. The color scale to the right displays the signal strength in arbitrary units. For negative delays the XUV pulse will arrive first, while for positive delays the IR pulse arrive first.

regime where the corresponding vibronic coupling is small, and that the adiabatic approximation constitute a more appropriate representation as the coupling of the diabatic curves introduced a high degree of mixing. For the intermediate and weak regime the corresponding vibronic coupling is too strong to be neglected and the diabatic curves are the appropriate representation.

5.3 ATA spectra of the Model System

In this section we describe and analyse the ATA spectra of the model system for a set of the exact diabatic curves in each of the three regimes together with the approximate adiabatic curves in the strong regime as a comparison. We only include the adiabatic result for one regime, as the ATA spectra are, just like the case of the XUV-only, very similar for the three regimes.

We first consider the ATA spectrum of the exact diabatic curves in the

weak regime, which is shown in Fig. 5.10. For larger positive delays, the IR pulse arrives before the XUV. If enough time passes, such that there is no overlap between the two fields, the resulting spectra is equal to the XUV-only and we just see the delay-independent main absorption lines. For large negative delays, the two pulses are again well separated. Here the XUV arrives first and excites population onto the two bright state curves where the resulting wave packets will move, and later the incoming IR pulse will perturb these giving rise to the delay-dependent features. For the largest negative delays, the window function will have damped most of the signal and we mainly see modulation of the main absorption. The emission features seen between the absorption lines could be due to the hyperbolic sidebands, but they are hard to distinguish due to the closely lying vibrational states. At delays around -40 fs, still at a time where the two pulses are well separated, there are more abrupt changes of the main absorption lines where some of the lines split. There is also additional features around 15 and 13.25 eV at this delay. The features show both hyperbolic slopes away from the main lines as well as periodic modulation as a function of the time delay. The features are approximately spaced one IR frequency ~ 0.4 eV away from the absorption lines, and could therefore be the result of oscillating fringes. We argue later in sec. 5.3.1, that this seems to be correct. Around zero delay, where the two pulses overlap, we see the richest features. There is a modulation of both the main absorption lines, as well as the emission features between them as a function of the delay. Away from the main lines we see vertical features with a clear time delay modulation. Looking more closely at the different features away from the main absorption lines, we see that they all have the same oscillation around $2\omega_{\text{IR}}$, which corresponds to a period of ~ 5.4 fs.

We now consider the ATA spectrum of the exact diabatic curves in the intermediate regime in Fig. 5.11. Compared to the weak regime in Fig. 5.10 the main absorption lines are much more chaotic, as expected from the XUV-only analysis. In the intermediate regime, the absorption lines are so close that they often overlap, and it is therefore difficult to distinguish any possible emission features between them as could more clearly be seen in the weak regime. Similar to the weak regime, we see features attributed to the oscillating fringes at negative time delays around 15 and 13.25 eV. However the features now lie around -50 fs, instead of -40 fs, an effect we will see even more pronounced in the strong regime. The features at -50 fs are also weaker here than compared to the weak regime, and as we see later to the strong regime. The features due to the fringes and LIS centered at zero time delay are not altered significantly

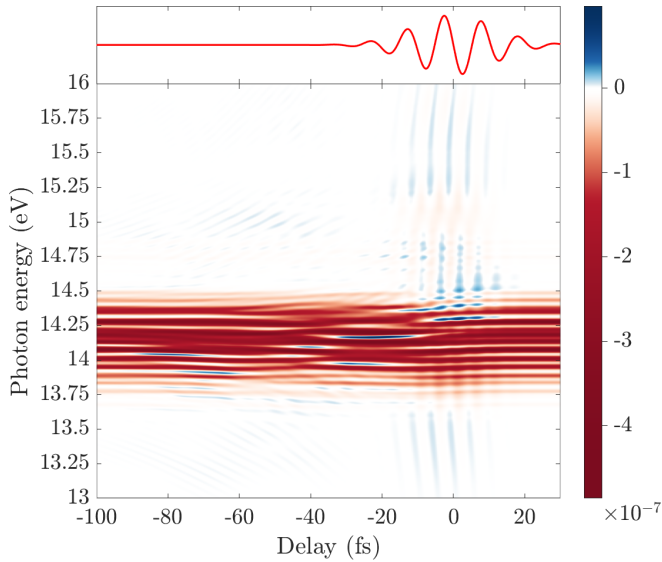


Figure 5.11: ATAS spectrum of exact diabatic curves for intermediate amplitude of the diabatic coupling. The parameters of the XUV and the IR are given in table 5.1. An illustration of the IR pulse, centered at $\tau = 0$ fs, is shown in the top panel. The color scale to the right displays the signal strength in arbitrary units. For negative delays the XUV pulse will arrive first, while for positive delays the IR pulse arrive first.

compared to the weak regime.

In Fig. 5.12 we consider the ATA spectrum of the exact diabatic curves in the strong regime. In the strong regime, the main absorption lines are now back to being well separated. Compared to the weak regime, where the lines are also well defined, we see much weaker emission lines. The oscillating fringes at 15 and 13.25 eV for negative delays are now situated at -60 fs, and have moved to further negative delay compared to the -40 fs for the weak regime and -50 fs for the intermediate regime. If we compare these three delay times with the nuclear dynamics of Fig. 5.6, 5.7 and 5.8, we see that it coincides roughly with the time it takes for the excited wave-packet to propagate out and return to the Frank-Condon window of the ground state. The feature at negative delay could

Again there is not much change to the features coming from the oscillating fringes and LIS at zero delay compared to the two other regimes.

Finally we include the ATA spectrum calculated using the approximate adiabatic curves for strong diabatic coupling. The spectrum is shown in

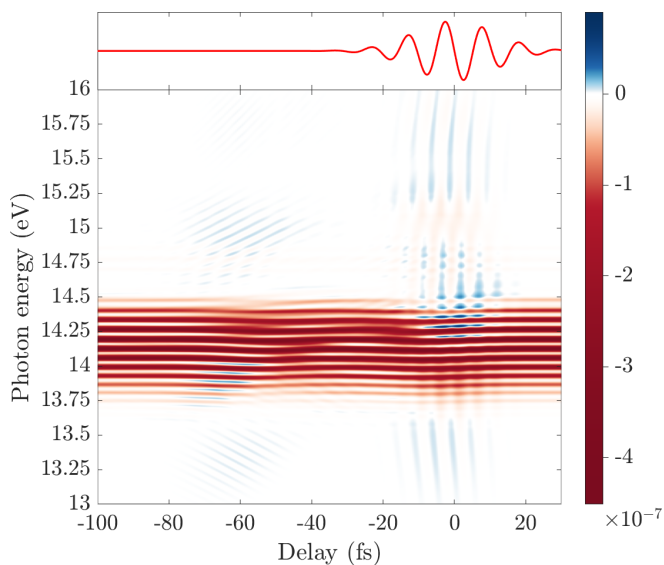


Figure 5.12: ATAS spectrum of exact diabatic curves for strong amplitude of the diabatic coupling. The parameters of the XUV and the IR are given in table 5.1. An illustration of the IR pulse, centered at $\tau = 0$ fs, is shown in the top panel. The color scale to the right displays the signal strength in arbitrary units. For negative delays the XUV pulse will arrive first, while for positive delays the IR pulse arrive first.

Fig. 5.13. In the strong regime the vibronic coupling is weak, and our omission of this for the adiabatic curves is a good approximation. This is further justified when we compare the approximate adiabatic spectrum with the corresponding exact diabatic spectrum in the same regime Fig. 5.12, where we see that the two spectra are almost identical. Calculating the ATA spectrum of the approximate adiabatic curves for the two other regimes, there is only a slight altering as the strength of the diabatic coupling is changed.

5.3.1 Using the Multi-level model

In our analysis of the features of the ATA spectra of LiF in chap. 4, we could use the adiabatic two-level model of sec. 2.6. In the case of our model system, it is clear from both the ATAS and the XUV-only spectra that multiple excited levels are at play. To analyse the spectra we will therefore used the multi-level expansion of the adiabatic three-level model derived in sec. 2.5.2.

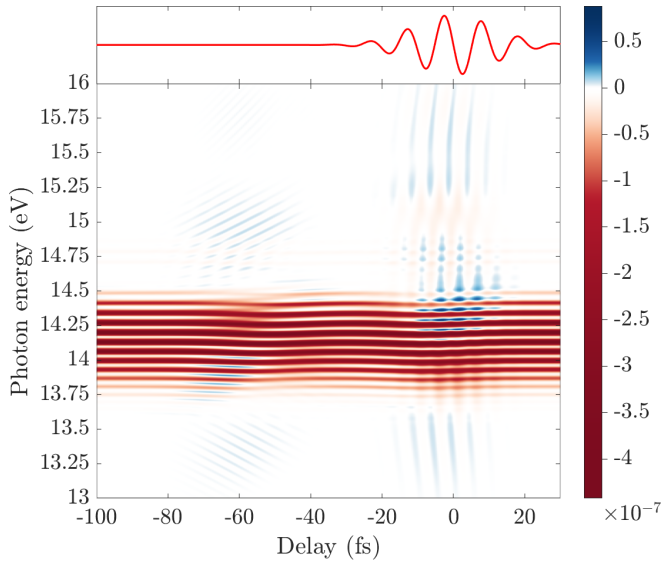


Figure 5.13: ATAS spectrum of approximate adiabatic curves for strong amplitude of the diabatic coupling. The parameters of the XUV and the IR are given in table 5.1. An illustration of the IR pulse, centered at $\tau = 0$ fs, is shown in the top panel. The color scale to the right displays the signal strength in arbitrary units. For negative delays the XUV pulse will arrive first, while for positive delays the IR pulse arrive first.

The response function of the multi-level model for the sidebands and fringes in Eq. (2.105) and the LIS in Eq. (2.106) extends the simpler three-level model, by including and summing the signal of all possible sub three-level systems. This is a very crude model, and it will in general provide too strong a signal due to the combinatorial nature of including all levels. The model can provide some quantitative insight to the collective effects that happen when several levels are included, but more investigation is needed to determine more clearly the range of validity of the model and possible adjustment that can be made to produce more useful results.

We present here briefly some of the results of the model, with a focus on the description of the oscillating fringes. Fig. 5.14 shows the response function Eq. (2.105) responsible for the fringes for the exact diabatic curves in the weak regime. We further simplify the response function by neglecting the intra-manifold coupling arising from the intersection of different bright states mediate by a dark state, and focus on the inter-manifold term coupling. The function is calculated by summing over the

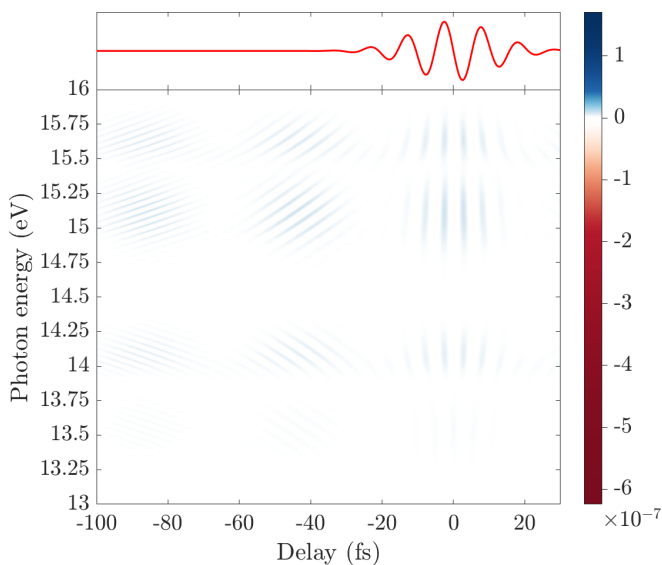


Figure 5.14: Analytical response function of the oscillating fringes Eq. (2.105) coming from the inter-manifold coupling for the exact diabatic curves for weak amplitude of the diabatic coupling.

lowest 25 vibrational state in each of the excited curves. Comparing with the full numerical result in Fig. 5.10, the model recreates the fringes at the correct energies of 15 and 13.25 eV, delay at 0 and -40 fs and with the same delay dependent period of $2\omega_{\text{IR}}$. There is an additional feature at -80 fs, which is not present in the full model. The signal at -40 fs was explained by the excited wave-packet completing one oscillation and returning to the Frank-Condon window of the ground state, and the signal at -80 fs can therefore be explain by the same process happening after two full oscillations. In the full numerical model the dipole is dampened by the Window function, and the signal for this second arrival is extinguished. We further see some additional fringes at energies around 15.7 eV, which are not present in the full numerical spectra.

Fig. 5.15 response function for the fringes for the exact diabatic curves in the intermediate regime. In this figure the accordance with the corresponding full numerical spectrum in Fig. 5.12 is worse, which much stronger additional features, and the revival signal of the fringes at -50 fs is less distinguished. For the diabatic curves in the strong regime in Fig. 5.16 the revival fringes are pronounced again, but the additional fringes are even stronger. These trends suggest that the model breaks down in the presence

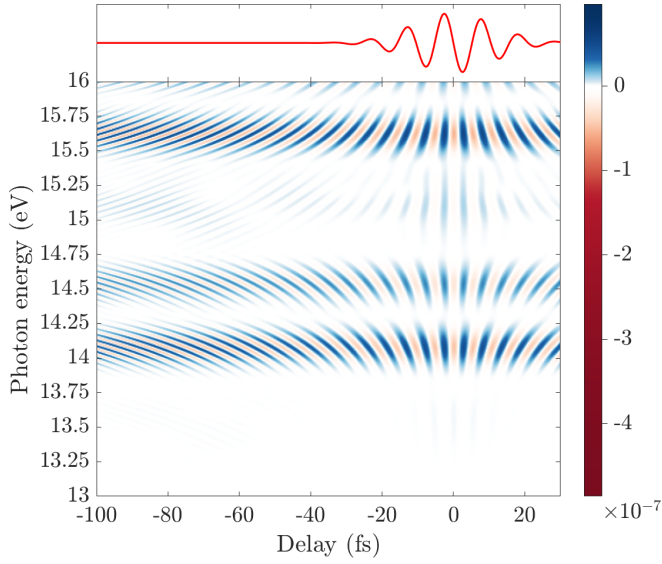


Figure 5.15: Analytical response function of the oscillating fringes Eq. (2.105) coming from the inter-manifold coupling for the exact diabatic curves for intermediate amplitude of the diabatic coupling.

of a significant diabatic coupling and works best in the weak regime. This is further supporter by the spectrum calculated for the approximative adiabatic curves in the strong regime in Fig. 5.17, which has a good agreement with the corresponding full numerical result in Fig. 5.13.

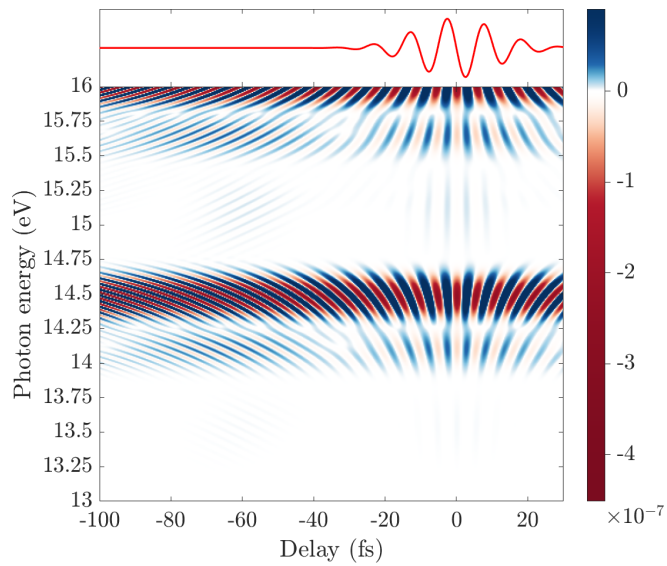


Figure 5.16: Analytical response function of the oscillating fringes Eq. (2.105) coming from the inter-manifold coupling for the exact diabatic curves for strong amplitude of the diabatic coupling.

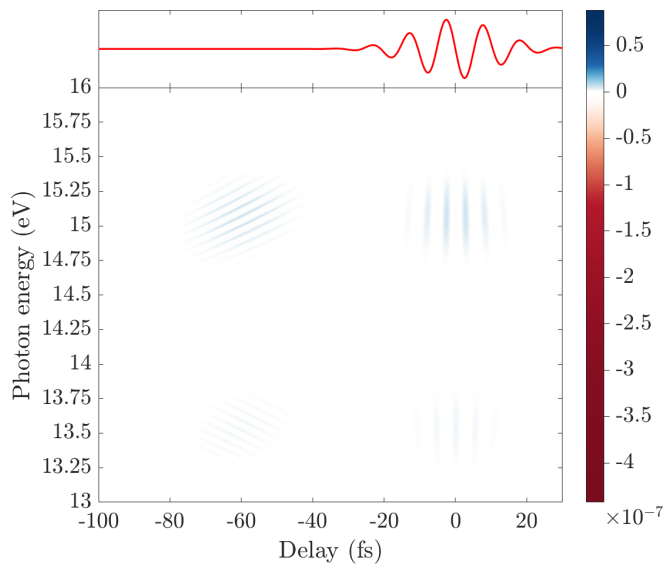


Figure 5.17: Analytical response function of the oscillating fringes Eq. (2.105) coming from the inter-manifold coupling for the approximate adiabatic curves for strong amplitude of the diabatic coupling.

Summary and Outlook

In this thesis we have presented a comprehensive description of the underlying theory of attosecond transient absorption spectroscopy in diatomic molecules.

In Chapter 2 we gave a review of the response function, which through the time-dependent dipole moment of the molecule, provides a way to reproduce features of the rich spectrograms. We described in detail the adiabatic and diabatic representation needed in the description of the quantum model of the diatomic molecule, and compared the advantages and disadvantages of the two representations with a focus of the vibronic coupling arising at the avoided crossings. Lastly we derived a series of semi analytical models useful in the description of the most fundamental features present in the ATA spectra.

Chapter 3 described the standard numerical methods used in the simulation of the interaction of the molecule with the incoming field, as well as general techniques used in the subsequent analysis.

In Chapter 4 we studied ATAS in the context of a polar diatomic molecule exemplified by the LiF system. Polar molecules break inversion symmetry, which opens up more pathways and therefore leads to new features. The obtained spectra of LiF calculated using the full numerical model showed in particular two new interesting features; LIS situated one NIR photon away from the main absorption line, and an additional new ladder structure with the rungs separated by one NIR photon. The LIS have previously only been seen surrounding dark states, but can for polar molecules occur around the bright states as the electronic states are no longer of definite parity. Through the use of a fixed-nuclei model derived in chap. 2 we could show some of the dependencies of the different features.

Importantly we saw that both the LIS and the ladder were dependent on $D_{22} - D_{11}$, implying that nonpolar molecules would not exhibit these in their spectra. We further compared the two different experimental scenarios of alignment and orientation, where we saw how the mixture of the signal for the aligned sample would lead to the extinguish of some of the features.

For further studies into the dynamics of LiF or polar molecules in general one could e.g. explore the effects of including more than just two potential energy curves. The dissociative shape of the excited state lead to a fast dephasing of the dipole signal, and comparing the spectrum of LiF to is polar system with a binding excited state could also be of interest. Recently our adiabatic two-level model for the polar system was extended and used to describe ATAS in non-centrosymmetric systems in ref. [58], and further investigations into other areas of its applicability could be of interest.

Chapter 5 was concerned with the study of a model system with an avoided crossing between two of the excited states. The model system allowed us full control of the vibronic coupling of the crossing through the amplitude of the corresponding diabatic coupling. Through absorption spectra calculated with only the presence of the XUV, we could divide the different set of curves in to three distinct regimes based on the strength of the diabatic coupling. From the full numerical spectra of the model calculated for the exact diabatic and approximate adiabatic curves, we could examine the effect of the crossing and determine when omission of the non-adiabatic features constituted a valid approximation. We further employed a multi-level model to aid in the description of the oscillating fringes. The model showed promise for the exact diabatic curves in the weak regime and for the approximate adiabatic curves in the strong regime.

In the full numerical simulation the model system showed promise in description of non-adiabatic effects through the comparison of the exact diabatic and approximative adiabatic curves. Studies of interest could be in changing the shape of the excited states; such that some states are dissociative instead of binding, the avoided crossing is moved further out or the introduction of multiple crossings. The multi-level model used in the description of the oscillating fringes was less successful, and an obvious path for further work would be to more closely investigate its used and determine its range of validity.

Fourier Transforms of the fields

In this appendix we briefly outline how the different Fourier transforms of the fields are calculated. This is based entirely on the work in [11] and [1].

Both the IR and the XUV fields are defined by the vector potential Eq. (2.17)

$$A(t) = A_0 e^{-\frac{4(t-t_c)^2}{T^2}} \cos[\omega(t-t_c)], \quad (\text{A.1})$$

through the relation

$$F(t) = -\partial_t A(t) \quad (\text{A.2})$$

$$= F_0 e^{-\frac{4(t-t_c)^2}{T^2}} \left\{ \frac{8(t-t_c)}{\omega T^2} \cos[\omega(t-t_c)] + \sin[\omega(t-t_c)] \right\}, \quad (\text{A.3})$$

with $F_0 = \omega A_0$.

The IR field is centered around $t_c = 0$, and since the duration T_{IR} is relatively large we will neglect the first term,

$$F_{\text{IR}}(t) = F_{0,\text{IR}} e^{-\frac{4t^2}{T_{\text{IR}}^2}} \sin[\omega_{\text{IR}} t]. \quad (\text{A.4})$$

We reiterate here that we use the unitary, angular frequency definition of the Fourier transform

$$\mathcal{F}[f(t)](\omega) = \frac{1}{\sqrt{2\pi}} \int_{\mathbb{R}} dt f(t) e^{-i\omega t}. \quad (\text{A.5})$$

For the Light-induced structures we need the Fourier transform of the IR pulse multiplied by an exponential

$$\mathcal{F}\left[F_{\text{IR}}(t)e^{iE_d t}\right](\omega) = \frac{F_{0,\text{IR}}}{2i} \left\{ \mathcal{F}\left[e^{-\frac{4t^2}{T_{\text{IR}}^2}} e^{i(E_d+\omega_{\text{IR}})t}\right](\omega) - \mathcal{F}\left[e^{-\frac{4t^2}{T_{\text{IR}}^2}} e^{i(E_d-\omega_{\text{IR}})t}\right](\omega) \right\}. \quad (\text{A.6})$$

Using the shift property of the Fourier transform

$$\mathcal{F}\left[f(t)e^{iat}\right](\omega) = \mathcal{F}\left[f(t)\right](\omega - a), \quad (\text{A.7})$$

we find

$$\mathcal{F}\left[F_{\text{IR}}(t)e^{iE_d t}\right](\omega) = \frac{F_{0,\text{IR}}}{2i} \left\{ \mathcal{F}\left[e^{-\frac{4t^2}{T_{\text{IR}}^2}}\right](\omega - E_d - \omega_{\text{IR}}) - \mathcal{F}\left[e^{-\frac{4t^2}{T_{\text{IR}}^2}}\right](\omega - E_d + \omega_{\text{IR}}) \right\}. \quad (\text{A.8})$$

The Fourier transform of a Gaussian is just another Gaussian

$$\mathcal{F}\left[e^{-at^2}\right](\omega) = \frac{1}{\sqrt{2a}} e^{-\frac{\omega^2}{4a}}. \quad (\text{A.9})$$

Using this finally yields us

$$\mathcal{F}\left[F_{\text{IR}}(t)e^{iE_d t}\right](\omega) = \frac{F_{0,\text{IR}} T_{\text{IR}}}{i4\sqrt{2}} \left\{ e^{-\frac{T_{\text{IR}}^2(\omega - E_d - \omega_{\text{IR}})^2}{16}} - e^{-\frac{T_{\text{IR}}^2(\omega - E_d + \omega_{\text{IR}})^2}{16}} \right\}. \quad (\text{A.10})$$

For the hyperbolic sidebands and the oscillating fringes we need the Fourier transforms of two different terms. The first term is the square of the IR pulse multiplied by a phase

$$\mathcal{F}\left[F_{\text{IR}}^2(t)e^{iE_d t}\right](\omega) = F_{0,\text{IR}}^2 \mathcal{F}\left[e^{-\frac{8t^2}{T_{\text{IR}}^2}} \sin^2(\omega_{\text{IR}} t) e^{iE_d t}\right](\omega) \quad (\text{A.11})$$

$$= -\frac{F_{0,\text{IR}}^2}{4} \left\{ \mathcal{F}\left[e^{-\frac{8t^2}{T_{\text{IR}}^2}} e^{i(E_d+2\omega_{\text{IR}})t}\right] + \mathcal{F}\left[e^{-\frac{8t^2}{T_{\text{IR}}^2}} e^{i(E_d-2\omega_{\text{IR}})t}\right] - 2\mathcal{F}\left[e^{-\frac{8t^2}{T_{\text{IR}}^2}} e^{iE_d t}\right] \right\} \quad (\text{A.12})$$

$$= -\frac{F_{0,\text{IR}}^2 T_{\text{IR}}}{16} \left\{ e^{-\frac{T_{\text{IR}}^2(\omega - E_d - 2\omega_{\text{IR}})^2}{32}} + e^{-\frac{T_{\text{IR}}^2(\omega - E_d + 2\omega_{\text{IR}})^2}{32}} - 2e^{-\frac{T_{\text{IR}}^2(\omega - E_d)^2}{32}} \right\} \quad (\text{A.13})$$

The second Fourier transform needed, is of the integral over the square of the field. To calculate the transform we first split up the time integral

$$\int_{\tau}^t dt' F_{\text{IR}}^2(t') = \int_0^t dt' F_{\text{IR}}^2(t') + \int_{\tau}^0 dt' F_{\text{IR}}^2(t'). \quad (\text{A.14})$$

The second integral is now independent of the time t , and will be neglected since it will only contribute to a small change of the main absorption line. For the first integral we can further write, using that the integrand is even,

$$\int_0^t dt' F_{\text{IR}}^2(t') = \frac{1}{2} \int_{-t}^t dt' F_{\text{IR}}^2(t') \quad (\text{A.15})$$

$$= \frac{1}{2} \left\{ \int_{-\infty}^{-t} dt' F_{\text{IR}}^2(t') + \int_{-t}^t dt' F_{\text{IR}}^2(t') - \int_t^{\infty} dt' F_{\text{IR}}^2(t') \right\} \quad (\text{A.16})$$

$$= \frac{1}{2} \int_{-\infty}^{\infty} dt' \text{sgn}(t - t') F_{\text{IR}}^2(t'), \quad (\text{A.17})$$

where $\text{sgn}(t)$ is the sign function. The Fourier transform of this term is now of the form of a convolution

$$(f * g)(t) = \int_{-\infty}^{\infty} dt' f(t - t')g(t'), \quad (\text{A.18})$$

where the Fourier transform becomes a product

$$\mathcal{F}[(f * g)(t)](\omega) = \sqrt{2\pi} \mathcal{F}[f(t)](\omega) \mathcal{F}[g(t)](\omega). \quad (\text{A.19})$$

The Fourier transform of the sign function is

$$\mathcal{F}[\text{sgn}(t)] = \sqrt{\frac{2}{\pi}} \frac{1}{i\omega}, \quad (\text{A.20})$$

and combining all this we get

$$\mathcal{F}\left[\int_{\tau}^t dt' F_{\text{IR}}^2(t') e^{iE_d t'}\right](\omega) = \mathcal{F}\left[\int_{\tau}^t dt' F_{\text{IR}}^2(t')\right](\omega - E_d) \quad (\text{A.21})$$

$$= \frac{\sqrt{2\pi}}{2} \mathcal{F}[\text{sgn}(t)](\omega - E_d) \mathcal{F}[F_{\text{IR}}^2(t)](\omega - E_d) \quad (\text{A.22})$$

$$= \frac{1}{i(\omega - E_d)} \mathcal{F}[F_{\text{IR}}^2(t)](\omega - E_d) \quad (\text{A.23})$$

$$= -\frac{F_{0,\text{IR}}^2 T_{\text{IR}}}{i16} \frac{1}{\omega - E_d} \left\{ e^{-\frac{T_{\text{IR}}^2 (\omega - E_d - 2\omega_{\text{IR}})^2}{32}} + e^{-\frac{T_{\text{IR}}^2 (\omega - E_d - 2\omega_{\text{IR}})^2}{32}} - 2e^{-\frac{T_{\text{IR}}^2 (\omega - E_d)^2}{32}} \right\} \quad (\text{A.24})$$

In the treatment of the heteronuclear LiF molecule, we consider an XUV field in a regime where we want to include the effect of the spectral width not contained in the approximation of the delta function in time where the Fourier transform is a constant. For the LiF molecule we also wanted to test the effect of orientation compared to alignment, and to do this we include the phases φ of both fields.

The XUV is centered at τ

$$F_{\text{XUV}}(t) = F_{0,\text{XUV}} e^{-\frac{4(t-\tau)^2}{T_{\text{XUV}}^2}} \left\{ \frac{8(t-\tau)}{\omega_{\text{XUV}} T_{\text{XUV}}^2} \cos \left[\omega_{\text{XUV}}(t-\tau) + \varphi \right] + \sin \left[\omega_{\text{XUV}}(t-\tau) + \varphi \right] \right\}. \quad (\text{A.25})$$

As we have used earlier, we need only to consider the exponentials with positive phases

$$F_{\text{XUV}}(t) = \frac{4F_{0,\text{XUV}}}{\omega_{\text{XUV}} T_{\text{XUV}}^2} (t-\tau) e^{i\omega_{\text{XUV}}(t-\tau)} e^{i\varphi} e^{-\frac{4(t-\tau)^2}{T_{\text{XUV}}^2}} \quad (\text{A.26})$$

$$+ \frac{F_{0,\text{XUV}}}{2i} e^{i\omega_{\text{XUV}}(t-\tau)} e^{i\varphi} e^{-\frac{4(t-\tau)^2}{T_{\text{XUV}}^2}}. \quad (\text{A.27})$$

The Fourier transform is found, by first using the time shift property

$$\mathcal{F}[f(t-t')](\omega) = e^{-i\omega t'} \mathcal{F}[f(t)](\omega), \quad (\text{A.28})$$

and after that the shift in frequency in Eq. (A.7)

$$\begin{aligned} \mathcal{F}[F_{\text{XUV}}(t)](\omega) &= \frac{4F_{0,\text{XUV}}}{\omega_{\text{XUV}} T_{\text{XUV}}^2} e^{-i\omega\tau} e^{i\varphi} \mathcal{F}\left[te^{i\omega_{\text{XUV}}t} e^{-\frac{4t^2}{T_{\text{XUV}}^2}}\right](\omega) \\ &+ \frac{F_{0,\text{XUV}}}{2i} e^{-i\omega\tau} e^{i\varphi} \mathcal{F}\left[e^{i\omega_{\text{XUV}}t} e^{-\frac{4t^2}{T_{\text{XUV}}^2}}\right](\omega) \end{aligned} \quad (\text{A.29})$$

$$\begin{aligned} &= \frac{4F_{0,\text{XUV}}}{\omega_{\text{XUV}} T_{\text{XUV}}^2} e^{-i\omega\tau} e^{i\varphi} \mathcal{F}\left[te^{-\frac{4t^2}{T_{\text{XUV}}^2}}\right](\omega - \omega_{\text{XUV}}) \\ &+ \frac{F_{0,\text{XUV}}}{2i} e^{-i\omega\tau} e^{i\varphi} \mathcal{F}\left[e^{-\frac{4t^2}{T_{\text{XUV}}^2}}\right](\omega - \omega_{\text{XUV}}). \end{aligned} \quad (\text{A.30})$$

Finally using the algebraic property

$$\mathcal{F}[tf(t)](\omega) = i \frac{d}{d\omega} \mathcal{F}[f(t)](\omega), \quad (\text{A.31})$$

we get, using the Fourier transform of the Gaussian in Eq. (A.9),

$$\mathcal{F}\left[F_{\text{XUV}}(t)\right](\omega) = i \frac{4F_{0,\text{XUV}}}{\omega_{\text{XUV}} T_{\text{XUV}}^2} e^{-i\omega\tau} e^{i\varphi} \frac{d}{d\omega} \frac{T_{\text{XUV}}}{2\sqrt{2}} e^{-\frac{T_{\text{XUV}}^2(\omega - \omega_{\text{XUV}})^2}{16}} \quad (\text{A.32})$$

$$\begin{aligned} &+ \frac{F_{0,\text{XUV}}}{2i} e^{-i\omega\tau} e^{i\varphi} \frac{T_{\text{XUV}}}{2\sqrt{2}} e^{-\frac{T_{\text{XUV}}^2(\omega - \omega_{\text{XUV}})^2}{16}} \\ &= -i \frac{F_{0,\text{XUV}} T_{\text{XUV}}}{4\sqrt{2}} \frac{\omega}{\omega_{\text{XUV}}} e^{-i\omega\tau} e^{i\varphi} e^{-\frac{T_{\text{XUV}}^2(\omega - \omega_{\text{XUV}})^2}{16}}. \end{aligned} \quad (\text{A.33})$$

In the description of the ladder structure, we also need the Fourier transform of the IR field to multiple orders

$$\mathcal{F}\left[F_{\text{IR}}^n(t)\right] = \mathcal{F}\left[F_{0,\text{IR}}^n \sin^n(\omega_{\text{IR}}t + \varphi) e^{-\frac{4n^2 t^2}{T_{\text{IR}}^2}}\right](\omega), \quad (\text{A.34})$$

where we again use the Eq. (A.4) expression for the IR field. For the different powers of the sine carrier we have, using the binomial theorem,

$$F_{0,\text{IR}}^n \sin^n(\omega_{\text{IR}}t + \varphi) = \frac{F_{0,\text{IR}}^n}{(2i)^n} \left(e^{i\omega_{\text{IR}}t} e^{i\varphi} - e^{-i\omega_{\text{IR}}t} e^{-i\varphi} \right)^n \quad (\text{A.35})$$

$$= \frac{F_{0,\text{IR}}^n}{(2i)^n} \sum_{k=0}^n \binom{n}{k} e^{ik\omega_{\text{IR}}t} e^{ik\varphi} (-1)^{n-k} e^{-i(n-k)\omega_{\text{IR}}t} e^{-i(n-k)\varphi} \quad (\text{A.36})$$

$$= F_{0,\text{IR}}^n \left(\frac{-i}{2} \right)^n \sum_{k=0}^n (-1)^{n-k} \binom{n}{k} e^{i(2k-n)\omega_{\text{IR}}t} e^{i(2k-n)\varphi}. \quad (\text{A.37})$$

This sum will contain exponentials with phases $e^{in\omega_{\text{IR}}t}$, $e^{i(n-2)\omega_{\text{IR}}t}$, \dots , $e^{-n\omega_{\text{IR}}t}$, i.e. we get a given power from more than one power of the carrier. The terms will fall off with the intensity, and we will therefore only keep the first term. We will further only keep the positive phases, as we have done earlier. We therefore get

$$\mathcal{F}[F_{\text{IR}}^n(t)](\omega) \approx F_{0,\text{IR}}^n \left(\frac{-i}{2}\right)^n e^{in\varphi} \mathcal{F}\left[e^{-\frac{4nt^2}{T_{\text{IR}}^2}} e^{in\omega_{\text{IR}}t}\right](\omega) \quad (\text{A.38})$$

$$= F_{0,\text{IR}}^n \left(\frac{-i}{2}\right)^n e^{in\varphi} \mathcal{F}\left[e^{-\frac{4nt^2}{T_{\text{IR}}^2}}\right](\omega - n\omega_{\text{IR}}) \quad (\text{A.39})$$

$$= \frac{F_{0,\text{IR}}^n T_{\text{IR}}}{2\sqrt{2n}} \left(\frac{-i}{2}\right)^n e^{in\varphi} e^{-\frac{T_{\text{IR}}^2(\omega - n\omega_{\text{IR}})^2}{16n}} \quad (\text{A.40})$$

Adiabatic Multi-Level model

In this appendix we shown in more detail how the two analytical response functions Eq. (2.105) and Eq. (2.106) of the adiabatic three-level model are calculated.

We found the second order adiabatic energies

$$E_{ba,n} = E_{b,n} - \sum_m \frac{D_{b,n;d,m}^2 F_{\text{IR}}^2}{E_{d,m} - E_{b,n}} \quad (\text{B.1})$$

$$E_{da,m} = E_{d,m} + \sum_n \frac{D_{b,n;d,m}^2 F_{\text{IR}}^2}{E_{d,m} - E_{b,n}}, \quad (\text{B.2})$$

and dressed states

$$\begin{aligned} |\psi_{ba,n}\rangle &= \left(1 - \frac{1}{2} \sum_m \frac{D_{b,n;d,m}^2 F_{\text{IR}}^2}{(E_{d,m} - E_{b,n})^2} \right) |\psi_{b,n}\rangle + \sum_m \frac{d_{b,n;d,m} F_{\text{IR}}}{E_{d,m} - E_{b,n}} |\psi_{d,m}\rangle \\ &+ \sum_m \sum_{k \neq n} \frac{D_{b,k;d,m} D_{b,n;d,m} F_{\text{IR}}^2}{(E_{d,m} - E_{b,n})(E_{b,k} - E_{b,n})} |\psi_{b,k}\rangle \end{aligned} \quad (\text{B.3})$$

$$\begin{aligned} |\psi_{da,m}\rangle &= - \sum_n \frac{d_{b,n;d,m} F_{\text{IR}}}{E_{d,m} - E_{b,n}} |\psi_{b,n}\rangle + \left(1 - \frac{1}{2} \sum_n \frac{D_{b,n;d,m}^2 F_{\text{IR}}^2}{(E_{d,m} - E_{b,n})^2} \right) |\psi_{d,m}\rangle \\ &+ \sum_n \sum_{l \neq m} \frac{D_{b,n;d,m} D_{b,n;d,l} F_{\text{IR}}^2}{(E_{d,m} - E_{b,n})(E_{d,m} - E_{d,l})} |\psi_{d,l}\rangle. \end{aligned} \quad (\text{B.4})$$

Using these states, we write the full wave function as

$$|\Psi_a\rangle = a_g(t)|\psi_g\rangle + \sum_n a_{b,n}(t)e^{-i\int_\tau^t dt' E_{ba,n}}|\psi_{ba,n}\rangle + \sum_m a_{d,m}(t)e^{-i\int_\tau^t dt' E_{da,m}}|\psi_{da,m}\rangle. \quad (\text{B.5})$$

Working to first order in the weak XUV field, we find the following equations for the expansion coefficients

$$\dot{a}_{b,n}^{(1)} = iF_{\text{XUV}}\langle\psi_{ab,n}|\hat{D}|\psi_g\rangle e^{i\int_\tau^t dt' E_{ba,n}} \quad (\text{B.6})$$

$$\dot{a}_{d,m}^{(1)} = iF_{\text{XUV}}\langle\psi_{ad,m}|\hat{D}|\psi_g\rangle e^{i\int_\tau^t dt' E_{da,m}}, \quad (\text{B.7})$$

where we have neglected all non-adiabatic terms containing $\langle\psi_{ba,n}|\dot{\psi}_{da,m}\rangle$, $\langle\psi_{da,m}|\dot{\psi}_{ba,n}\rangle$, $\langle\psi_{ba,n}|\dot{\psi}_{ba,n}\rangle$ and $\langle\psi_{da,m}|\dot{\psi}_{da,m}\rangle$. The matrix elements of the dipole operator between the ground and the two dressed states are

$$\langle\psi_{ba,n}|\hat{D}|\psi_g\rangle = D_{g;b,n}\left(1 - \frac{1}{2}\sum_m \frac{D_{b,n;d,m}^2 F_{\text{IR}}^2}{(E_{d,m} - E_{b,n})^2}\right) + \sum_m \sum_{k \neq n} D_{g;b,k} \frac{D_{b,k;d,m} D_{b,n;d,m} F_{\text{IR}}^2}{(E_{d,m} - E_{b,n})(E_{b,k} - E_{b,n})} \quad (\text{B.8})$$

$$\langle\psi_{da,m}|\hat{D}|\psi_g\rangle = -\sum_n D_{g;b,n} \frac{D_{b,n;d,m} F_{\text{IR}}}{E_{d,m} - E_{b,n}}, \quad (\text{B.9})$$

to second order in the IR field.

Using the approximation of the short XUV pulse as a delta function $F_{\text{XUV}}(t - \tau) \rightarrow \gamma(t - \tau)$, we can solve the differential equations for the expansion coefficients

$$a_{b,n}^{(1)}(t) = i\gamma\theta(t - \tau)\left\{D_{g;b,n}\left(1 - \frac{1}{2}\sum_m \frac{D_{b,n;d,m}^2 F_{\text{IR}}^2(\tau)}{(E_{d,m} - E_{b,n})^2}\right) + \sum_m \sum_{k \neq n} D_{g;b,k} \frac{D_{b,k;d,m} D_{b,n;d,m} F_{\text{IR}}^2(\tau)}{(E_{d,m} - E_{b,n})(E_{b,k} - E_{b,n})}\right\} \quad (\text{B.10})$$

$$a_{d,m}^{(1)}(t) = -i\gamma\theta(t - \tau)\sum_n D_{g;b,n} \frac{D_{b,n;d,m} F_{\text{IR}}(\tau)}{E_{d,m} - E_{b,n}}. \quad (\text{B.11})$$

To first order in the XUV field, the time-dependent dipole moment of the wave function is

$$\begin{aligned} \langle D \rangle_a &= \sum_n \left[a_{b,n}^{(1)} \right]^* \langle \psi_{ba,n} | \hat{D} | \psi_g \rangle e^{i \int_\tau^t dt' E_{ba,n}} \\ &\quad + \sum_m \left[a_{d,m}^{(1)} \right]^* \langle \psi_{da,m} | \hat{D} | \psi_g \rangle e^{i \int_\tau^t dt' E_{da,m}}, \end{aligned} \quad (\text{B.12})$$

where we have only included the terms with positive phases. Following the approach of the three-level model, we treat the two terms separately.

For the first term of the dipole we have

$$\begin{aligned} \langle D \rangle_{a1} &= \sum_n \left[a_{b,n}^{(1)} \right]^* \langle \psi_{ba,n} | \hat{D} | \psi_g \rangle e^{i \int_\tau^t dt' E_{ba,n}} \\ &\approx -i\gamma\theta(t-\tau) \sum_n \left\{ D_{g;b,n}^2 \left(1 - \frac{1}{2} \sum_m \frac{D_{b,n;d,m}^2 [F_{\text{IR}}^2(t) + F_{\text{IR}}^2(\tau)]}{(E_{d,m} - E_{b,n})^2} \right) \right. \\ &\quad - iD_{g;b,n}^2 \sum_m \frac{D_{b,n;d,m}^2}{E_{d,m} - E_{b,n}} \int_\tau^t dt' F_{\text{IR}}^2(t') \\ &\quad \left. + D_{g;b,n} \sum_m \sum_{k \neq n} D_{g;b,k} \frac{D_{b,k;d,m} D_{b,n;d,m} [F_{\text{IR}}^2(t) + F_{\text{IR}}^2(\tau)]}{(E_{d,m} - E_{b,n})(E_{b,k} - E_{b,n})} \right\} e^{iE_{b,n}(t-\tau)}. \end{aligned} \quad (\text{B.13})$$

Ignoring the terms with trivial time-dependence as well as setting the step function equal to one and ignoring the window function, we get the

response function

$$\begin{aligned}
S_{a1}(\omega, \tau) = & - \sum_n \sum_m \frac{\sqrt{\pi}\gamma^2 D_{g;b,n}^2 D_{b,n;d,m}^2 F_{0,\text{IR}}^2 T_{\text{IR}}}{4\sqrt{2}(E_{d,m} - E_{b,n})c} \\
& \times \left[\frac{1}{\omega - E_{b,n}} + \frac{1}{2(E_{d,m} - E_{b,n})} \right] \omega \cos \left[(E_{b,n} - \omega)\tau \right] \\
& \left[\exp \left(- \frac{T_{\text{IR}}^2 (\omega - E_{b,n} - 2\omega_{\text{IR}})^2}{32} \right) + \exp \left(- \frac{T_{\text{IR}}^2 (\omega - E_{b,n} + 2\omega_{\text{IR}})^2}{32} \right) \right. \\
& \left. - 2 \exp \left(- \frac{T_{\text{IR}}^2 (\omega - E_{b,n})^2}{32} \right) \right] \\
& + \sum_n \sum_m \sum_{k \neq n} \frac{\sqrt{\pi}\gamma^2 D_{g;b,n} D_{g;b,k} D_{b,n;d,m} D_{b,k;d,m} F_{0,\text{IR}}^2 T_{\text{IR}}}{2\sqrt{2}(E_{d,m} - E_{b,n})(E_{b,k} - E_{b,n})c} \\
& \times \omega \cos \left[(E_{b,n} - \omega)\tau \right] \\
& \left[\exp \left(- \frac{T_{\text{IR}}^2 (\omega - E_{b,n} - 2\omega_{\text{IR}})^2}{32} \right) + \exp \left(- \frac{T_{\text{IR}}^2 (\omega - E_{b,n} + 2\omega_{\text{IR}})^2}{32} \right) \right. \\
& \left. - 2 \exp \left(- \frac{T_{\text{IR}}^2 (\omega - E_{b,n})^2}{32} \right) \right] \tag{B.14}
\end{aligned}$$

The second term of the dipole is

$$\langle D \rangle_{a2} = \sum_m \left[a_{d,m}^{(1)} \right]^* \langle \psi_{da,m} | \hat{D} | \psi_g \rangle e^{i \int_{\tau}^t dt' E_{da,m}} \tag{B.15}$$

$$\begin{aligned}
& \approx -i\gamma\theta(t - \tau) \sum_m \sum_n \sum_k D_{g;b,n} D_{g;b,k} \\
& \times \frac{D_{b,n;d,m} D_{b,k;d,m} F_{\text{IR}}(\tau) F_{\text{IR}}(t)}{(E_{d,m} - E_{b,n})(E_{d,m} - E_{b,k})} e^{iE_{d,m}(t-\tau)}. \tag{B.16}
\end{aligned}$$

This yields the response function

$$\begin{aligned}
S_{a2}(\omega, \tau) = & \sum_n \sum_m \frac{\sqrt{\pi} \gamma \rho D_{g;b,n}^2 D_{b,n;d,m}^2 F_{0,\text{IR}}^2 T_{\text{IR}}}{2c(E_{d,m} - E_{b,n})^2} \exp\left(-\frac{4\tau^2}{T_{\text{IR}}^2}\right) \\
& \times \omega \sin(\omega_{\text{IR}} \tau) \sin[(E_{d,m} - \omega)\tau] \\
& \times \left[\exp\left(-\frac{T_{\text{IR}}^2(\omega - E_{d,m} - \omega_{\text{IR}})^2}{16}\right) - \exp\left(-\frac{T_{\text{IR}}^2(\omega - E_{d,m} - \omega_{\text{IR}})^2}{16}\right) \right] \\
+ & \sum_n \sum_m \sum_{k \neq n} \frac{\sqrt{\pi} \gamma \rho D_{g;b,n} D_{g;b,k} D_{b,n;d,m} D_{b,k;d,m} F_{0,\text{IR}}^2 T_{\text{IR}}}{2c(E_{d,m} - E_{b,n})(E_{d,m} - E_{b,k})} \exp\left(-\frac{4\tau^2}{T_{\text{IR}}^2}\right) \\
& \times \omega \sin(\omega_{\text{IR}} \tau) \sin[(E_{d,m} - \omega)\tau] \\
& \times \left[\exp\left(-\frac{T_{\text{IR}}^2(\omega - E_{d,m} - \omega_{\text{IR}})^2}{16}\right) - \exp\left(-\frac{T_{\text{IR}}^2(\omega - E_{d,m} - \omega_{\text{IR}})^2}{16}\right) \right]
\end{aligned} \tag{B.17}$$

Bibliography

- [1] J. J. Rørstad, N. S. W. Ravn, L. Yue, and L. B. Madsen, Attosecond transient-absorption spectroscopy of polar molecules, *Phys. Rev. A* **98**, 053401 (2018).
- [2] F. Krausz and M. Ivanov, Attosecond physics, *Rev. Mod. Phys.* **81**, 163 (2009).
- [3] M. Wu, S. Chen, S. Camp, K. J. Schafer, and M. B. Gaarde, Theory of strong-field attosecond transient absorption, *Journal of Physics B: Atomic, Molecular and Optical Physics* **49**, 062003 (2016).
- [4] M. B. Gaarde, C. Buth, J. L. Tate, and K. J. Schafer, Transient absorption and reshaping of ultrafast XUV light by laser-dressed helium, *Phys. Rev. A* **83**, 013419 (2011).
- [5] C.-T. Liao, A. Sandhu, S. Camp, K. J. Schafer, and M. B. Gaarde, Beyond the single-atom response in absorption line shapes: Probing a dense, laser-dressed helium gas with attosecond pulse trains, *Phys. Rev. Lett.* **114**, 143002 (2015).
- [6] C.-T. Liao, A. Sandhu, S. Camp, K. J. Schafer, and M. B. Gaarde, Attosecond transient absorption in dense gases: Exploring the interplay between resonant pulse propagation and laser-induced line-shape control, *Phys. Rev. A* **93**, 033405 (2016).
- [7] E. Goulielmakis, Z.-H. Loh, A. Wirth, R. Santra, N. Rohringer, V. S. Yakovlev, S. Zherebtsov, T. Pfeifer, A. M. Azzeer, M. F. Kling, et al., Real-time observation of valence electron motion, *Nature* **466**, 739 (2010).
- [8] H. Wang, M. Chini, S. Chen, C.-H. Zhang, F. He, Y. Cheng, Y. Wu, U. Thumm, and Z. Chang, Attosecond time-resolved autoionization of argon, *Physical review letters* **105**, 143002 (2010).
- [9] C. Ott, A. Kaldun, L. Argenti, P. Raith, K. Meyer, M. Laux, Y. Zhang, A. Blättermann, S. Hagstotz, T. Ding, et al., Reconstruction and control of a time-dependent two-electron wave packet, *Nature* **516**, 374 (2014).
- [10] J. C. Baggesen, E. Lindroth, and L. B. Madsen, Theory of attosecond absorption spectroscopy in krypton, *Phys. Rev. A* **85**, 013415 (2012).
- [11] J. J. Rørstad, J. E. Bækhoj, and L. B. Madsen, Analytic modeling of structures in attosecond transient-absorption spectra, *Phys. Rev. A* **96**, 013430 (2017).
- [12] M. Schultze, K. Ramasesha, C. D. Pemmaraju, S. A. Sato, D. Whitmore, A. Gandman, J. S. Prell, L. J. Borja, D. Prendergast, K. Yabana, et al., Attosecond band-gap dynamics in silicon, *Science* **346**, 1348 (2014), ISSN 0036-8075.
- [13] L. J. Borja, M. Zürich, C. D. Pemmaraju, M. Schultze, K. Ramasesha, A. Gandman, J. S. Prell, P. D., N. D. M., and L. S. R., Extreme ultraviolet transient absorption of solids from femtosecond to attosecond timescales, *J. Opt. Soc. Am. B* **33**, C57 (2016).

- [14] A. Moulet, J. B. Bertrand, T. Klostermann, A. Guggenmos, N. Karpowicz, and E. Goulielmakis, Soft x-ray excitonics, *Science* **357**, 1134 (2017), ISSN 0036-8075.
- [15] E. R. Warrick, W. Cao, D. M. Neumark, and S. R. Leone, Probing the dynamics of rydberg and valence states of molecular nitrogen with attosecond transient absorption spectroscopy, *The Journal of Physical Chemistry A* **120**, 3165 (2016), PMID: 26862883.
- [16] Y. Cheng, M. Chini, X. Wang, A. González-Castrillo, A. Palacios, L. Argenti, F. Martín, and Z. Chang, Reconstruction of an excited-state molecular wave packet with attosecond transient absorption spectroscopy, *Phys. Rev. A* **94**, 023403 (2016).
- [17] E. R. Warrick, J. E. Bækthøj, W. Cao, A. P. Fidler, F. Jensen, L. B. Madsen, S. R. Leone, and D. M. Neumark, Attosecond transient absorption spectroscopy of molecular nitrogen: Vibrational coherences in the $b'{}^1\Sigma_u^+$ state, *Chemical Physics Letters* (2017), ISSN 0009-2614.
- [18] C.-T. Liao, X. Li, D. J. Haxton, T. N. Rescigno, R. R. Lucchese, C. W. McCurdy, and A. Sandhu, Probing autoionizing states of molecular oxygen with XUV transient absorption: Electronic-symmetry-dependent line shapes and laser-induced modifications, *Phys. Rev. A* **95**, 043427 (2017).
- [19] J. E. Bækthøj, L. Yue, and L. B. Madsen, Nuclear-motion effects in attosecond transient-absorption spectroscopy of molecules, *Phys. Rev. A* **91**, 043408 (2015).
- [20] J. E. Bækthøj and L. B. Madsen, Light-induced structures in attosecond transient-absorption spectroscopy of molecules, *Phys. Rev. A* **92**, 023407 (2015).
- [21] J. E. Bækthøj and L. B. Madsen, Attosecond transient-absorption spectroscopy on aligned molecules, *Phys. Rev. A* **94**, 043414 (2016).
- [22] T. Helgaker, P. Jørgensen, and J. Olsen, *Molecular Electronic-Structure Theory* (Wiley, 2004).
- [23] H. Hettema, H. J. A. Jensen, P. Jørgensen, and J. Olsen, Quadratic response functions for a multiconfigurational self-consistent field wave function, *The Journal of Chemical Physics* **97**, 1174 (1992), <https://doi.org/10.1063/1.463245>.
- [24] K. L. Bak, P. Jørgensen, H. J. A. Jensen, J. Olsen, and T. Helgaker, First-order nonadiabatic coupling matrix elements from multiconfigurational self-consistent-field response theory, *The Journal of Chemical Physics* **97**, 7573 (1992), <https://doi.org/10.1063/1.463477>.
- [25] J. E. Bækthøj, C. Lévesque, and L. B. Madsen, Signatures of a Conical Intersection in Attosecond Transient Absorption Spectroscopy, *Phys. Rev. Lett.* **121**, 023203 (2018).
- [26] M. Feit, J. Fleck, and A. Steiger, Solution of the Schrödinger equation by a spectral method, *Journal of Computational Physics* **47**, 412 (1982), ISSN 0021-9991.
- [27] F. T. Smith, Diabatic and adiabatic representations for atomic collision problems, *Phys. Rev.* **179**, 111 (1969).
- [28] J. C. Baggesen and L. B. Madsen, On the dipole, velocity and acceleration forms in high-order harmonic generation from a single atom or molecule, *Journal of Physics B: Atomic, Molecular and Optical Physics* **44**, 115601 (2011).
- [29] B. H. Bransden and C. J. Joachain, *Physics of Atoms and Molecules* (Pearson, 2003), 2nd ed.
- [30] M. Born and K. Huang, *Dynamical Theory of Crystal Lattices*, International series of monographs on physics (Clarendon Press, 1954).

- [31] J. J. Sakurai and J. Napolitano, *Modern Quantum Mechanics* (Pearson, 2011), International ed.
- [32] F. Jensen, *Introduction to Computational Chemistry* (Wiley, 2017), 3rd ed.
- [33] P. Norman, K. Ruud, and T. Saue, *Principles and Practices of Molecular Properties: Theory, Modeling and Simulations* (John Wiley & Sons, Ltd, 2018), ISBN 9780470725627.
- [34] T. B. Pedersen, *Introduction to Response Theory* (Springer International Publishing, Cham, 2017), pp. 269–294, ISBN 978-3-319-27282-5.
- [35] K. Aidas, C. Angeli, K. L. Bak, V. Bakken, R. Bast, L. Boman, O. Christiansen, R. Cimraglia, S. Coriani, P. Dahle, et al., The Dalton quantum chemistry program system, *WIREs Comput. Mol. Sci.* **4**, 269 (2014).
- [36] J. Olsen and P. Jørgensen, Linear and nonlinear response functions for an exact state and for an MCSCF state, *The Journal of Chemical Physics* **82**, 3235 (1985), <https://doi.org/10.1063/1.448223>.
- [37] R. Bast, D. H. Friese, B. Gao, D. J. Jonsson, M. Ringholm, S. S. Reine, and K. Ruud, OpenRSP: open-ended response theory (version 1.0.0), .
- [38] N. C. Handy and A. M. Lee, The adiabatic approximation, *Chemical Physics Letters* **252**, 425 (1996), ISSN 0009-2614.
- [39] J. von Neumann and E. Wigner, Über das verhalten von eigenwerten bei adiabatischen prozessen, *Physik Z.* **30**, 467 (1929).
- [40] L. Landau and E. Lifshitz, *Quantum Mechanics: Non-Relativistic Theory*, Course of Theoretical Physics (Elsevier Science, 1981), ISBN 9780080503486.
- [41] C. A. Mead, The "noncrossing" rule for electronic potential energy surfaces: The role of time-reversal invariance, *The Journal of Chemical Physics* **70**, 2276 (1979), <https://doi.org/10.1063/1.437733>.
- [42] P. Saalfrank, Photodesorption of neutrals from metal surfaces: a wave packet study, *Chemical Physics* **193**, 119 (1995), ISSN 0301-0104.
- [43] H. Werner and W. Meyer, MCSCF study of the avoided curve crossing of the two lowest $^1\Sigma^+$ states of LiF, *The Journal of Chemical Physics* **74**, 5802 (1981).
- [44] B. Bransden and M. McDowell, *Charge Exchange and the Theory of Ion-atom Collisions*, International series of monographs on physics (Clarendon Press, 1992), ISBN 9780198520207.
- [45] S. Chen, M. Wu, M. B. Gaarde, and K. J. Schafer, Quantum interference in attosecond transient absorption of laser-dressed helium atoms, *Phys. Rev. A* **87**, 033408 (2013).
- [46] Maxima, Maxima, a computer algebra system. version 5.34.1, (2014).
- [47] C. C. Marston and G. G. Balint-Kurti, The Fourier grid Hamiltonian method for bound state eigenvalues and eigenfunctions, *The Journal of Chemical Physics* **91**, 3571 (1989), <https://doi.org/10.1063/1.456888>.
- [48] M. Frigo and S. G. Johnson, The Design and Implementation of FFTW3, *Proceedings of the IEEE* **93**, 216 (2005), special issue on "Program Generation, Optimization, and Platform Adaptation".
- [49] B. Zhang, J. Zhao, and Z.-X. Zhao, Multi-Electron Effects in Attosecond Transient Absorption of CO Molecules, *Chinese Physics Letters* **35**, 043201 (2018).
- [50] L. Holmegaard, J. H. Nielsen, I. Nevo, H. Stapelfeldt, F. Filsinger, J. Küpper, and G. Meijer, Laser-induced alignment and orientation of quantum-state-selected large molecules, *Phys. Rev. Lett.* **102**, 023001 (2009).

- [51] S. De, I. Znakovskaya, D. Ray, F. Anis, N. G. Johnson, I. A. Bocharova, M. Magrakvelidze, B. D. Esry, C. L. Cocke, I. V. Litvinyuk, et al., Field-free orientation of CO molecules by femtosecond two-color laser fields, *Phys. Rev. Lett.* **103**, 153002 (2009).
- [52] K. Oda, M. Hita, S. Minemoto, and H. Sakai, All-optical molecular orientation, *Phys. Rev. Lett.* **104**, 213901 (2010).
- [53] E. Frumker, C. T. Hebeisen, N. Kajumba, J. B. Bertrand, H. J. Wörner, M. Spanner, D. M. Villeneuve, A. Naumov, and P. B. Corkum, Oriented rotational wave-packet dynamics studies via high harmonic generation, *Phys. Rev. Lett.* **109**, 113901 (2012).
- [54] H. Stapelfeldt and T. Seideman, Colloquium: Aligning molecules with strong laser pulses, *Rev. Mod. Phys.* **75**, 543 (2003).
- [55] M. Kowalewski, K. Bennett, J. R. Rouxel, and S. Mukamel, Monitoring nonadiabatic electron-nuclear dynamics in molecules by attosecond streaking of photoelectrons, *Phys. Rev. Lett.* **117**, 043201 (2016).
- [56] M. Kowalewski, K. Bennett, K. E. Dorfman, and S. Mukamel, Catching conical intersections in the act: Monitoring transient electronic coherences by attosecond stimulated x-ray raman signals, *Phys. Rev. Lett.* **115**, 193003 (2015).
- [57] E. R. Warrick, A. P. Fidler, W. Cao, E. Bloch, D. M. Neumark, and S. R. Leone, Multiple pulse coherent dynamics and wave packet control of the N₂ $a''\ ^1\Sigma_g^+$ dark state by attosecond four-wave mixing, *Faraday Discuss.* **212**, 157 (2018).
- [58] L. Drescher, M. J. J. Vrakking, and J. Mikosch, Attosecond transient absorption spectroscopy without inversion symmetry, *Journal of Physics B: Atomic, Molecular and Optical Physics* **53**, 164005 (2020).